Université de Montréal

Les étoiles Wolf-Rayets en cavales extrêmes

par
Melissa Sara Muñoz

Département de physique
Faculté des arts et des sciences

Mémoire présenté à la Faculté des études supérieures
en vue de l'obtention du grade de Maître ès sciences (M.Sc.)
en astrophysique

Avril, 2016

Université de Montréal
Faculté des études supérieures

Ce mémoire intitulé:

Les étoiles Wolf-Rayets en cavales extrêmes

présenté par:

Melissa Sara Muñoz

a été évalué par un jury composé des personnes suivantes:

Patrick Dufour,	président-rapporteur
Anthony Moffat,	directeur de recherche
David Lafrenière,	membre du jury

Mémoire accepté le: ....

RÉSUMÉ

Parmi les étoiles Wolf-Rayets (WR) les plus éloignées du plan galactique (GP), seules deux étoiles WR possèdent une mention de binarité: WR 148, localisée à 800 pc au-dessus du GP, et WR 71, à 700 pc au-dessous du GP. WR 148 possède une période orbitale bien établie de 4.3173 jours dont le compagnon est soupçonné d'être soit une étoile B ou bien un trou noir. Quant à WR 71, quoique son statut de binarité ne soit pas confirmé, le compagnon (s'il existe) est également soupçonné d'être un objet compact (cc) ayant une période orbitale de 7.7 jour. Dans les deux cas, aucune signature du compagnon n'a été détectée. Ainsi, puisqu'elles se retrouvent si fortement éjectées du GP, ces deux étoiles ont donc été considérées comme de bons candidats de systèmes du type WR+cc; une classe d'objets très rarement observés.

Pour identifier la nature du compagnon de WR 148, nous avons obtenu de multiples spectres à l'Observatoire du Mont-Mégantic (OMM) ainsi qu'à l'Observatoire Keck. Pareillement, pour déterminer le statut de binarité de WR 71, nous avons obtenu un mois de photométrie ininterrompue par le micro-satelite MOST (Microvariability and Oscillations of STars) en parallèle avec une série de spectres à partir su sol.

Il s'avère qu'aucune de nos cibles ne fait partie des rares systèmes binaires WR+cc. Le compagnon de WR 148 est ni un objet compact, ni une étoile B, mais plutôt une étoile O et WR 71 est en fait une étoile simple. Ces implications seront par la suite discutées.

Mots clés étoile individuelle: WR 148, étoile individuelle: WR 71.

ABSTRACT

Among the most highly ejected Wolf-Rayet (WR) stars from the Galactic plane (GP), only two are indicated with a possible binary status: WR 148 located at 800 pc above the GP and WR 71 at 700 pc below the GP. WR 148 is a confirmed single lined spectroscopic binary in a 4.3173 day orbital period suspected to harbour either a low mass B star or a black hole (BH) companion. On the other hand, WR 71 is only a suspected single lined spectroscopic binary, also thought to comprise a compact companion (cc) in a short 7.7-day period orbit. In both cases, no obvious signatures of the unseen companions have been detected. Therefore, in an attempt to explain their extreme runaway status, these stars were often interpreted as WR+cc binaries; a rarely observed class of objects.

In order to identify the nature of WR 148's companion, we obtained multiple spectra from l'Observatoire du Mont-Mégantic (OMM) in conjunction with two nights of spectra at opposite quadratures at Keck Observatory. Similarly, to reveal WR 71's binary status, we obtained one month of uninterrupted space-based photometry from the MOST micro satellite (Microvariability and Oscillations of STars) in parallel with several ground based spectroscopy.

We conclude that neither targets belong to the rare WR+cc systems. WR 148's companion is now found to be an O star rather than the expected B star or BH and WR 71 is in fact a normal single star runaway. The implications of this are then discussed.

Keywords: individual stars: WR 148, individual stars: WR 71.

TABLE DES MATIÈRES

LISTE DES TABLEAUX

LISTE DES FIGURES

LISTE DES ANNEXES

LISTE DES SIGLES

BH	Black hole (Trou noir)
BME	Brown, McLean and Emslie
CAK	Castor, Abbott and Klein
CIR	Corotating Interaction Region (Région d'interaction en corotation)
cc	Compact companion (Compagnon compact)
CE	Common envelope (Enveloppe commune)
CW	Colliding winds (Collision de vents)
DAC	Discrete Absorption Component (Composante discrète d'absorption)
EW	Equivalent Width (Largeur équivalente)
FW	Full Width (Pleine largeur)
GP	Galactic plane (plan Galactique)
HMXRB	High-mass X-ray binary (Binaire X massive)
LBV	Luminous Blue Variable (Variable lumineuse bleue)
LSR	Local standard of rest (Référentiel repos local)
MOST	Microvariability and Oscillations of STars (Microvariabilité et Oscillations STellaires)
NS	Neutron star (Étoile à Neutron)
OMM	Observatoire du Mont Mégantic
PDM	Phase Dispersion Minimization
PoWR	The Potsdam Wolf-Rayet Models (Les modèles Potsdam de Wolf-Rayet) [1]
RV	Radial velocity (Vitesse radiale)
SB1	Single-lined spectroscopic binary (Binaire spectroscopique à un spectre)
SB2	Double-lined spectroscopic binary (Binaire spectroscopique à deux spectres)
SN	Supernova
UV	Ultraviolet
WC	Étoile Wolf-Rayet riche en carbone
WN	Étoile Wolf-Rayet riche en azote
WNE	WN early (Étoile WN précoce)

---

[1] Logiciel conçu pour calculer les spectres d'étoiles WR

WNL	WN late (Étoile WN tardive)
WNh	Étoile WN en abondance d’hydrogène
WNo	Étoile WN en absence d’hydrogène
WR	Étoile Wolf-Rayet
WRXRB	Wolf-Rayet X-ray binary

NOTATION

$\dot{M}$	Taux de perte de masse
v_∞	Vitesse terminale d'un vent stellaire
β	Exposant sur la loi β d'un vent stellaire
α	Nombre d'électrons libres par baryon
M_1	Masse de l'étoile primaire
M_2	Masse de l'étoile secondaire
q	Rapport de masse du secondaire sur le primaire
K_1	Amplitude en RV de l'étoile primaire
K_2	Amplitude en RV de l'étoile secondaire
γ_1	Vitesse systémique de l'étoile primaire
γ_2	Vitesse systémique de l'étoile secondaire
e	Excentricité
P	Période
v_r	Vitesse radiale
R_*	Rayon hydrostatique
i	Inclinaison orbitale
ϕ	Phase orbitale
G	Constante Gravitationelle
c	Vitesse de la lumière

À mes parents.

REMERCIEMENTS

Je remercie infiniment mon directeur de recherhe, Anthony Moffat, pour les opportunités et toutes les discussions que nous avons eues et que nous allons avoir. J'ai été profondément touchée par sa grande générosité et je garderai toujours de très forts souvenirs de nos rencontres.

Je tiens également à remercier tous les membres du groupe d'étoiles massives à l'Université de Montréal incluant Nicole St-Louis, Noel Richardson, Herbert Pablo, Tahina Ramiaramanantsoa et Emily Aldoretta. Les discussions que nous avons eues à notre club hebdomadaire étaient non seulement très instructives, mais d'autant plus très agréables.

Je remercie aussi mes collègues Grant Hill et Tomer Shenar qui m'ont chaudement accueillie dans leur institution de recherche et m'ont énormément aidée à la réalisation de mes articles.

CHAPTER 1

INTRODUCTION

Le chemin évolutif et fin de vie d'une étoile est surtout déterminé par sa masse initiale. À titre indicatif, plus qu'une étoile est massive, plus que sa durée de vie sera réduite. Par ailleurs, non seulement que l'espérance de vie des étoiles massives est très courte en comparaison des étoiles de faible masse, mais elles sont aussi peu nombreuses, car la formation stellaire favorise les étoiles de faible masse. Quoiqu'en nombre minoritaire, les étoiles massives contribuent tout de même à la majorité de la lumière au seins des galaxies et jouent un rôle indispensables à l'enrichissement du milieu interstellaire. En effet, seules les étoiles les plus massives expulsent de la matière via ses grands vents stellaires pendant son évolution stellaire et enfin via une violente éjection de matière à la fin de sa vie autrement connue sous le nom d'explosion supernova. Les étoiles massives sont donc des étoiles rares et précieuses. En lien avec le sujet de mémoire, le chapitre suivant sera entièrement consacré à fournir un aperçu général sur les étoiles massives.

1.1 Les étoiles massives

1.1.1 Évolution stellaire: un bref aperçu

Le gradient de la pression de gaz interne des étoiles s'oppose perpétuellement à la compression gravitationnelle afin de demeurer en équilibre hydrostatique. L'énergie perdue par la radiation entraine la contraction inévitable des étoiles jusqu'à la formation d'un objet compact. Telle est la fatalité de tout objet stellaire (Tauris & van den Heuvel, 2006a).

Les étoiles consacrent la majorité de leur vie sur la séquence principale (Meynet & Maeder, 2003). Sur la séquence principale, elles sont soutenues par la fusion nucléaire d'hydrogène à l'hélium. Les étoiles de masse intermédiaire, au-deçà de $8M_{\odot}$, n'ont typiquement pas de noyaux assez chauds pour déclencher la fusion d'hélium suite à l'épuisement de l'hydrogène. Ainsi, sujette à la compression gravitationnelle, leurs noyaux deviennent dégénérés et elles termineront leur vie en une naine blanche. Cependant, certaines étoiles de masse intermédiaire sont capables de brûler de l'hélium, menant aux naines blanches de type CO. D'autre part, les étoiles massives, au-delà de $8\,M_\odot$, poursuivent leur évolution par une série de combustion cyclique d'éléments plus lourds jusqu'à la formation de fer déclenchant une explosion supernova (SN) à effondrement de coeur et éjectant ses couches externes. Les étoiles dont la masse initiale est comprise entre 8 et $25\,M_\odot$ achèveront leur vie en étoiles à neutrons, tandis que celles supérieures à $25\,M_\odot$, en trous noirs (Postnov & Yungelson, 2014a).

Les étoiles se distinguent en fonction de leur température et luminosité à l'aide de deux systèmes de classification distinctes: le type spectral et la classe de luminosité. La détermination du type spectral d'une étoile s'effectue à l'aide du guide de classification Morgan-Keenan (Hoffleit, 1943). En ordre de température décroissant, les types spectraux sont identifiés par les lettres O, B, A, F, G, K, and M. Les étoiles O font partie des étoiles massives ayant des températures effectives allant jusqu'à 45 000 K. À l'autre extrême, les étoiles K sont de faible masses avec des températures effectives aux alentours de 2500 K. Quant à leurs espérances de vie, les étoiles massives ont des durées de vie typiquement de l'ordre de quelques millions d'années, alors que les étoiles de faible masse peuvent atteindre des durées de vie bien au-delà de plusieurs milliards d'années. Numérotés par des chiffres entre 0 et 9, les types spectraux se subdivisent davantage à l'intérieure même de chaque type où l'indice 0 correspond aux etoiles les plus chaudes et 9 aux plus froides. La classe de lumonisité est une spécification supplémentaire du type spectral. Ainsi, les étoiles sont d'abord identifiées par un type spectral suivi par une classe de luminosité. En ordre décroissant de luminosité, les classes de luminosité sont indiqués avec des chiffres romains allant de I, pour les Supergéantes, à V, pour les naines.

Seules les étoiles les plus massives, supérieures à approximativement $25\,M_\odot$, passent par une phase Wolf-Rayet (WR) avant de terminer leur vie en explosion SN. Les étoiles WRs sont des étoiles massives très évoluées descendantes des étoiles O ayant des vents stellaires très puissants. La phase WR dure approximativememnt 10% du temps de vie de l'étoile progénitrice, l'étoile O (Crowther, 2007). Elles possèdent des vitesses terminales de l'ordre de 2000 à 3000 $\mathrm{km\,s^{-1}}$ ainsi que des taux de pertes de masses de l'ordre de $10^{-5}\,M_{\odot}\,\mathrm{yr}^{-1}$ (Lamers & Cassinelli, 1999). Caractérisées par leurs larges raies d'émission, elles sont pourvues d'atmosphères étendues continuellement en expansion. Ceci génère des profils P Cygni typiques des étoiles WRs dont leurs composantes d'absorption sont décalées vers le bleu et leurs composantes d'émission sont décalées vers le rouge en vertu de l'effet Doppler (Sobolev, 1960). Par contre, certaines raies, surtout celles de recombinaison, démontrent uniquement de l'émission.

Les étoiles WRs, toutes riches en hélium, sont classifiées en deux sous-types: les étoiles WN riches en azote et les étoiles WC riches en carbone. Cette première catégorie est sous-divisée en WN précoce (« WN early », WNE) ou WN tardive (« WN late », WNL) selon le rapport des intensités des raies, telles que WNE = WN2, 3, 4, 5 et WNL = WN6, 7, 8, 9 avec certaines WN6 étant WNE. La majorité des WNL montrent de l'hydrogène alors que la majorité des WNE en n'ont pas. Qualitativement, l'abondance d'hydrogène peut être mesurée en fonction du rapport H I sur He II. Ce dernier est souvent estimé par le rapport de Hβ + He II λ4861 sur He II λ4542. Si ce rapport est nul, inférieur à 0.5 ou supérieur 0.5, les WRs sont notées des WNo, WN(h) ou WNh respectivement (Smith et al., 1996).

Entourées par des vents denses et optiquement épais, il n'est plus question de déterminer une température effective aux étoiles WRs, car leurs rayons stellaires sont mal définis. Comme l'enveloppe circumstellaire des étoiles WRs empêchent de voir leurs photosphères, il sagira plutot de caractériser une température stellaire, T_*, définie au rayon hydrostatique, R_*. Le rayon hydrostatique est déterminé à une profondeur optique de Rosseland arbitrairement élévée, typiquement $\sim$ 10 (Crowther, 2007) ou $\sim$ 20 (Hamann et al., 2006a). Dans ce contexte, les étoiles WRs possèdent des valeurs de R_* de l'ordre de quelques rayons solaires et atteigent des valeurs de T_* entre 35 000 K et 85 000 K qui varie en fonction du type spectral.

Toujours au brûlage d'hydrogène, les étoiles WNh, dont la plupart sont des WNLh se comportent plus spectroscopiquement parlant comme des versions plus extrêmes et massives des étoiles Of (étoiles O avec raies d'émission), contrairement aux étoiles WNo, qui sont hors de la séquence principale et dans la phase du brûlage d'hélium. Les étoiles

WNo sont donc considérées comme étant de vraies WR au sens classique alors que les WNh sont dites non classiques.

Selon Crowther (2007), le scénario évolutif des WRs se distingue en trois cas étant donné une masse initiale (dans un environnement de métallicité solaire):

Supérieure à $75 M_{\odot}$

$$O \rightarrow WN(H-rich) \rightarrow LBV \rightarrow WN(H-poor) \rightarrow WC \rightarrow SNIc$$

Comprise entre 40 et $75 M_{\odot}$

$$O \rightarrow LBV \rightarrow WN(H-poor) \rightarrow WC \rightarrow SNIc$$

Comprise entre 25 et $40 M_{\odot}$

$$O \rightarrow LBV/RSG \rightarrow WN(H-poor) \rightarrow SNIb$$

Avant de passer à la phase WR, les étoiles O passent par une phase transitoire: la phase variable lumineuse bleue (« luminous blue variables », LBV), si elles sont assez massives ou sinon la phase supergéante rouge (« red supergiant » , RSG). Ensuite, débutant comme des WRs riches en azote, elles évoluent vers des WRs riches en carbone. Enfin, elles subissent des supernovae du type Ib (si l'étoile a entièrement perdu son enveloppe d'hydrogène par l'entremise de ses vents stellaires) ou du type Ic (si l'étoile a entièrement perdu de son enveloppe d'hydrogène ainsi que son enveloppe d'hélium).

1.1.2 Les vents stellaires

Les vents chauds des étoiles massives sont accélérés par la pression de radiation. C'est le principe de base derrière la théorie des vents entrainés par les raies spectrales développées par Castor, Abbott & Klein (1975), ci-après CAK, pour les étoiles O. Dans ce contexte, les vents stellaires sont surtout caractérisés par deux quantités physiques: le taux de perte de masse, $\dot{M}$ et la vitesse terminale, v_{∞}.

Pour des vents stationnaires à écoulement sphériquement symétrique, le taux de perte de masse peut être exprimé à partir de l'équation de continuité de la masse comme suit:

$$\dot{M} = 4\pi r^2 \rho(r) v(r) \tag{1.1}$$

où r est une distance radiale à partir du centre de l'étoile, $\rho(r)$ est la densité de masse et v(r) est la vitesse du vent. L'équation 1.1 indique qu'il n'y a aucune destruction ni création de masse. Autrement dit, le flux de masse rentrant est équivalent au flux de masse sortant.

Quant à la vitesse du vent, $v(r)$ est souvent approximé par la loi β. Introduite par CAK, il s'agit d'une loi de vitesse empirique de la forme

$$v(r) \simeq v_0 + (v_\infty - v_0)\left(1 - \frac{R_*}{r}\right)^\beta \tag{1.2}$$

où R_* est le rayon hydrostatique, v_0 est la vitesse à ce rayon, v_∞ est la vitesse terminale et β est un paramètre libre. L'équation 1.2 décrit le comportement général d'un vent ayant une certaine vitesse initiale (v_0) à la photosphère, tandis qu'infiniment loin de l'étoile, lorsque $r \to \infty$, le vent atteint une vitesse maximale (v_∞). Entre ces deux cas extrêmes, le paramètre β contrôle la raideur de l'accélération, tel que pour bêta plus grand, l'accélération est plus faible près de l'étoile. Pour le vent d'une source ponctuelle, on peut montrer facilement que $\beta = 0.5$. Autrement, pour le vent d'une source de taille finie, $\beta > 0.5$ (Lamers & Cassinelli, 1999).

Les théories de Friend & Abbott (1986) et Pauldrach et al. (1986) prédisent et vérifient observationellement une valeur de $\beta \sim 0.8$ pour les étoiles O. Ainsi, une valeur be β de l'ordre de l'unité est généralement acceptée pour les étoiles massives. Quoique les observations de Lépine & Moffat (1999a) suggèrent que, pour les étoiles WRs à vent fort, β sera en fait plus élevé (de l'ordre de $\beta \sim 3$ allant même jusqu'à ~ 10) .

La vitesse terminale peut être déterminée observationnellement en mesurant v_{black} des profils P Cygni dont la composante d'absorption est saturée (Prinja et al., 1990). La valeur de v_{black} correspond à la vitesse la plus bleue à zéro absorption et permet de bien estimer v_∞ (i.e. $v_\infty = v_{\text{black}}$). Quant à la détermination du taux de perte de masse, il est plus ambigu. D'une part, il peut être mesuré à l'aide de l'émission $H\alpha$ (Lamers & Leitherer, 1993) et d'autre part, par l'émission continue des transitions libre-libre aux ondes radio (Puls et al., 1996).

1.1.3 Variabilités à petites échelles

Dans un monde idéal, les vents stellaires sont homogènes. Par contre, ceci a été sérieusement mis en question lors des observations spectroscopiques de Moffat et al. (1988) qui ont proposé des évidences indirectes quant à la nature inhomogène du vent, autrement connue sous les noms de « clumps ». Il s'agit d'un phénomène stochastique résultant des instabilités du mécanisme d'entraînement du vent (Gayley & Owocki, 1995). La présence des clumps est surtout perceptible sur de larges raies d'émissions des WRs où les grumeaux se propagent et se dispersent radialement dans le vent sur une durée de l'ordre de quelques heures (Lépine & Moffat, 1999b). Si on suppose que les clumps se dispersent au même rythme que le vent, la surveillance temporelle de l'expansion des clumps permettra d'une manière directe de déterminer la loi de vitesse de l'étoile incluant le paramètre β

Outre les signatures spectroscopiques des clumps, ces fluctuations stochastiques se manifestent aussi dans les observations polarimétriques. Robert et al. (1989) ont noté que les WRs apparemment simples sont intrinsèquement variables sur une échelle de temps comparable à celle des clumps. D'ailleurs, l'amplitude de ces variations est anticorrelée avec la vitesse terminale des vents des étoiles WRs. Ceci indique que les clumps seront en principe présents dans toutes les étoiles WRs, mais ne survivent pas si bien dans les types WR précoces où les vitesses terminales sont trop élevées pour être propices à la formation des clumps (Robert et al., 1989). Une interprétation alternative se trouve dans Michaux et al. (2014), où les étoiles WRs plus chaudes ont une zone de convection sub-surfacique qui est plus proche de la surface de l'étoile et donc moins puissante pour générer des clumps.

Les clumps ont un impact direct sur la détermination du taux de perte de masse des étoiles WRs. Les taux de perte de masse ont traditionnellement été obtenus soit par l'émission Hα, notés $\dot{M}(\mathrm{H}\alpha)$ (Lamers & Leitherer, 1993) ou bien par l'émission radio libre-libre, notés $\dot{M}(\mathrm{radio})$ (Puls et al., 1996). Selon ces auteurs, les deux méthodes ont généralement été en accord. Un moyen alternatif consiste à utiliser les raies de résonances ultraviolettes du doublet PV, notés $\dot{M}(\mathrm{P}^{+4})$ (Fullerton et al., 2006). Cependant, un facteur 10 à 100 discrimine ce diagnostique du taux de perte masses aux autres. Fullerton et al. (2006) a expliqué que cette discordance est une conséquence liée au clumping. Effectivement, les deux premières méthodes sont sensibles à ρ^2, alors que cette dernière méthode est uniquement sensible à ρ. Comme le clumping joue un rôle important sur l'homogénéité du vent et par extension sa densité, les diagnostiques de $\dot{M}(\rho)$ seront en principe plus précis. Ceci indiquerait que les déterminations du taux de perte de masse sensibles à ρ^2 (notés $\dot{M}(\rho^2)$, incluant $\dot{M}(\mathrm{H}\alpha)$ et $\dot{M}(\mathrm{radio})$) ont été systématiquement surestimées par rapport à celles sensibles à ρ (notés $\dot{M}(\rho)$, incluant $\dot{M}(\mathrm{P}^{+4})$) par un facteur de 10 à 100. Or, en comparant ces diagnostiques de $\dot{M}(\rho)$ et $\dot{M}(\rho^2)$ avec les techniques de déterminations de $\dot{M}$ des WRs au sein des systèmes WR+O, il s'avère que les valeurs de $\dot{M}(\mathrm{P}^{+4})$ sont inexactes. En effet, St.-Louis et al. (1988) (voir section 1.2.5) et Lamontagne et al. (1996) (voir section 1.2.6) ont respectivement développé des méthodes polarimétriques et photométriques pour dériver le taux de perte de masse de l'étoile WR qui concordent à un facteur 3 près des valeurs de $\dot{M}(\rho^2)$. Les taux de pertes de masse qui découlent de ces deux techniques polarimétriques et photométriques sont aussi uniquement sensibles à ρ et sont donc considérés comme étant plus fiables, car ils sont moins sensibles au clumping. Ainsi, les mesures de $\dot{M}(\mathrm{H}\alpha)$ et $\dot{M}(\mathrm{radio})$ surestiment le taux de perte de masse par un facteur 3 en raison du clumping, tandis que les mesures de $\dot{M}(\mathrm{P}^{+4})$ demeurent imprécises pour des raisons toujours incertaines (Puls et al., 2008).

1.1.4 Variabilités à grandes échelles

Les régions d'interaction en corotation (« corotating interaction regions » , CIRs) surgissent par l'interaction des vents rapides et lents. Ce gradient de vitesse est soupçonné de provenir par des perturbations à la base du vent qui génère des inhomogénéités dans la densité du vent. Couplés avec la rotation rapide de l'étoile, les CIRs donnent lieu à des structures de surdensités à cause des chocs sous forme de bras spiraux. Ces derniers ont été vastement étudiés dans le cadre de vents solaires. Les gradients de vitesses nécessaires pour engendrer des CIRs proviennent de la propulsion des vents non sphériquement symétriques. Ainsi, étant donné la nature inhomogène des étoiles massives, les CIRs devraient aussi être observables dans les vents stellaires. De ce fait, Mullan (1984) a fait les premières démarches pour étendre cette théorie dans le cadre des vents stellaires chauds. Cranmer & Owocki (1996a) ont par la suite fourni des modèles hydrodynamiques adaptés aux étoiles O capables de reproduire des CIRs par l'entremise des taches brillantes à la surface des étoiles.

De telles structures à grandes échelles ont été observées dans les étoiles O sous forme de « discrete absorption components » (DACs). Les DACs se perçoivent comme des absorptions étroites sur les côtés bleus des profils P-Cygni ultraviolets, surtout pour les transitions de résonance (à partir de l'état fondamental). Sur des échelles de temps corrélées avec leur période de rotation, les DACs se déplacent vers le bleu des composantes d'absorption des profils P-Cygni. Les modèles de Cranmer & Owocki (1996a) ont confirmé que les DACs sont effectivement présents en conséquence des CIRs.

Il est soupçonné que la majorité des étoiles O démontrent de telles variabilités (Howarth & Prinja, 1989). Or, la présence des CIRs n'a été confirmée (ou fortement soupçonné) que dans quatre étoiles WRs: WR 6, WN4o, P = 3.76 jours (Morel et al., 1997); WR 134, WN6, P = 2.3 jours (Morel et al., 1999); WR 1, WN4, P = 16.9 jours (Chené & St-Louis, 2010) et WR 110, WN5 P=4.08 jours (Chené et al., 2011). Puisque les profils P-Cygni sont souvent saturés dans les étoiles WRs, l'identification des CIRs par les DACs n'est souvent pas possible. Il faut donc recourir à d'autres moyens de dépistage.

Les étoiles mentionnées ci-dessus (apparemment simples) possèdent des variabilités photométriques, spectroscopiques et polarimétriques quasi-périodiques. Par exemple, au niveau spectroscopique, des variations périodiques en dissymétrie, aplatissement, largeur à mi-hauteur et largeur équivalentes sont notamment observées. Par conséquent, ces étoiles ont souvent été faussement classifiées comme des systèmes binaires ayant un compagnon de faible masse (telle qu'une étoile B ou un objet compact) pour produire des faibles variations en vitesse radiale (Antokhin et al., 1982; Smith et al., 1985).

Cependant, dépourvue de variations en vitesse radiale cohérentes, cette hypothèse est à exclure. Pour confirmer l'origine des CIRs, les étoiles candidates doivent être suivies intensivement par des observations photométriques en parallèle avec des observations spectroscopiques et si possible aussi en polarimétrie linéaire.

1.2 Les étoiles massives en systèmes binaires

1.2.1 Évolution binaire: un bref aperçu

Dans un système binaire serré, les lobes de Roche déterminent la portée gravitationnelle de chaque composante du système. Hors de son lobe, la matière n'est plus gravitationnellement liée à l'étoile respective. Ces deux lobes sont joints par le point Lagrangien L_1, un point équipotentiel critique entre les deux étoiles. Si aucune des étoiles ne remplit son lobe de Roche, elles demeurent stables et le système est dit détaché. L'évolution d'un tel système binaire peut donc être approximée par l'évolution de deux étoiles simples distinctes. Si une des étoiles déborde de son lobe de Roche, un transfert de masse aura lieu via le point L_1 et le système est dit semi-détaché. Il s'agit du débordement du lobe de Roche (« Robe loche overflow » , RLOF). Si les deux étoiles débordent de leur lobe de Roche, le système est dit binaire à contact. En négligeant les étapes intermédiaires de LBV et les détails des sous-types WR, l'évolution binaire à partir d'étoiles massives se schématise comme suit:

$$O+O \rightarrow WR+O \rightarrow cc+O \rightarrow cc+WR \rightarrow cc+cc, \tag{1.3}$$

où cc désigne les compagnons compacts (« compact companion »). Puisque la phase WR est courte comparativement à sa durée de vie comme étant une étoile O, les systèmes WR+WR sont très rarement observés et ont donc été omis dans le scénario évolutif.

Par convention, l'étoile primaire est l'étoile initialement plus massive et l'étoile secondaire est l'étoile initialement moins massive. Comme les étoiles les plus massives évoluent plus rapidement, l'étoile primaire atteint la phase WR d'abord et subit la première explosion SN. Environ 80% à 90% des systèmes risquent de se séparer à ce point

(Eldridge et al., 2011). Les systèmes qui demeurent liés, les O+cc, sont classés comme étant des binaires X massives (« high mass X-ray binaires » , HMXRBs) et sont de forts émetteurs en rayons-X. En principe, ces systèmes évoluent en des WR+cc (« Wolf-Rayet X-ray binaires » , WRXRBs). Cependant ces systèmes sont très rares et sont donc considérés comme des chaînons manquants. Enfin, l'étoile secondaire éprouve la deuxième supernova potentiellement menant à la formation de systèmes doublement compacts, encore plus rares.

Évidemment, le schéma ci-dessus est idéalisé et ne tient pas en compte toutes les interactions binaires telles que le transfert de masse. Au cours de l'évolution stellaire sur la séquence principale, les étoiles massives prennent de l'expansion. Ainsi, l'étoile primaire risque de remplir son lobe de Roche d'abord provocant un transfert de masse vers l'étoile secondaire. Si le transfert de masse a lieu sur une échelle de temps nucléaire (une échelle de temps nécessaire pour qu'une étoile s'épuise son carburant nucléaire; de l'ordre des Gyr) le transfert de masse demeure stable. Dans ce cas, une fois embarqué dans le RLOF, ce processus ne cesse jusqu'à ce que la majeure partie de l'enveloppe riche en hydrogène de l'étoile primaire (allant jusqu'à 70% de la masse totale) soit transférée vers l'étoile secondaire pour que la primaire rentre dans son lobe de Roche (Tauris & van den Heuvel, 2006a). En revanche, si le transfert de masse a lieu sur des échelles de temps dynamiques (une échelle de temps nécessaire pour atteindre l'équilibre hydrostatique; de l'ordre des heures), le transfert de masse est instable et entrainera la formation d'une enveloppe commune autour des deux étoiles. Dans cette configuration, il n'y a que deux possibilités: une éjection de l'enveloppe commune (résultant en un système binaire à séparation considérablement réduite) et, si la séparation des étoiles est suffisamment courte, la fusion des deux étoiles.

1.2.2 La géométrie d'un système binaire

La géométrie d'un système binaire est déterminée par les trois lois de Kepler:

- Le mouvement orbital est elliptique:

$$r = \frac{a(1-e^2)}{1+e\cos\theta}; \tag{1.4}$$

- Le moment cinétique est conservé:

$$r\dot{\theta} = \frac{2\pi a}{P}\sqrt{1-e^2} = \text{constante}; \tag{1.5}$$

- L'énergie totale est conservée menant à:

$$\frac{P^2}{a^3} = \frac{4\pi^2}{G(M_1+M_2)} = \text{constante}, \tag{1.6}$$

où G est la constante gravitationelle, e est l'excentricité du système, θ est l'anomalie vraie (qui varie en fonction du temps), P est la période, a est le demi-grand axe de l'orbite et r est la séparation entre les deux étoiles.

De ces lois, il s'ensuit que l'énergie totale et le moment cinétique total du système sont donnés par

$$E_{orb} = -\frac{1}{2}\frac{GM_1M_2}{a} \qquad \text{et} \qquad J_{orb} = M_1M_2\sqrt{\frac{Ga(1-e^2)}{M_1+M_2}}. \tag{1.7}$$

De plus, en se rappelant que la vitesse en coordonnées polaires s'écrit comme $v^2 = \dot{r}^2 + r^2\dot{\theta}^2$, la vitesse orbitale relative entre les deux étoiles devient

$$v_{\text{orb}} = \sqrt{G(M_1+M_2)\left[\frac{2}{r} - \frac{1}{a}\right]}. \tag{1.8}$$

Les deux étoiles ont chacune une séparation r_1 et r_2 et de vitesse v_1 et v_2 par rapport au centre de masse de telle sorte que $r = r_1 + r_2$ et $v_{\text{orb}} = |\mathbf{v}_1 - \mathbf{v}_2|$. Les séparations individuelles peuvent être exprimées en fonction de la séparation totale comme suit,

$$r_1 = \frac{M_2}{M_1+M_2}r \qquad \text{et} \qquad r_2 = \frac{M_1}{M_1+M_2}r, \tag{1.9}$$

et parallèlement pour les vitesses,

$$v_1 = \frac{M_2}{M_1 + M_2} v_{\text{orb}} \qquad \text{et} \qquad v_2 = \frac{M_1}{M_1 + M_2} v_{\text{orb}}. \tag{1.10}$$

Il est pratique commune de définir le rapport de masse (« mass ratio », q) comme étant le rapport de la masse du secondaire sur le primaire dont les relations entre les masses, les vitesses et les séparations orbitales sont très simples:

$$q \equiv \frac{M_2}{M_1} = \frac{v_1}{v_2} = \frac{r_1}{r_2}. \tag{1.11}$$

Du point de vue d'un observateur terrestre, le plan des orbites est incliné par rapport au plan du ciel selon un angle d'inclinaison i de telle sorte que

$$v_{r,1} = v_1 \sin i \qquad \text{et} \qquad v_{r,2} = v_2 \sin i, \tag{1.12}$$

où $v_{r,1}$ et $v_{r,2}$ sont les vitesses radiales (i.e. les vitesses réelles projetées dans la direction de l'observateur) du primaire et du secondaire respectivement. Au sein d'un système binaire, il est possible de montrer que la vitesse radiale d'une étoile est déterminée par

$$v_{r,i} = \gamma + K_i(e \cos\omega - \cos(\theta + \omega)), \tag{1.13}$$

où ω est la longitude du périastre dans le plan orbital par rapport à la ligne des noeuds, γ est la vitesse du centre de masse le long de la ligne de visée et K est l'amplitude de la courbe vitesse radiale donnée par

$$K_i = \frac{2\pi}{P} \frac{a_i \sin i}{\sqrt{1 - e^2}}, \tag{1.14}$$

pour $i = 1, 2$. Il est toutefois plus commode d'exprimer v_r en fonction de la phase photométrique et non en fonction de l'anomalie vraie. Selon l'approche de Smart & Green (1977), on peut exprimer θ en fonction de l'anomalie excentrique, E, puis E en fonction du temps, t , ou de la phase orbitale, ϕ, comme suit:

$$E - e\sin E = 2\pi\left(\frac{t - T_o}{P}\right) = 2\pi\phi, \tag{1.15}$$

et

$$\tan\frac{\theta}{2} = \sqrt{\frac{1+e}{1-e}}\tan\frac{E}{2} \tag{1.16}$$

où T_o est le temps de passage au périastre. Cependant, la résolution d'un tel système d'équations n'est pas analytique. À la limite où les orbites sont faiblement elliptiques ($e \ll 1$), Budding (1993) a obtenu une forme analytique reliant θ et ϕ de la manière suivante:

$$\theta = 2\pi\phi - \omega \pm \frac{\pi}{2}, \tag{1.17}$$

où le ± correspond au primaire et secondaire respectivement. Ainsi, il en découle de l'équation 1.13 que,

$$\begin{aligned} v_{r,1} &= \gamma + K_1(e\cos\omega_1 - \sin 2\pi\phi), \qquad (1.18)\\ v_{r,2} &= \gamma + K_2(e\cos\omega_2 + \sin 2\pi\phi), \end{aligned}$$

où

$$K_1 = \frac{2\pi}{P}\frac{a_1\sin i}{\sqrt{1-e^2}} \qquad \text{et} \qquad K_2 = \frac{2\pi}{P}\frac{a_2\sin i}{\sqrt{1-e^2}}. \tag{1.19}$$

Dans le cas particulier d'une orbite circulaire ($e = 0$), les équations 1.18 se réduisent à de simples courbes sinusoïdales en anti-phase. Des exemples de courbes de vitesses radiales pour le secondaire et le primaire d'une orbite circulaire et elliptique sont illustrés à la figure 1.1.

1.2.3 Les collisions des vents

Lorsque deux étoiles massives, ayant toutes les deux des vents stellaires puissants, sont au sein d'un système binaire proche, leurs vents interagissent et entrent en collision formant un cône de choc. La géométrie de la zone de choc est délimitée par les régions où la quantité de mouvement entre les deux vents en collisions est nulle. Cela peut être

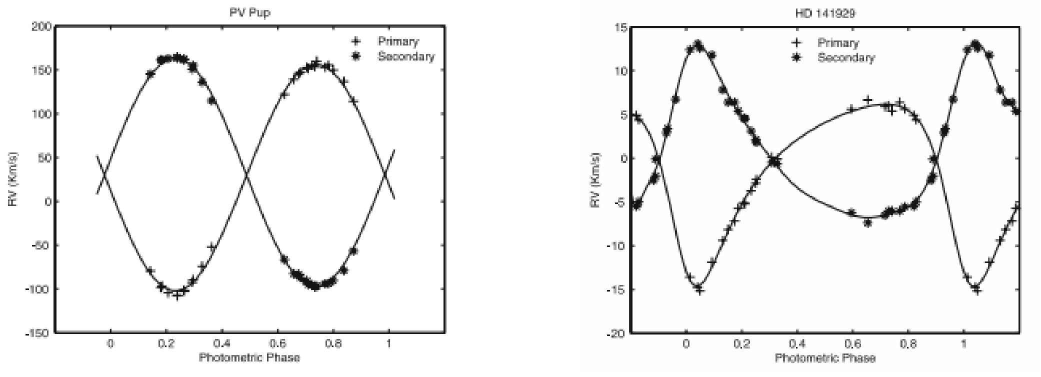

(a) (b)

Figure 1.1: Comparaison des courbes de vitesses radiales pour (a) une orbite circulaire et (b) une orbite elliptique (tiré de Karami & Mohebi (2008)).

déterminé qualitativement par le paramètre η (« wind momentum factor ») qui décrit en quelque sorte la force d'un vent par rapport à l'autre :

$$\eta = \frac{\dot{M}_2 v_2^\infty}{\dot{M}_1 v_1^\infty}, \tag{1.20}$$

où l'indice 1 correspond à l'étoile primaire et l'indice 2 à l'étoile secondaire. Plus rigoureusement, η correspond au rapport du taux de transfert de quantité de mouvement entre les deux vents en collisions. Selon cette convention, il y a donc trois cas possibles à considérer:

$\eta < 1 \Rightarrow$ Le vent du primaire est plus puissant et
la zone de choc forme un cône autour de l'étoile secondaire

$\eta > 1 \Rightarrow$ Le vent du secondaire est plus puissant et
la zone de choc forme un cône autour de l'étoile primaire

$\eta = 1 \Rightarrow$ Les deux vents sont de calibre équivalent et
la zone de choc forme un plan entre les deux étoiles

Bien que les vitesses terminales des étoiles WRs soient du même ordre de grandeur que celles des étoiles O, les taux de perte de masse des étoiles WRs sont nettement supérieurs, typiquement d'un facteur de 10. Ainsi, dans des systèmes WR+O, le cône de choc est forcément autour de l'étoile O. La figure 1.2 décrit de façon schématique la zone de collision des vents dans un tel cas.

La collision des vents induit un échauffement du gaz qui se thermalise et génère des rayons X dits thermiques. Ce gaz chauffé contribue à une source d'émission supplémentaire. Vu selon d'autres lignes de visée pendant que l'étoile O orbite autour de l'étoile WR, cet excès d'émission varie périodiquement. La modélisation de ce phénomène est plus profondément traitée à la section 3.6 du chapitre 2.

1.2.4 Variabilités spectroscopiques

Selon l'effet Doppler, le spectre d'une étoile en mouvement sera décalé vers le bleu si elle s'approche vers un observateur, mais décalé vers le rouge si elle s'éloigne. Ainsi, les binaires spectroscopiques sont des systèmes binaires dont le mouvement orbital des étoiles est exposé par des décalages périodiques des raies spectrales. Ce type de binaire se subdivise en deux catégories: les binaires spectroscopiques à un spectre (« single-lined spectroscopic binary » , SB1) où le spectre d'uniquement une étoile est observée et les binaires spectroscopiques à deux spectres (« double-lined spectroscopic binary » , SB2) où les deux spectres sont observés. Il est à noter que souvent les systèmes binaires spectroscopiques sont classifiés des SB1 à cause de spectres ayant un rapport de signal sur bruit insuffisant pour révéler les raies spectrales du compagnon plus faible en compétition avec les raies spectrales du primaire plus dominant.

Il est important de noter que v_1 et v_2 ne sont pas observées directement, mais plutôt leurs projections selon notre ligne de visée. Autrement dit, les déplacements en longueurs d'onde observés sont dûs aux vitesses radiales en vertu de l'effet de Doppler. Ainsi, le déplacement d'une raie est corrélé avec la vitesse radiale de la manière suivante:

$$\frac{\lambda - \lambda_0}{\lambda_o} = \frac{\Delta\lambda}{\lambda_o} = \frac{\sqrt{1 - v_r/c}}{\sqrt{1 + v_r/c}} \approx \frac{v_r}{c}, \tag{1.21}$$

où c est la vitesse de la lumière, λ est la longueur d'onde observée, λ_o longueur d'onde au repos et la dernière approximation n'est valide que si $v_r \ll c$ (qui est juste pour la

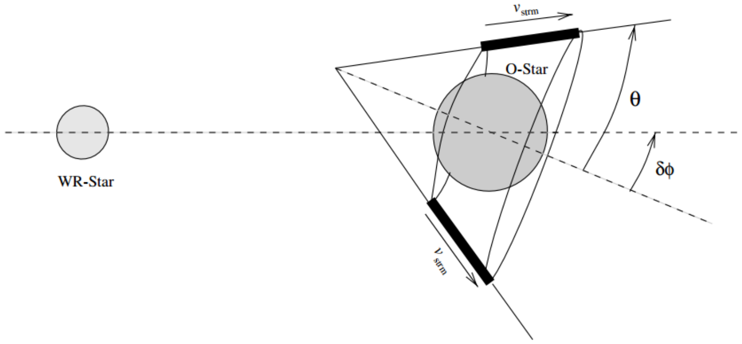

Figure 1.2: La géométrie simplifiée de la zone de collision de vents (tiré de Bartzakos et al. (2001)). La vraie zone sera plutôt de forme hyperbolique.

majorité d'orbites stellaires).

Pour les systèmes SB2, le rapport de masse peut être déduit facilement en sachant uniquement les amplitudes des deux mouvements orbitaux. Cependant, sans information sur l'angle d'inclinaison, il n'est pas possible de déterminer les masses individuellement. Encore moins d'information peut être obtenue pour les systèmes SB1. En manipulant les termes de la troisième loi de Kepler, la quantité,

$$f(M_1) = \frac{M_2^3 \sin^3 i}{(M_1 + M_2)^2} = \frac{PK_1^3}{2\pi G}(1-e^2)^{3/2}, \tag{1.22}$$

est connu sous le nom de la fonction de masse et est souvent introduite pour coupler les masses et l'inclinaison en une seule expression.

1.2.5 Variabilités polarimétriques

La polarisation totale d'une étoile simple entourée d'une enveloppe circumstellaire fortement ionisée à symétrie sphérique serait en principe nulle. Par contre, la présence d'un compagnon a pour effet d'introduire des asymétries au système. Ainsi, la perte de symétrie sphérique peut mener à une petite polarisation linéaire du système.

Brown, McLean & Emslie (1978), ci-après, BME, ont déterminé analytiquement la polarisation linéaire produite par la diffusion Thompson d'une source ponctuelle dans une enveloppe optiquement mince de densité arbitraire. L'intérêt d'utiliser cette technique est qu'elle s'étend pas seulement aux binaires éclipsantes (dans le cas des WR+O, un peu comme les éclipses atmosphériques). Effectivement, peu importe l'angle d'inclinaison, des modulations synchronisées avec la phase orbitale sont observées dans les paramètres de Stokes Q et U. Ainsi, cette théorie s'applique pleinement dans le cadre des binaires WR+O où la lumière de l'étoile O, assujettie aux vents stellaires de l'étoile WR, est diffusée par les électrons libres de cette dernière, ce qui provoque une polarisation linéaire qui varie le long de l'orbite. Cette technique permet de déterminer, entre autres, le taux de perte masse de l'étoile WR (insensible au clumping); une application directe est présentée à la section 3.4 du chapitre 2.

1.2.6 Variabilités photométriques

Les binaires à éclipses sont des systèmes binaires dont l'angle d'inclinaison est suffisamment élevé de telle sorte qu'une étoile occulte de manière périodique au moins une partie de la lumière de l'autre. Ces éclipses se manifestent dans une courbe de lumière comme des chutes périodiques en intensité, typiquement deux, une pour chaque étoile, par cycle orbital. L'intérêt d'observer ces systèmes réside dans la capacité d'obtenir non seulement l'ensemble des paramètres orbitaux, mais aussi les propriétés physiques des étoiles telles que leurs tailles et luminosités.

Bien que ces systèmes à éclipses soient fondamentaux à la déterminatins des paramétres orbitaux des systèmes binaires, ils sont plutôt rares à observer. Ainsi, Lamontagne et al. (1996) ont élaboré un modèle d'éclipse atmosphérique permettant de décrire les variations photométriques dans un cas plus large des systèmes binaires WR+O. Il s'agit d'un modèle géométrique qui caractérise la diffusion électronique de Thomson périodique de la lumière de l'étoile O orbitant autour de l'étoile WR. Cette méthode permet d'obtenir des quantités fondamentales, telles que le taux de perte de masse de l'étoile WR, indépendamment du clumping, et est discutée davantage à la section 3.5 du chapitre 2.

1.3 Les étoiles en cavales

La vitesse particulière (« peculiar velocity ») d'une étoile dans la Galaxie correspond à sa vitesse spatiale par rapport au référentiel au repos local (« local standard of rest » , LSR), c'est-à-dire, le référentiel suivant le mouvement moyen des étoiles de la Voie lactée au voisinage du Soleil. La plupart des étoiles massives OB possèdent des vitesses particulières au voisinage de $15\,\mathrm{km\,s^{-1}}$ (Stone, 1991). Par contre, certaines étoiles acquièrent de très grandes vitesses particulières au-delà de $35\,\mathrm{km\,s^{-1}}$ allant même jusqu'à $200\,\mathrm{km\,s^{-1}}$ (Moffat et al., 1998); Elles sont dites des étoiles en cavales.

1.3.1 Les mécanismes d'éjection

Si les étoiles en cavales sont éjectées perpendiculairement, ou presque, du plan Galactique (GP), elles peuvent se retrouver très fortement éloignées du GP. Il y a deux méthodes pour les produire: éjection par supernova dans un système binaire (Blaauw, 1961) ou bien par interactions gravitationnelles dans un amas jeune en formation (Poveda et al., 1967).

Éjection Supernova

Dans un système binaire, l'impact d'une explosion supernova peut provoquer la rupture du système binaire dans $\sim 80-90\%$ des cas (Eldridge et al., 2011). Les explosions SN sont caractérisées par une éjection de masse instantanée. Les deux composantes des systèmes découplés gravitationnellement peuvent s'en échapper avec de grandes vitesses particulières. Les systèmes qui demeurent liés reçoivent aussi un recul systémique, quoique moins significatif. Dans ce qui suit, nous allons uniquement considérer des systèmes en orbite circulaire instantanément avant l'explosion SN. Cette supposition se justifie par le fait que les binaires massives serrées ont tendance à se circulariser généralement bien avant l'explosion SN du primaire (van den Heuvel, 1994).

Explosions supernovae symétriques

Un système demeure lié suite à une explosion SN symétrique (c'est-à-dire, que l'éjection de masse est isotrope) si moins de la moitié de la masse totale initiale est éjectée (Vanbeveren, 1998),

$$\Delta M < \frac{1}{2}(M_1 + M_2), \tag{1.23}$$

où $M = M_1 + M_2$ est la masse totale avant la SN, $\Delta M = M - M'$ est la perte de masse due à la SN et $M' = M_1' + M_2$ est la masse totale après la SN (on suppose que M_2 reste constant). Autrement, le système binaire se dissocie et éjecte les deux composantes. Ce critère sera toujours respecté si, au moment de l'explosion SN, la masse du primaire est inférieure à celle du secondaire. Cela est souvent le cas pour les systèmes binaires massifs, car le primaire aura déjà perdu beaucoup de sa masse soit via ses vents stellaires ou via RLOF qui peut aussi augmenter la masse du secondaire. Par conséquent, les systèmes binaires massifs demeureront toujours liés suite à une explosion SN symétrique. Or, la disparité des HMXRBs (contrairement à l'abondance des systèmes binaires O+O) suggère que les explosions SN seront en fait plutôt asymétriques.

Explosions supernovas asymétriques

Une explosion SN asymétrique (c'est-à-dire que l'éjection de masse est anisotrope) induit un recul supplémentaire au système binaire. Dans ce cas si, la condition de stabilité devient (Vanbeveren, 1998),

$$\Delta M < \frac{1}{2}(M_1 + M_2)\left[1 - \left(\frac{w}{v_{\text{orb}}}\right)^2 - cos\theta\left(\frac{w}{v_{\text{orb}}}\right)\right], \tag{1.24}$$

où w est la vitesse du recul SN, v_{orb} est la vitesse relative des deux étoiles avant la SN et θ est l'angle entre w et v_{orb}. La direction du recul SN influence la stabilité de l'orbite. Plus concrètement, w dans la direction de v_{orb} favorise la rupture du système, tandis que, w en direction opposée de v_{orb} encourage le système à demeurer lié. D'ailleurs, l'explosion SN perturbe la période de l'orbite et transmet une excentricité au système (voir figure 1.3).

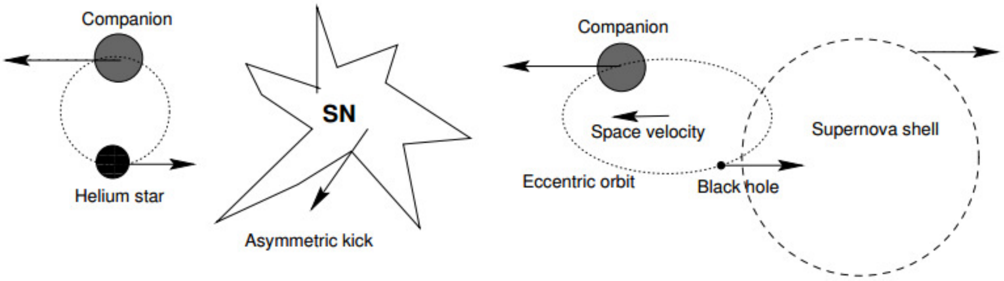

Figure 1.3: L'impact d'une explosion supernova dans un système binaire en trois phases distinctes (tiré de Nelemans (2007)).

Un système qui demeure lié obtient une vitesse d'éjection de,

$$V_{\text{ejt}} = \frac{v_{\text{orb}}}{M_1' + M_2}\left[\left(\frac{M_2 \Delta M}{M_1 + M_2}\right)^2 - 2\frac{M_2 M_1' \Delta M}{M_1 + M_2}\left(\frac{w}{v_{orb}}\right)\cos\theta + \left(M_1'\left(\frac{w}{v_{\text{orb}}}\right)\right)^2\right]^{1/2}, \tag{1.25}$$

alors que les membres d'un système binaire dissocié sont éjectés avec leurs vitesses orbitales instantanément avant la SN,

$$V_{\text{ejt},1} = \frac{M_1}{M_1 + M_2} v_{\text{orb}} \qquad \text{et} \qquad V_{\text{ejt},2} = \frac{M_1}{M_1 + M_2} v_{\text{orb}}. \tag{1.26}$$

Éjection dynamique

Dans de jeunes et denses amas stellaires, l'interaction gravitationnelle entre les étoiles peut éjecter une ou plusieurs composantes des systèmes multiples. Les interactions à trois- ou à quatre-corps sont notamment efficaces pour générer les étoiles en cavales les plus rapides. Dans les deux cas, il n'y a pas d'expressions analytiques pour exprimer la vitesse d'échappement des étoiles éjectées.

Interactions à trois-corps

Ce type d'interaction est caractérisé par des diffusions entre un système binaire et un corps simple. Si l'énergie totale d'une telle interaction est positive, il y a une ionisation. Cela mène à la rupture du système binaire dont chacune des étoiles s'en sort non liée. Si au contraire, l'énergie totale est négative, il y a un échange. Cela implique la formation d'un nouveau système binaire éjectant l'autre étoile simple. Si aucune interaction ne se produit, on dit qu'il y a eu préservation.

Interactions à quatre-corps

Ce type d'interaction est caractérisé par des diffusions entre deux systèmes binaires. La combinaison des trois cas précédents donne lieu à six possibilités (voir figure 1.4):

1. préservation: même deux systèmes binaires initiaux demeurent liés.
2. échange : échange entre un membre de chaque système binaire formant deux nouveaux systèmes binaires.
3. ionisation: ionisation (rupture) d'un système binaire résultant à l'éjection de deux étoiles simples et d'un système binaire.
4. échange et ionisation: échange suivi par une ionisation formant un nouveau système binaire et éjectant deux étoiles simples.
5. ionisation totale: ionisation (rupture) des deux systèmes binaires résultant à l'éjection de quatre étoiles simples.
6. triple: formation d'un système triple et éjection d'une étoile simple.

Les deux mécanismes d'éjection ont été vastement étudiés par Leonard (1993) via des synthèses de population (pour les éjections supernova) et des simulations à N corps (pour les éjections dynamiques). Dans les deux cas, ce sont les étoiles de plus faible masses qui atteignent les plus grandes vitesses et leurs distributions de vitesses sont quasi Maxwelliennes (voir figure 1.5). Ainsi, les systèmes binaires en cavales typiquement acquièrent des vitesses d'éjections inférieures à celles des étoiles simples. Cependant, les éjections dynamiques sont plus efficaces pour produire des étoiles en cavales à hautes vitesses.

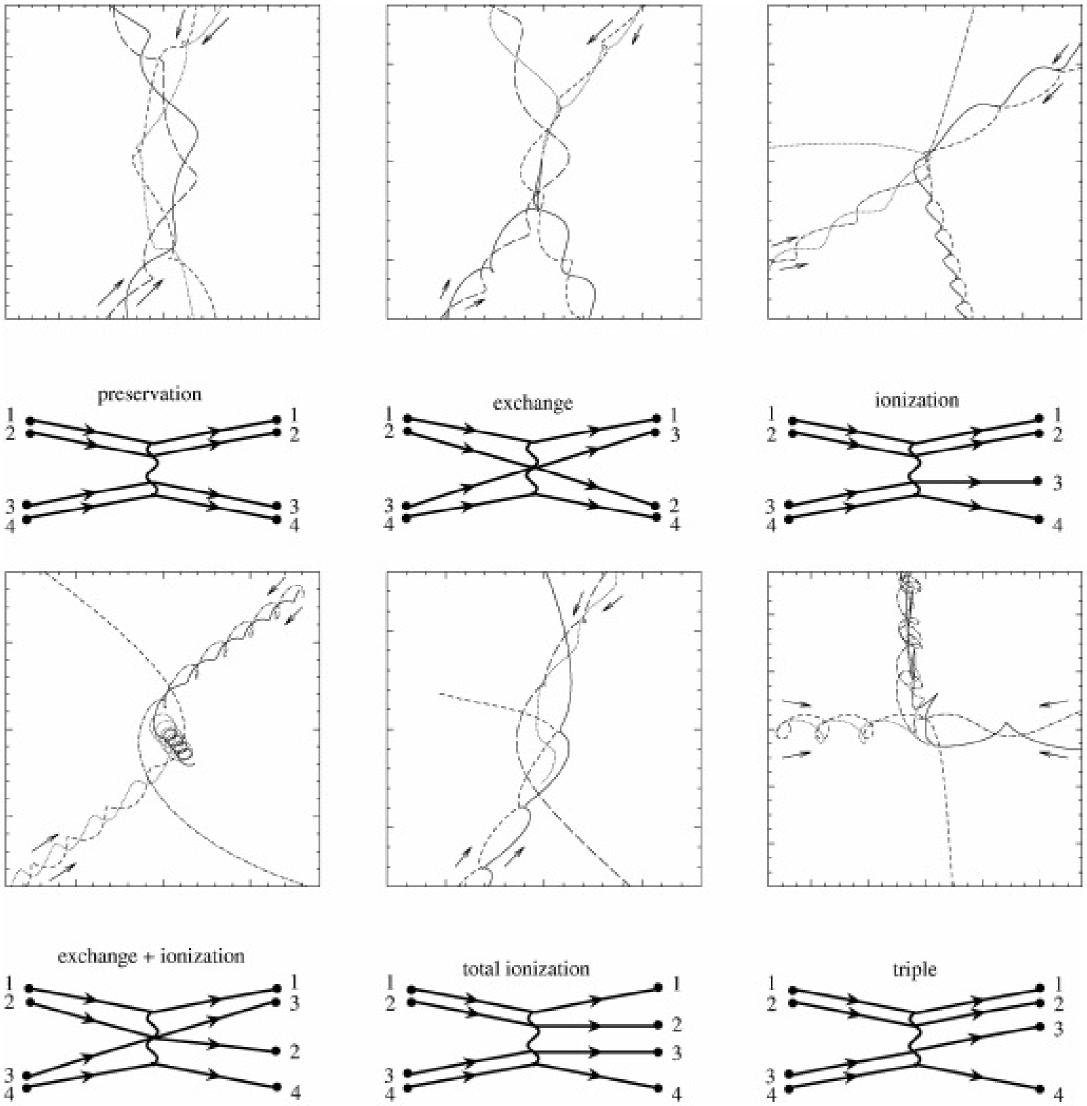

Figure 1.4: Résultats possibles des interactions binaires-binaires (tiré de Fregeau et al. (2007)).

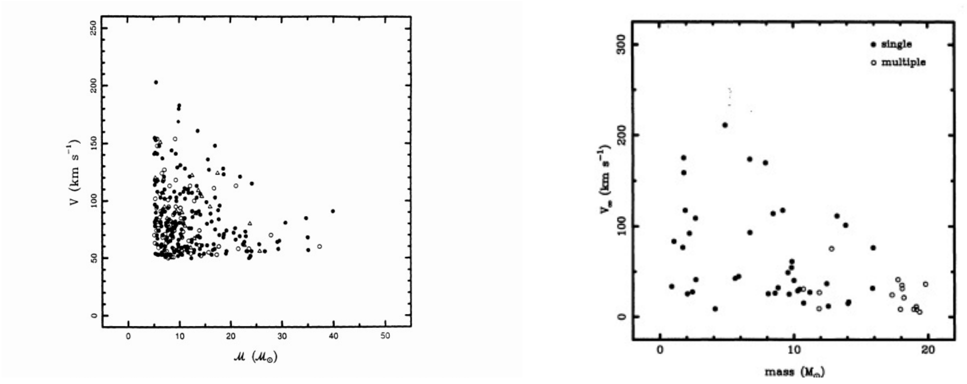

(a) (b)

Figure 1.5: Comparaison des distributions masses-vitesses des (a) éjections supernova (tiré de Leonard & Dewey (1993)) et (b) éjections dynamiques (tiré de Leonard & Duncan (1990a)). Les cercles pleins désignent les étoiles simples et les vides, les systèmes binaires.

1.3.2 L'intégration des orbites

Afin d'obtenir l'équation du mouvement d'une étoile en cavale, il faut d'abord connaitre le potentiel Galactique. Le potentiel Galactique de la Voie Lactée est exprimé en coordonnées Galactiques typiquement représentées en coordonnées cylindriques (r,ϕ,z) et est souvent décrit par la somme de trois composantes distinctes: un potentiel Miyamoto-Nagai pour le bulbe (Φ_b) et le disque (Φ_d) et un potentiel logarithmique pour le halo (Φ_h). Leurs expressions analytiques sont données par,

$$\begin{aligned}
\Phi_b(R) &= -\frac{M_b}{\sqrt{R^2+b_b^2}}, \\
\Phi_d(r,z) &= -\frac{M_d}{\sqrt{r^2+\left(a_d+\sqrt{z^2+b_d^2}\right)^2}}, \qquad (1.27) \\
\Phi_h(R) &= -\frac{M_h}{a_h}\ln\left(\frac{\sqrt{R^2+a_h^2}+a_h}{R}\right),
\end{aligned}$$

où $R = R(r,z) = \sqrt{r^2+z^2}$ et les paramètres M_b, M_d, M_h, b_b, a_d,b_d et a_h ont été déterminés par Irrgang et al. (2013) et sont présentés dans le tableau 1.I.

Table 1.I: Les constantes décrivant le potentiel Galactique.

Description	Paramètre	Unité	Valeur
Masse du bulbe	M_b	$[M_{\rm gal}]$	175
Masse du disque	M_d	$[M_{\rm gal}]$	2829
Masse du halo	M_h	$[M_{\rm gal}]$	69725
Hauteur d'échelle du bulbe	b_b	[kpc]	0.1840
Rayon caractéristique du disque	a_d	[kpc]	4.85
Hauteur d'échelle du disque	b_d	[kpc]	0.305
Rayon caractéristique du halo	a_h	[kpc]	200.0

Les masses sont données en unités Galactiques $M_{\rm gal} = 100 \times 1000^2\,{\rm kpc}\,/\,{\rm G}\,[SI]\,M_\odot \simeq 2.325 \times 10^7\,M_\odot$ de telle sorte que la constante Gravitationelle G est fixée à l'unité.

Les équations du mouvement d'une étoile sujette à un potentiel Galactique sont donc obtenues par,

$$\ddot{\mathbf{r}} = -\nabla\Phi(r,z) \tag{1.28}$$

Explicitant l'équation 1.28 en coordonnées cylindriques, on obtient six équations de mouvement sous la forme,

$$\begin{aligned} \dot{r} &= v_r, & \ddot{r} &= -\frac{\partial\Phi}{\partial r} + \frac{L_z}{2R^2}, \\ \dot{\phi} &= \tfrac{L_z}{r^2}, & \ddot{\phi} &= 0, \\ \dot{z} &= v_z, & \ddot{z} &= -\frac{\partial\Phi}{\partial z} + \frac{L_z}{2R^2}, \end{aligned} \tag{1.29}$$

où $\Phi = \Phi_b + \Phi_d + \Phi_h$ et L_z, le moment angulaire de l'étoile, est une quantité conservée. Ce système d'équations est résolu numériquement à l'aide d'un intégration Runge-Kutta d'ordre quatre.

Pour déterminer la vitesse spatiale d'une étoile en coordonnées cylindriques, il faut faire la transformation de coordonnées équatoriales (référentiel centré autour de la Terre) jusqu'aux coordonnées Galactocentriques (référentiel centré autour du centre Galactique). Ceci se fait en trois étapes par le passage intermédiaire aux coordonnées Galactiques (référentiel centré autour du soleil):

La première étape s'effectue en appliquant successivement trois matrices de rotation

Coordonnées équatoriales	$\longrightarrow$	Coordonnées Galactiques	$\longrightarrow$	Coordonées Galactocentriques
(α,δ,d)		(l,b,d)		(r,ϕ,z)

afin d'aligner le système d'axes initial déterminé avec les angles équatoriaux (α,δ) vers un système d'axes déterminé avec les angles galactiques (l,b). Enuite, pour passer d'un système centré autour du soleil vers un centré autour du centre Galactique, il suffit de faire une translation de $\sim 8.3\,\mathrm{kpc}$. Ces transformations sont souvent traitées en coordonnées cartésiennes. Ainsi, la dernière étape consiste à faire une transformation triviale de représentation cartésienne à cylindrique.

1.4 Résumé

Les notions de bases abordées dans les sections précédentes permettront d'embarquer le lecteur pleinement au coeur du projet de mémoire. Des applications concrètes des techniques spectroscopiques, polarimétriques et photométriques décrites aux sections 1.2.4, 1.2.5 et 1.2.6 respectivement seront présentées dans les chapitres suivants afin d'identifier la nature du compagnon des deux systèmes binaires WR 148 et WR 71. La caractérisation d'autres phénomenes communément observables dans les étoiles massives, tels que des collisions de vents ou des CIRs serait également mis en pratique. Par ailleurs, dans le but de mieux comprendre l'emplacement géométriques des deux systèmes en cavales, leurs équations de mouvements sont dérivées et intégrées numériquement dans le passée jusqu'à leur site d'éjection initiale du plan galactique. Cette exercise nous renseigne, entre autres, sur le temps écoulé depuis leurs ejection qui fourni donc une borne inférieure sur leurs age.

CHAPTER 2

WR 148: L'IDENTIFICATION DU COMPAGNON

L'article qui suit présente une étude spectroscopique de WR 148. Il s'agit d'un système binaire constitué d'une étoile WR du type WN7h et d'un compagnon soupçonné d'être soit une étoile B de masse intermédiaire ou bien un trou noir. Bracher (1979) a déterminé une période orbitale de 4.3174 jours dont la précision a depuis été améliorée par les efforts combiné de Moffat & Seggewiss (1979), Drissen et al. (1986) et Marchenko et al. (1996). Il s'avère que la périodicité est demeurée essentiellement constante (tout au long des multiples observations), tandis que la nature du compagnon demeure toujours inconnue. Afin d'identifier le compagnon, nous avons obtenu plusieurs spectres de l'OMM suivis par deux nuits de spectres à l'Observatoire Keck. La détermination de la nature du compagnon permettra de restraindre les scénarios possibles qui ont pu mener à l'éjection du système hors du GP.

Mes contributions correspondent à la réduction et l'analyse des dommées OMM, ainsi qu'à la reconstruction 3D des vitesses spatiales de WR 148. Le co-auteur Grant Hill a obtenu et réduit les données de l'Observatoire Keck. Tomer Shenar a traité les fits spectroscopiques utilisant les modèles PoWR. Guidé par Anthony Moffat, les co-auteurs Nicole St-Louis, Noel Richardon, Herbert Pablo et Tahina Ramiaramanantsoa ont tous fourni des commentaires constructifs et fondamentaux à la rédaction de l'article. Enfin, l'article a été entièrement rédigé par moi-même.

L'article a été soumis et sa mise en forme originale a été adaptée pour être inclus dans le texte.

Muñoz, M., Moffat, A.F.J., Hill, G.M., Shenar, T., Richardson, N.D., Pablo, H., St-Louis, N., Ramiaramanantsoa, T. (2016). WR 148: Identifying the companion of an extreme runaway massive binary.
Monthly notices of the royal astronomical society
Article soumis: 10 Février 2016

WR 148: Identifying the companion of an extreme runaway massive binary.

Melissa Muñoz,[1] Anthony F. J. Moffat,[1] Hill M. Grant,[2] Tomer Shenar,[3] Noel D. Richardson,[4] Herbert Pablo,[1] Nicole St-Louis,[1] Tahina Ramiaramanantsoa[1]

[1]*Département de Physique, Université de Montréal, and Centre de Recherche en Astrophysique du Quebec, CP 6128, Succursale, Montréal, QC H3C 3J7, Canada*
[2]*W.M. Keck Observatory, 65-1120 Mamalohoa, Kamuela, HI 96743, USA*
[3]*Institut fürr Physik und Astronomie, Universität Potsdam, Karl-Liebknecht-Str. 24/25, 14476, Potsdam, Germany*
[4]*Ritter Observatory, Department of Physics and Astronomy, The University of Toledo, Toledo, OH 43606-3390, USA*

Abstract

WR 148 (HD 197406) is an extreme runaway system considered to be a potential candidate for a short-period (4.3173 d) rare WR + compact object binary. Provided with new high resolution, high signal-to-noise spectra from the Keck observatory, we at last detect direct signatures from the companion. From this, we determine the orbital parameters for both the primary WR and the secondary, yielding respective projected orbital velocity amplitudes of $88.1 \pm 3.8\,\mathrm{km\,s^{-1}}$ and $79.2 \pm 3.1\,\mathrm{km\,s^{-1}}$ and implying a mass ratio of 1.1 ± 0.1. We then apply the shift-and-add technique to disentangle the spectra and obtain spectra compatible with a WN7ha and an O4-6 star. Considering an orbital inclination of $\sim 67^{\circ}$, derived from previous polarimetry observations, the system's total mass would be a mere 2-3 Msol, an unprecedented result for a putative massive binary system. However, a system comprising a $37 M_{\odot}$ secondary (typical mass of an O5V star) and a $33 M_{\odot}$ primary (given the mass ratio) would infer an inclination of $\sim 18^{\circ}$. We therefore reconsider the previous methods of deriving the orbital inclination based on time-dependent polarimetry and photometry. While the polarimetric results are inconclusive, requiring better data, the photometric results favour low inclinations. Finally, we compute WR 148's space velocity and retrace the runaway's trajectory back to the Galactic plane (GP). With an ejection velocity of $198 \pm 27\,\mathrm{km\,s^{-1}}$ and a travel time of $4.7 \pm 0.8\,\mathrm{Myr}$ to reach its current location, WR 148 was most likely ejected via dynamical interactions in a young cluster.

Keywords: binaries: spectroscopic – stars: individual: WR 148 – stars: mass-loss – stars: winds, outflows – stars: Wolf-Rayet – stars: kinematics and dynamics.

2.1 Introduction

Current massive-star evolution theories agree that Wolf-Rayet (WR) stars originate from O-type main sequence stars (Crowther, 2007). Thus, we expect a commonplace O+O binary system to evolve into an O+cc (compact companion), i.e. a high mass X-ray binary (HMXRB) if they remain bound after the first supernova explosion (SN). Recent population synthesis models suggest that roughly 80-95 % of the O+O binaries are disrupted subsequent to the SN (Eldridge et al., 2011; Postnov & Yungelson, 2014b). The surviving O+cc systems are then expected to progess to a WR+cc system. Yet, while the number of known O + cc sytems is significant, the number of detected WR+cc systems is much lower than predicted. In fact, while there are a total of 114 confirmed HMXRBs (Liu et al., 2006) in our Galaxy, there is only a single confirmed WR+cc binary, Cyg X-3 (Tutukov et al., 2013a), compared to the ~ 10 expected based on the Galactic fraction of WR- to O- stars (van der Hucht, 2001).

HD 197406 (WR 148) is a well known candidate for such WR+cc systems. It is a single-lined spectroscopic binary with a well established ~ 4.3173 d orbital period where the unseen companion was suspected to be either a low mass B2-B5 V-III star or a black hole (BH) (Marchenko et al., 1996). Found at roughly 800 pc above the Galactic plane (Rosslowe & Crowther, 2015), HD 197406 is an extreme runaway with a high peculiar velocity. The compact companion is therefore an interesting possibility, as the recoil of the supernova explosion could have ejected the binary from the Galactic plane without breaking it up. The major shortfall of this hypothesis is the presence of a thermal X-ray spectrum (Zhekov, 2012), typical for WR+O colliding wind binaires, rather than a hard spectrum generally observed in accreating massive X-ray binaries.

The purpose of this investigation is therefore to determine the nature of the secondary in WR 148 and understand the evolutionary path of WR 148 as a unique runaway WR binary. In order to do so, we have acquired high resolution, very high signal-to-noise spectra at the Keck Observatory at both quadratures, complemented with a dozen lower quality spectra at the Observatoire du Mont Mégantic (OMM) during the summers of 2014 and 2015. The OMM data will serve mostly to refine the system's orbital parameters based on the bright primary WR component, whereas the Keck data will be used in an attempt to determine the nature of the companion.

The rest of the paper is organized as follows: We begin by describing the details of the observations in section 2.2. This is followed by a thorough analysis of the observational data in section 2.3. Finally, in section 2.4, we briefly summarize the results.

2.2 Observational Data

Optical spectra were obtained during the summers of 2014 and 2015 at the Keck observatory and in 2014 at OMM. Table 2.I summarizes the details of the observations.

A total of 36 spectra were obtained over the course of a month with the Perkin-Elmer optical long slit spectrograph mounted at the Cassegrain focus of the 1.6-m telescope of OMM. Each spectrum was extracted and reduced individually using standard IRAF[1]

---

[1] IRAF is distributed by the National Optical Astronomy Observatories, which are operated by the Association of Universities for Research in Astronomy, Inc., under cooperative agreement with the National Science Foundation

techniques. If multiple exposures were taken during one night, they were combined in one or more multiples to ensure a minimal spread in phase of 10 %. Once combined, we acquired 13 spectra, each providing a signal-to-noise ratio (S/N) of $\simeq 250$ in the continuum.

WR 148 was observed for two nights at the Keck observatory with the Echellette Spectrograph and Imager (ESI) instrument at roughly opposite quadratures: phase $\simeq 0.28$ in the night of 2014 and phase $\simeq 0.73$, a year later, in 2015. At each quadrature, all spectra were combined to produce one high S/N spectrum well above 1000 per pixel in the continuum.

The data were rectified by selecting obvious regions of continuum and fitting a low order smooth function. For the echelle data, the overlaps in the orders were combined via a linear interpolation between pixels.

2.3 Analysis and Results

2.3.1 Orbital Elements

We measure the radial velocities (RVs) of the N IV λ4058 line by means of the bisector method (i.e. the RV refers to the centroid of the line). N IV λ4058 is a relatively strong, narrow and symmetric line that is formed quite deep in the WR wind and is thus suspected to best reflect the true orbital motion of the WR. Though it is not uncommom for a late WN (WNL) star to have its zero-point shifted by $\sim 10\,\mathrm{km\,s^{-1}}$ to negative values (Moffat & Seggewiss, 1979). The quality of the OMM data alone, when taken comparatively from one spectrum to another, is not sufficient to detect obvious

Table 2.I: Summary of spectroscopic observations.

Telescope	Dates		No. of spectra	Exp. Time [sec]	Spectral range [Å]	Resolving power	S/N (combined[†])
OMM (1.6 m)	2014	July 25 - August 23	36	1800	3800 - 5000	~3000	~250
Keck (10 m)	2014	July 24	49	120	3900 - 6900	~8000	~1000
Keck (10 m)	2015	July 15	42	120	3900 - 6900	~8000	~100

[†] combined in 13 groups for OMM, while all spectra were combined for each of the Keck dates.

signatures of the secondary. Therefore, the companion lines should not affect the RV measurements for the WR orbit from most lines, but especially from N IV λ4058. Applying the period finding algorithm described in Morbey & Brosterhus (1974), capable of processing multiple datasets with large gaps in time simultaneously, to the present measurements in addition to all available anterior spectroscopic observations allows us to improve WR 148's orbital solution. The prevous RV measurrements are provided from Bracher (1979), Moffat & Seggewiss (1979), Drissen et al. (1986) and Marchenko et al. (1996). As noted in Marchenko et al. (1996), in spite of the different methods used for the older determinations (e.g. fitting a parabola to the peak of the N IV λ4058 line or bisector method), the RVs are in accordance and no signifiant consequences were reported.

An elliptical orbit fit was first attempted followed by a circular fit (see Table 2.III). We note that the two sets of orbital elements have nearly the same quality of fit, as seen in the dispersion of the measured velocities of both fits being roughly identical: 24.10km s^{-1} for the elliptical fit and 24.06km s^{-1} for the circular fit. In a situation like this with a low eccentricity, the simple p_1 test described by Lucy (2005) quickly shows that the circular solution is strongly favoured. With the circular fit, we confirm and refine the previously reported period of P = 4.317336 d and time for phase zero (WR in front at inferior conjunction) of E = 2 444 825.04 HJD. The remaining orbital parameters are listed in Table 2.III and Fig. 2.1 displays the WR RV-curve. The refined orbtital solution is in agreement with the most recent analysis from Marchenko et al. (1996).

The Keck observations are of utmost importance for spectroscopically resolving this system. In fact, the higher resolution and higher S/N Keck data reveal the presence of absorption dips which move in clear anti-phase to the WR emission lines throughout the spectra in most of the H I, He I and He II lines. We identify four absorption lines that were particularly isolated to characterize the orbit of the secondary: He II λ4542, C IV $\lambda\lambda$5801, 5812 and O III λ5592. Of these lines, O III is the only absorption line unperturbed by WR emission lines. Most likely originating from the companion, we can deduce the secondary's gamma velocity, γ_2, and amplitude, K_2, from RV measurements at both epochs, assuming a circular orbit. The RVs of the absorption lines were derived

Table 2.II: Radial velocities for the WR component based on N IV λ4058 from OMM and Keck data.

HJD - 2 450 000	Orbital phase	RV [km s^{-1}] N IV λ4058
6864.7613	0.6922	-217.9 ± 7.2
6865.6098	0.8887	-158.7 ± 6.0
6865.7480	0.9208	-152.7 ± 6.7
6868.7376	0.6132	-197.5 ± 6.7
6868.8226	0.6329	-203.1 ± 6.9
6869.6056	0.8143	-216.4 ± 5.6
6869.7292	0.8429	-218.0 ± 6.2
6869.8249	0.8651	-209.6 ± 6.0
6870.6204	0.0493	-83.9 ± 6.1
6871.7661	0.3147	-31.9 ± 9.0
6889.7406	0.4780	-104.7 ± 8.4
6892.7523	0.1756	-56.4 ± 6.7
6892.8417	0.1963	-65.2 ± 5.9
6862.9773†	0.2790	-57.6 ± 2.6
7218.9720†	0.7360	-215.4 ± 3.4

†RV measurements are from Keck Observatory.

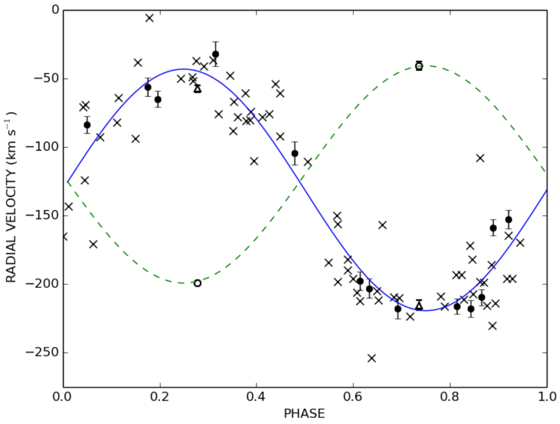

Figure 2.1: Radial velocity curve for the WR-star (blue solid line, based upon the N IV λ4058 line) and the O-type companion (green dashed line, based upon the He II λ4542, C IV $\lambda\lambda$5801, 5812 and O III λ5592. lines). The crosses correspond to all previous observations from Bracher (1979), Moffat & Seggewiss (1979), Drissen et al. (1986) and Marchenko et al. (1996) and the filled circles to the most recent 2014 observations from OMM. The hollow triangles and circles correspond to the Keck measurement for the WR and companion, respectively.

Table 2.III: Orbital Elements for the WR component and derived quantities. $f(m_1)$ is the mass function for the WR-star given by $f(m_1) \equiv PK_1^3/2\pi G = (m_2 \sin i)^3/(m_1+m_2)^2$.

Parameter	Elliptical fit	Circular fit
P [days]	4.317340 ± 0.000026	4.317336 ± 0.000026
T_0 [HJD - 2,440,000]	4818.5 ± 0.8	-
E [HJD - 2,440,000]	-	4825.04 ± 0.03
e	0.05 ± 0.04	0 (fixed)
ω [deg]	79.9 ± 64.7	-
K_1 [$\mathrm{km\,s^{-1}}$]	88.1 ± 3.8	88.1 ± 3.8
γ_1 [$\mathrm{km\,s^{-1}}$]	-131.9 ± 2.7	-131.4 ± 2.7
$a_1 \sin i$ [$R_\odot$]	7.5 ± 0.3	7.5 ± 0.3
$f(m_1)$ [$M_\odot$]	0.30 ± 0.04	0.30 ± 0.04

by fitting a Gaussian to the trough of the line and are tabulated in Table 2.IV. The resulting γ_2 and K_2 values are provided in Table 2.V. We note that, at the first quadrature, the C IV λ5801 absorption line is slightly contaminated by a superimposed diffuse interstellar band (DIB) at λ5796.98 (Herbig, 1995). An attempt was made to remove this DIB by subtracting a DIB profile obtained from the first qudrature to the second (see Fig. 2.2). However, we note an increase of DIB depth from the first quadrature to the second. This can seen at the DIB near $\sim$ 5595 Å(Herbig, 1995) in figure 2.2. Consequently, the correction will likely be underestimated. In spite of this, the calculated γ_2 and K_2 velocities tie in well with respective values of $-120.1 \pm 1.2\,\mathrm{km\,s^{-1}}$ and $79.2 \pm 3.1\,\mathrm{km\,s^{-1}}$.

Marchenko et al. (1996) did report the presecence of weak absorption features on top of Hγ λ4340 and He I λ4471. Presumed to arise from the companion, Marchenko et al. (1996) obtained $K_1 = 87.7 \pm 2.4\mathrm{km\,s^{-1}}$ and $K_2 = 36.2 \pm 2.4\mathrm{km\,s^{-1}}$. While K_1 is compatible with our result, K_2 is not. However, the RV's for the companion were only seen and measured on 3 (for Hγ λ4340) or 6 (for He IV λ4471) of their 22 collected spectra. Given the sparsity of their measurents, the orbital solution may be unreliable. Futhermore, as the absorption dips are heavily blended with the WR emission lines, we suspect that some measurements could have been inaccurate.

We point out that the companion's systemic velocity differs slightly from that of the WR-star. Although the two values are marginally the same within the errors, we keep in mind that the WR's radial velocity is solely based upon the ability of the N IV λ4058

Table 2.IV: Radial velocities for the companion based on He II λ4542, C IV λ5801, C IV λ5812 and O III λ5592 from Keck data (assuming period and time of phase zero from the WR component).

HJD - 2 450 000	Orbital phase	RV [km s^{-1}]			
		He II λ4542	C IV λ5801	C IV λ5812	O III λ5592
6862.9773	0.2790	-201.5 ± 2.6	-212.9 ± 2.7	-190.0 ± 3.0	-191.3 ± 2.4
7218.9720	0.7360	-38.5 ± 4.0	-33.5 ± 2.5	-41.7 ± 2.4	-51.2 ± 1.5

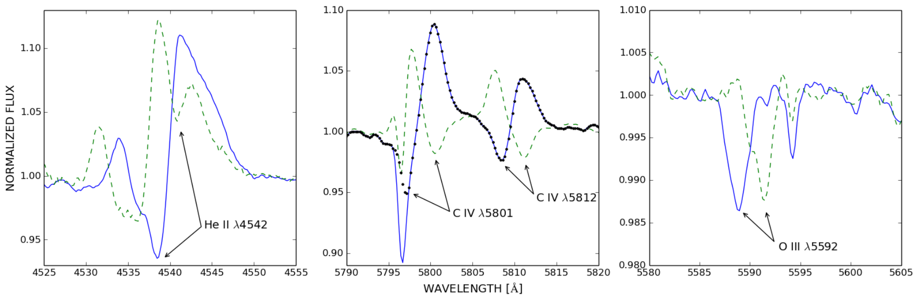

Figure 2.2: Most clearly revealed companion-star absorption lines from the Keck spectra, where measuring the RV was easily possible. The blue solid lines correspond to the first quadrature and the green dashed lines the second quadrature. The black dotted line is the attempted DIB-corrected spectrum for the first quadrature of the C IV line pair. The companion's absorption lines are indicated with arrows and are, from panels left to right, He II λ4542, C IV $\lambda\lambda$5801, 5812 and O III λ5592.

line to reflect the true orbital motion of the WR component. However, because of the WR-star's substantial stellar wind there is some leeway, and therefore the companion's systemic velocity may be more reliable (Moffat & Seggewiss, 1979). For this reason, we will adopt the companion's γ_2 as the true systemic velocity.

Interestingly enough, the K_1 and K_2 values are quite similar, which would imply a mass ratio on the order of unity. As stated in Drissen et al. (1986), an inclination angle of $\simeq 67°$ was derived from polarimetric variations. This would infer a total mass of the system

$$m_1 + m_2 = \frac{P}{2\pi G}\frac{(K_1 + K_2)^3}{\sin^3 i} \simeq 2.69\,M_\odot, \tag{2.1}$$

where subscript 1 refers to the WR-star and subscript 2 to the companion and G is the gravitational constant. Either we are dealing with a low-mass [WR] central star of a planetary nebula (CSPN) or a nova-like V Sge star (Steiner & Diaz, 1998) with a sub-dwarf OB companion, or the inclination angle is much lower than anticipated and the system is in fact a massive WR+OB binary. To resolve this situation, we attempt to rederive the orbital inclination via spectral classification of the secondary. With this new perspective, we review the previous polarimetric and photometric methods of determining i in order to merge all the information.

2.3.2 High or low mass?

Could WR 148 be a low-mass WR-star, i.e. a central star of a planetary nebula or a nova-like V Sge? Although almost all known [WR] stars belong to the carbon sequence [WC], a few [WN] stars were found in recent years (Miszalski et al., 2012; Todt et al.,

Table 2.V: Derived systemic velocities and amplitudes for the companion star from Table 2.IV

Line	K_2 [km s^{-1}]	γ_2 [km s^{-1}]
He II λ4542	82.3 ± 2.3	-120.5 ± 2.3
C IV λ5801	89.6 ± 2.5	-122.5 ± 2.3
C IV λ5812	74.9 ± 2.8	-116.3 ± 2.8
O III λ5592	72.0 ± 2.5	-122.9 ± 2.5

2010), and we therefore cannot reject the possibility of WR 148 being a rare case of a [WN] binary. While no nebular lines are present in the spectra at hand, this could be explained by the faintness of any surrounding nebula, or may even suggest a dissipation of the nebula due to binary interaction.

Unfortunately, [WR] (and V Sge) stars are virtually almost indistinguishable spectroscopically from their massive counterparts. While mass-loss rates of [WR] stars are clearly smaller than those of massive WR-stars, so are their emitting surfaces, leading to comparable equivalent widths of the emission lines in both types of stars. However, one somewhat subtle difference exists. Photons originating in recombination lines are scattered off free electrons in the WR wind and lead to the formation of so-called electron scattering wings (ESWs). ESWs form on both sides of the line (red and blue wings), but because the scattering electrons move outwards with the expanding stellar wind, the red wing is more prominent than the blue wing (Hillier, 1991). The strengths of these wings are directly proportional to the mass-loss rate and to the strengths of the recombination lines from which they stem. Since mass-loss rates of [WR] stars are at least an order of magnitude smaller than those of massive WR-stars, they are expected to show less pronounced or even vanishingly small ESWs.

Fig. 2.3 shows a comparison between our observed spectra of WR 148 (blue solid line) and Abell 48, a [WN] central star (red dashed line), focusing on the strong He II λ4686 line. Identifying the ESWs becomes easier when comparing the red and blue wings of the line. For each line, we measured the velocity corresponding to the blue edge of the line, i.e. where the profile reaches zero, v_{b}. We note that generally v_{b} need not be identical to v_∞, since the width depends on the line-formation region and the amount of electron scattering present. We find $v_{\mathrm{b}} = 850$ and $1500\,\mathrm{km\,s^{-1}}$ for WR 148 and Abell 48, respectively. The profiles shown in Fig. 2.3 are normalized to their respective peak intensities, and the wavelengths are transformed to the velocity space normalized to v_{b}.

Note how the spectrum of WR 148 exhibits a clear asymmetry towards the red part of the line. While the emission goes to zero at $-v_{\mathrm{b}}$ (per definition) on the blue side, there is clearly emission excess beyond v_{b} on the red side. This is a clear signature of the red ESW. In contrast, the profile exhibited by Abell 48 appears rather symmetric, just as one would expect in the case of a central star given their low mass-loss rates in an absolute sense. Its ESWs are almost undetectable. While the effect is subtle, it is apparent. Though the extent of the ESW will vary depending on the physical properties of the WR star, its presence should be noticeably larger in high-mass WR stars than low-mass [WR] stars, regardless of the ionization sequence. We also compared the ESWs exhibited by WR 148 with other massive WR-stars and find them to be similar in strength. This gives further evidence that the WR component of WR 148 is indeed a massive WR-star.

2.3.3 Spectral Classification

WR 148 was re-classified as a WN8h in Smith et al. (1996) according to 3D their classification guide. However, we reaffirm the former WN7 spectral type as quoted in van der Hucht (2001). This is based upon the line ratio of HeII $\lambda5411$ to HeI $\lambda5876$ (Peak/Continuum) totalling $\simeq 0.66$ for WR 148 (measured from the Keck spectra). Furthermore, the H^{+}/He^{++} fraction is well beyond the 0.5 threshold associated with WN7(h). Finally, with the added presence of intrinsic absorption lines we obtain WN7ha. A sample of the spectrum is shown in Fig. 2.4

The companion's spectral classification is based upon the ratio of the equivalent widths (EW) of He I $\lambda4471$ to He II $\lambda4542$ (Conti & Frost, 1977; Mathys, 1988). Since the OB absorption lines are blended with the WR emission lines, disentangling the spectra is crucial. We adopt the shift-and-add technique devised by Marchenko et al. (1998a). This procedure consists of first shifting all the spectra to the WR frame and creating a mean WR template. The latter is then subtracted from all the individual spectra and the result is shifted back to the O-star frame. Once combined, the output is the mean O-star spectrum. This is then substracted off the original spectra and the whole process is repeated as often as needed until a stable result is reached. Three iterations sufficed in this case.

This method requires knowledge of the orbital solution for both stellar components and warrants a dense enough data set with good phase coverage to smear out the companion's absorption lines. The Keck spectra supply the missing companion's orbital parameters, and are complementary to the OMM data, with evenly spaced phase cov-

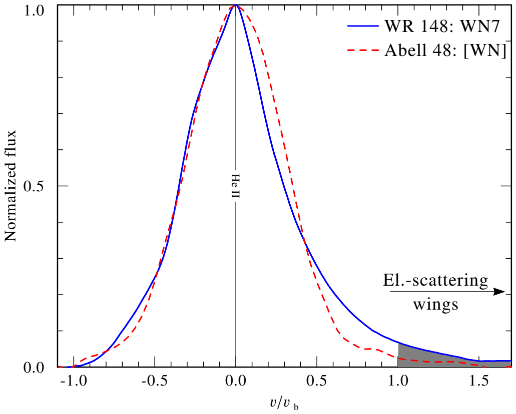

Figure 2.3: A comparison between the observed spectrum of WR 148 (blue solid line) and a low-mass [WN] star, Abell 48 (red dashed line). The observation of Abell 48 was obtained with the South African Large Telescope (SALT), see Todt et al. (2013) for further details.

erage. With these criteria fulfilled, we have extracted the mean O-star spectrum with only minor numerical artifacts on the companion's main He I and He II lines (see Fig. 2.5). Still, reconstructing the region between λ4600 - 4700 of the companion's spectrum was unsuccessful. In this region, the prominent features of the WR-star, (He II λ4686 and N III $\lambda\lambda$4634-4642 lines), are highly variable and overshadow the O-star absorption dips. Furthermore, a common residual side effect of this method is the presence of rounded emission-like edges on the absorption profiles. An accumulation of errors while subtracting the mean WR spectra from the individual spectra is most likely the cause.

Nonetheless, the He I line strengths are noticeably weaker than for He II. Measuring the EW of (the absorption part of) He I λ4471 and He II λ4542, yields $\log\left(EWHe\ \mathrm{I}\ \lambda 4471/EWHe\ \mathrm{II}\ \lambda 4524\right) = -0.51$. This corresponds to a spectral type of O5 for the companion (Mathys, 1988). For good measure, we will consider the O4 to O6 range as a reasonable uncertainty window. As for the companion's luminosity classification, the weak relative line strength (peak to continuum) of the secondary to the WR star suggets the secondary is a dwarf. If the secondary were to be a giant or especially a supergiant, the relative line strength would be larger than the observed value of ~ 0.2. We therefore presume the seconary is an O5V star.

We show in Fig.2.6 the spectra of the disentangled components plotted over the

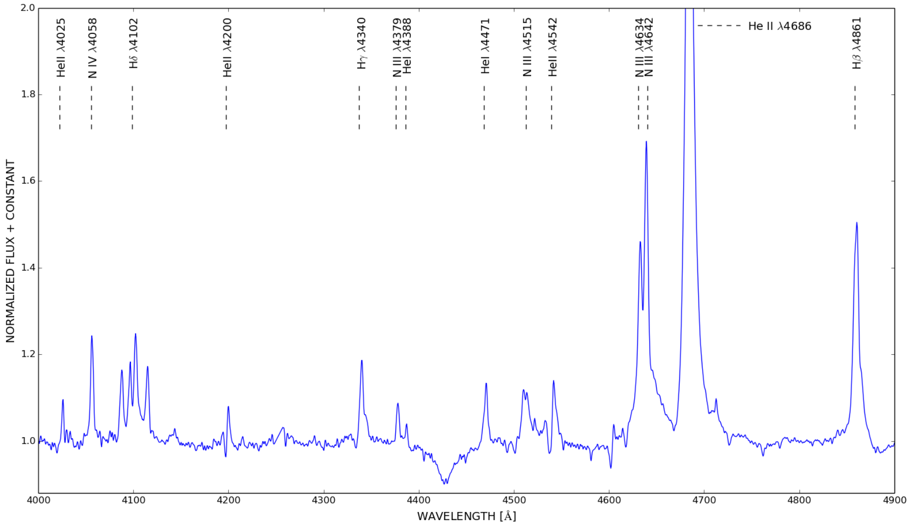

Figure 2.4: Sample of WR 148's spectrum from one of the 13 OMM combined spectra.

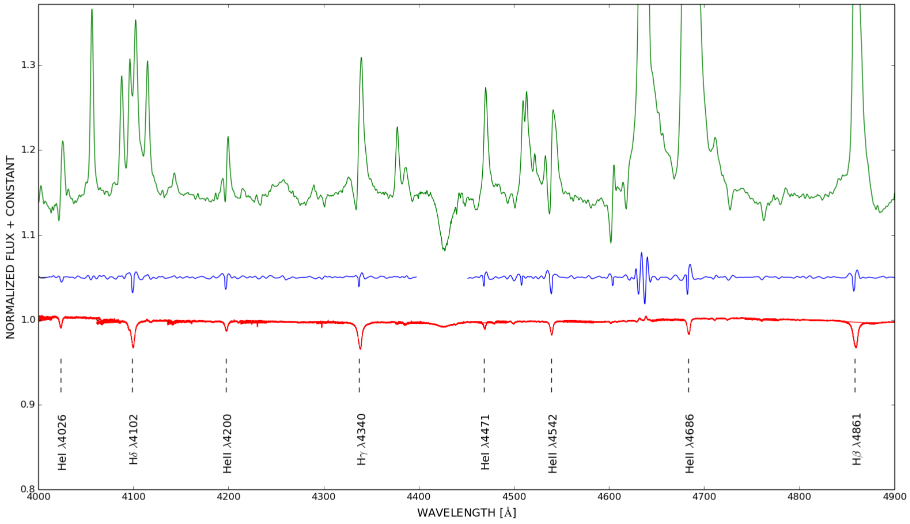

Figure 2.5: Mean spectra of the WR 148 components after applying the shift-and-add separation. Above is the WN7ha (shifted vertically for clarity) and beneath, the presumed O5V spectrum. Below, a spectrum of an O5V standard star (HD 46150) is shown for comparison purposes (provided from Petit et al., 2014). Note that the absolute line strengths are not preserved in this procedure.

blended spectra (from OMM at 0.61 phase) for both the He I λ4471 and He II λ4542 lines. The resulting disentangled spectra (i.e. sum of the WR-star and O-star separated spectra) concur with the blended OMM spectra and the He I λ4471 line is indeed significantly weaker than the He II λ4542 line. An improvement of the standard shift-and-add procedure from Marchenko et al. (1998a) can be done following the method from González & Levato (2006) where after each iteration, the RVs for both components are remeasured and consequently readjusted. Since N IV λ4058 is unaffected by the companion lines, no attempt was made to improve the WR's orbital solution. On the other hand, as convergence was acheived after only three iterations, no significant improvement was noted on the companion's orbital solution.

It is now possible to obtain the inclination angle via the mass function,

$$f(m_1) \equiv \frac{PK_1^3}{2\pi G} = \frac{(m_2 \sin i)^3}{(m_1 + m_2)^2} = 0.30 \pm 0.04\, M_\odot, \tag{2.2}$$

if the masses of both components are known. While the masses of WR-stars are not so well constrained based on their spectral types, the spectroscopic masses of OB-stars on the other hand are fairly well known as a function of spectral type. Knowing the mass ratio, $q = m_2/m_1 = K_1/K_2 = 1.1 \pm 0.1$, we therefore only need to determine the mass of the companion. For an O5V star, $M_O = 37\, M_\odot$ (Martins et al., 2005a) and thus $i = 18 \pm 4^\circ$. The uncertainty of ± 1 spectral class, has little affect on the inclination angle. This is because, at low inclinations, the values of the masses will vary drastically with only small changes of i on account of $\sin i$ being to the third power in equation 2.2 (see Fig. 2.7). We assume zero error on the luminosity class.

2.3.4 Revisiting the polarimetry

A linear polarization variability study on WR 148 was carried out by Drissen et al. (1986). An inclination of $\simeq 67^\circ$ was obtained by fitting separately the q_i and u_i Fourier

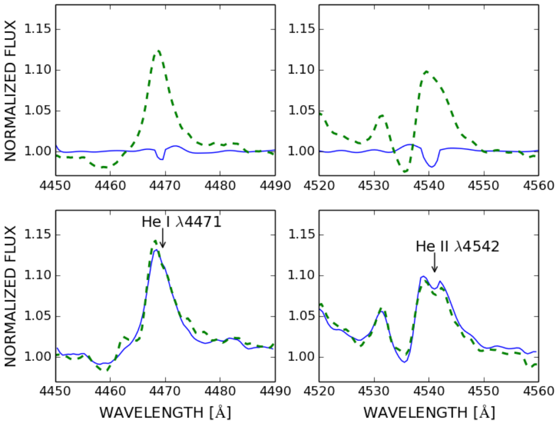

Figure 2.6: Top two panels: The indivual components of the disentagled spectra for the WR- (dashed curve) and O-star (solid curved) zoomed on the He I λ4471 (left panel) and He II λ4542 (right panel) lines. Bottom two panels: Comparison of the blended OMM spectra (dashed curve) and the sum of the disentangled components from the top panels (solid curve) for He I λ4471 (left panel) and He II λ4542 (right panel) at 0.61 orbital phase.

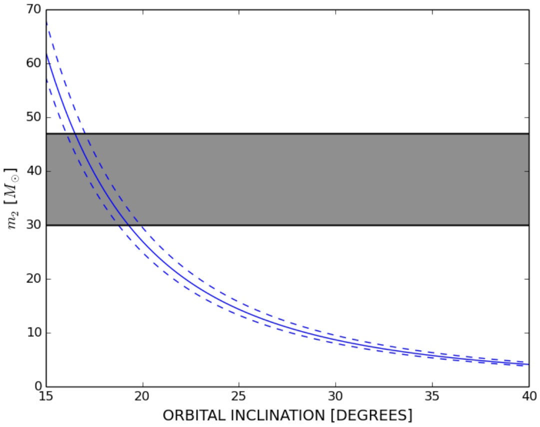

Figure 2.7: Mass of the companion as a function of orbital inclination for $q = 1.1$ (blue solid line) ± 0.1 (blue dashed lines). The shaded area corresponds to possible inclination angles given the uncertainties on spectral types. The upper limit is the mass of a typical O4 star and lower limit for an O6 star (Martins et al., 2005a)

coefficients to the following expressions for the Q and U Stokes parameters

$$\begin{aligned} Q &= q_0 + q_1\cos(\lambda) + q_2\sin(\lambda) + q_3\cos(2\lambda) + q_4\sin(2\lambda), \\ U &= u_0 + u_1\cos(\lambda) + u_2\sin(\lambda) + u_3\cos(2\lambda) + u_4\sin(2\lambda), \end{aligned} \tag{2.3}$$

where $\lambda = 2\pi\phi$ and ϕ is the orbital phase with WR inferior conjunction at $\phi = 0$.

This model can be further simplified assuming symmetry perpendicular to the orbital plane. Using the terminology from Brown, McLean & Emslie (1978), hereafter BME, this signifies that $\tau_1 = \tau_2 = 0$, where τ_i is the i^{th} electron density moment. Under these circumstances, equations (3) re-write to

$$\begin{aligned} Q &= Q_0 + \Delta Q\cos\Omega - \Delta U\sin\Omega, \\ U &= U_0 + \Delta Q\sin\Omega - \Delta U\cos\Omega, \end{aligned} \tag{2.4}$$

with

$$\begin{aligned} \Delta Q &= -H\left[(1+\cos^2 i)\cos 2(\lambda - \lambda_0) - \sin^2 i\right], \\ \Delta U &= -2H\cos i\sin 2(\lambda - \lambda_0), \end{aligned} \tag{2.5}$$

and

$$\begin{aligned} H &= \sqrt{\tau_3^2 + \tau_4^2}, \\ \tau_3 &= H\cos 2\lambda_0, \\ \tau_4 &= -H\sin 2\lambda_0, \end{aligned} \tag{2.6}$$

where Q_0 and U_0 are interstellar values, Ω is the rotation angle of the line of nodes on the sky, τ_3 and τ_4 are the third and fourth electron density moments and λ_0 is a constant.

By explicitly expressing the q_i and u_i coefficients as a function of the independent parameters (Q_0, U_0, i, Ω, H and λ_0), it becomes apparent that the coefficients are in fact all coupled. Therefore, rather than fitting Q and U with q_i and u_i as free parameters, we fit Q and U simultaneously with Q_0, U_0 i, Ω, H and λ_0 as free parameters via a non-linear least squares routine. A Levenburg-Marquardt algorithm was used here through the python module LMFIT (Newville et al., 2014).

From equation 2.6, we can see that τ_4 introduces a phase shift, λ_0. However, in the case of axial symmetry in the orbital plane about the WR, $\tau_4 = 0$ and consequently $\lambda_0 = 0$. Since we are uncertain about the asymmetries in the plane, we will consider two fitting scenarios:

1. Case A : $\tau_1 = \tau_2 = 0$; $\tau_3 \neq \tau_4 \neq 0$ ($\lambda_0 \neq 0$)
2. Case B : $\tau_1 = \tau_2 = \tau_4 = 0$; $\tau_3 \neq 0$ ($\lambda_0 = 0$)

Case B will be further subdivided in Ba and Bb where the inclination angle will be fixed at either 18° or 67°, respectively.

In case A, the values of the fitted parameters yield similar results to Drissen et al. (1986) (see Table 2.VI) with a new inclination of $\sim 69^\circ$ as opposed to the previous $\sim 67^\circ$. This slight difference is likely due to the new ephemeris and period adopted for phase folding the polarimetric data. The only caveat in this case is the justification for the phase shift relative to phase $\phi = 0$ (WR in front). Additional free electrons originating from a colliding-wind shock cone may be responsible. Consequently, a small positive phase shift may be expected in the presence of a strong aberration effect involving the wind-expansion and orbital speeds twisting the shape of the shock cone. While some authors consider this effect to be negligible (Moffat et al., 1998), it has been shown to exist and needed to explain some observations (Lomax et al., 2015). However, as seen below in section 2.3.6, the aberration angle in the modelled wind-wind collision zone does in fact appear to be negligible. This is indicative that the case B fits may be more appropriate for WR 148.

Table 2.VI: Best-Fitting values for the BME polarization model

Parameter	Case A	Case Ba	Case Bb
i (deg)	69.4 ± 1.9	18 (fixed)	67 (fixed)
Q_0(%)	-0.58 ± 0.02	-0.773 ± 0.014	-0.58 ± 0.02
U_0(%)	-0.70 ± 0.02	-0.535 ± 0.014	-0.51 ± 0.02
Ω (deg)	145.1 ± 3.6	196.9 ± 3.5	190.8 ± 4.0
H (%)	0.17 ± 0.04	0.121 ± 0.008	0.231 ± 0.016
λ_0 (deg)	26 ± 5	0 (fixed)	0 (fixed)

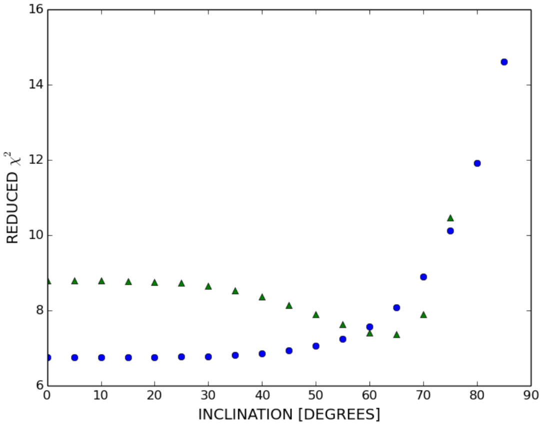

Figure 2.8: Reduced χ^2 as a function of orbital inclination for the polarimetric model. The green triangles correspond to case A and the blue circles to case B.

Regarding case B, the fitting procedure is arguably more difficult. This is because of the loss of a free parameter, λ_0, resulting in a fit with unrealistically large errors, thus rendering the values of the optimized parameters meaningless. Instead, we proceed by fitting four parametrs and fixing the last one, inclination. Fixed inclination values range from 0° to 90° with an increment of 5°. At each inclination angle, the reduced χ^2 is calculated for the observed Q and U values to the models in equation 2.4 as a means to compare with the other fits. For consistency, the reduced χ^2 was also computed for case A. The results are illustrated in Fig. 2.8.

According to the reduced χ^2, it appears that, for case B, the goodness of the fits increases as i decreases. This is true until $\sim 50^\circ$, below which, the fits are seemingly identical. That being said, there is a clear global minimum in the reduced χ^2 for case A. The question remains whether the dip is significant or not. Considering that the reduced χ^2 are rather far from 1, the best value for an ideal fit, no case formally fits well. This may be caused by a combination of underestimated observational errors (Bastien et al., 1988) or intrinsic variability of the stellar wind (e.g. due to clumpy structures).

Fig. 2.9 shows the fitted Q and U curves as a function of orbital phase at the optimized angle of 69° for case A and at both the newly and previously determined angles of 18° and 67° for cases Ba and Bb, respectively. No fit appears to be strongly favoured.

However, the same cannot be said for the fits in the Q-U plane (see Fig. 2.10). Although the scatter is quite large, the ellipse of the observed Q vs U data points appears to be quite eccentric. This is most exactly reproduced with case A, implying that the free electron density in the plane is indeed asymmetric. On the other hand, in the case B produced Q vs U ellipses, at 18° it is hardly even eccentric and, even worse, at 67° the ellipse appears to be tilted the wrong way. Still, perhaps the scatter is intrinsic to the WR-star (not related to the binary motion) and coincidently the few trailed-off points take the shape of an ellipse. If this is the case then the circular fit at 18° may very well best describe the variations of the Stokes' parameters in the $Q-U$ plane.

Regardless of the most likely case, estimation of the confidence intervals for inclinations determined polarimetrically is imperative. According to Wolinski & Dolan (1994) a quantifiable measure of the data's quality is given by the factor

$$\gamma = \left(\frac{A}{\sigma}\right)^2 \frac{N}{2}, \tag{2.7}$$

where N is the number of observations, σ is the mean error and A is the amplitude of the polarimetric variability defined by

$$A = \frac{|Q_{\max} - Q_{\min}| + |U_{\max} - U_{\min}|}{4}. \tag{2.8}$$

Provided that the polarimetric data have 38 observations each with a standard deviation of $\sigma = 0.035\,\%$ and an amplitude of $A = 0.23\,\%$, we obtain a γ factor of $\simeq 750$. It is stated that the polarimetric bias towards higher angles decreases with increasing i and γ. In other words, one needs better polarimetric precision and/or many more observations to determine accurately lower inclination angles.

Referring to Wolinski & Dolan (1994)'s Fig. 1 indicates that even with a given precision of $\gamma = 1200$, if the true orbital inclination is 10°, one can then obtain a best-fitted polarimetric angle ranging from 30 to 60°. This window only widens as γ decreases as is the case for the WR 148 observations. A denser data set with an enhanced statistical precision is therefore needed to provide a significant constraint.

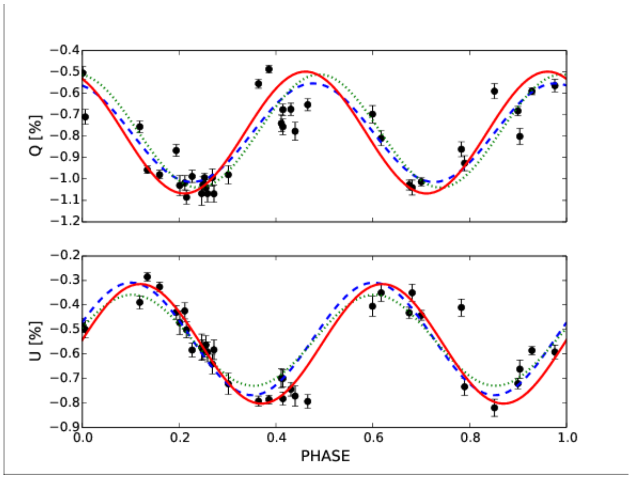

Figure 2.9: Stokes' parameters Q and U plotted as a function of orbital phase. The red solid curve represents the fit at 69.4° (case A), the blue dashed curve at 18° (case Ba) and the green dotted curve at 67° (case Bb). The polarimetric observations are provided from Drissen et al. (1986).

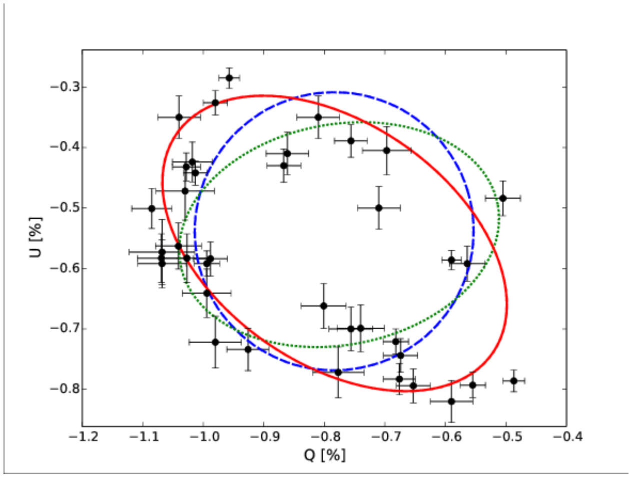

Figure 2.10: Polarimetric variations plotted in the $Q-U$ plane. The red solid curve represents the fit at 69.4° (case A), the blue dashed curve at 18° (case Ba) and the green dotted curve at 67° (case Bb). Overplotted is a typical single-point 2σ error bar.

2.3.5 Revisiting the photometry

In Marchenko et al. (1996), a compilation of light curves was fitted using a modified version of the Lamontagne et al. (1996) atmospheric eclipse model. The original proposed model (which we use here) is a geometrical paradigm to characterize the phase-dependent scattered light of the O-star as it passes through the WR wind. It assumes a spherically symmetric WR wind and a negligible O-star wind where Thomson scattering by the free electrons in the WR wind is the dominant process. We will assume that the WR wind obeys a velocity expansion law with $\beta = 1$ which is probably not unusual for a large, O-like WNLh star. Under these circumstances, Lamontagne et al. (1996) derived the following analytical expression for the light curve:

$$\begin{split}\Delta m = \Delta m_0 + \mathscr{A} \left[\frac{2}{\sqrt{(1-\varepsilon^2)(1-b^2)}} \left[\arctan\left(\frac{1+b}{1-b} \right) + \right.\right. \\ \left.\left. \arctan\left(\frac{1+b}{1-b} \tan\left(\frac{\arcsin\varepsilon}{2} \right) \right) \right] \right],\end{split} \tag{2.9}$$

where Δm_0 is a constant, $\varepsilon = \sin i \cos 2\pi\phi$ and $\mathscr{A}$ is the amplitude defined by

$$\mathscr{A} = \frac{(2.5 \log \mathrm{e})k}{(1 + I_{WR}/I_O)}, \tag{2.10}$$

k and b are given by

$$k = \frac{\alpha \sigma_t \dot{M}}{4\pi m_p v_{WR}^{\infty} a}, \tag{2.11}$$

$$b = \frac{R_\star/a}{\sqrt{1-\varepsilon^2}}, \tag{2.12}$$

where σ_t is the free electron Thomson cross section, m_p is the proton mass, v_{WR}^{∞} is the terminal velocity of the WR-star, a is the orbital separation, I_{WR}/I_O is the WR- to O-star light ratio at the observed wavelength, $\dot{M}$ is the WR mass-loss rate, α is the number of free electron per baryon and $R_\star$ is the WR-star core radius. Obtaining the best-fitted $\mathscr{A}$ parameter holds the potential of determining other fundamental parameters, although coupled, such as the light ratio or the mass-loss rate.

Fitting equation 2.9 to the observations requires an $R_\star/a$ ratio. The separation, $a =$

$7.5(1+1/q)/\sin i \;\; R_{\odot}$, varies from $17-46\, R_{\odot}$ for $i = 67^{\circ}$ to 18°, respectively. The photospheric radius is albeit more ambiguous to determine. For massive H-rich WRs, $R_{\star}$ can range anywhere from 10 to 25 $R_{\odot}$ (Hamann et al., 2006b). To avoid scenarios where the photospheric radius is larger than the separation, we will assume a constant fraction of $R_{\star}/a = 0.5$. In any case, the final result does not depend sensitively on the ratio.

Presented in Fig. 2.11 is the phased light curve provided from all previous photometric observations in the V band: Bracher (1979), Antokhin (1984), Moffat & Shara (1986) and Marchenko et al. (1996). Despite the large scatter (which is mostly intrinsic and likely due to inhomogeneities in the WR wind), we notice a dip at 0.0 phase. This arises as the O-star passes behind the WR and more of its light is Thomsom scattered out of the line of sight. Biased by the presumed orbital inclination of 67°, Marchenko et al. (1996) fixed i to this value and fit the phased light curves to a modified version of equation 2.9 with as free parameters the amplitude, $\mathscr{A}$, and zero point, Δm_0, along with enhanced ionization effects from the companion. Here we apply the orignal atmospheric eclipse model from Lamontagne et al. (1996) so we ignore the companion's extended light source. Ideally, though, the inclination angle should be left as a free parameter. However, with all three parameters left free in the Lamontagne et al. (1996) atmospheric eclipse model, the fits were unsatisfactory as the errors of the fitted paramers were larger than the values themselves. This is due to the degeneracy between $\mathscr{A}$ and i in equation 2.9 at very low inclinations.

Similar treatment to the polarization was therefore used: ranging i from 0° to 90° and fitting the phased light curves. At increments of 5°, the reduced χ^2 was also computed. We find that the observational data fit best with the model at low inclinations, similar to the polarization. Indeed, Fig. 2.12 shows a decrease in the reduced χ^2 towards smaller inclination. However, no global minimum is achieved. Again, there is no convergence in the reduced χ^2 to 1.0, probably for the same reasons as the polarimetry, i.e. due to clumping of the WR wind.

For comparison's sake, two synthetic light curves, obtained while fixing the orbital inclination at 18° and 67°, are shown in Fig. 2.11. The fitted parameters are indicated in

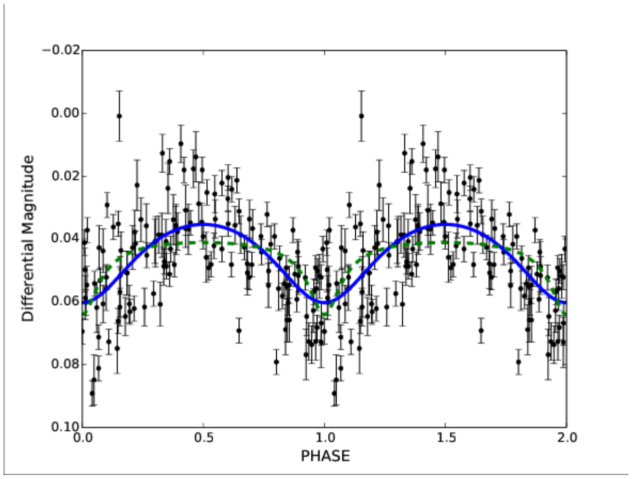

Figure 2.11: Phased light curve. Photometric observations are provided from Bracher (1979), Antokhin (1984), Moffat & Shara (1986) and Marchenko et al. (1996). The blue solid curve represents the fit at 18° and the green dashed at 67°. 2σ error bars are overplotted.

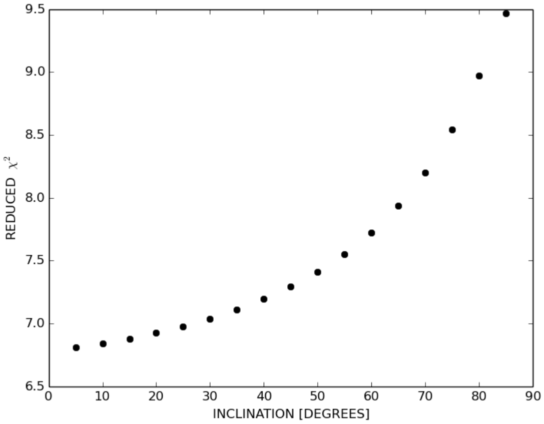

Figure 2.12: Reduced χ^2 as a function of orbital inclination for the photometric model

Table 2.VII. In agreement with the polarimetric results, the atmospheric eclipse model coincides best with the observations at lower inclinations. We will henceforth reject the previous 67° polarimetric inclination and only consider the newly derived 18° inclination.

2.3.6 Colliding Winds

Like in most massive binaries, where both stars have substantial stellar winds, we expect to see evidence of colliding winds (CWs). The shock region where the winds collide can produce considerable X-ray emission. Similarly, this phenomenon is often manifested as extra line emission in some spectral lines. Thermal X-rays have already been found in WR 148 from Zhekov (2012)'s analysis of XMM-Newton observations. Here we explore the excess line emission arising from the wind-wind collision zone.

Of particular interest are the line-profile variations of He II λ4686 because this line is highly sensitive and susceptible to CW (e.g. Marchenko et al., 1997). In order to extract the excess emission of He II λ4686, we first need to construct an underlying template of this line, which is then subtracted from each single spectrum in the WR frame and then returned to the observer's frame. Any residual flux is then considered to be excess emission, assuming the underlying profile is constant around the orbit. The base profile is obtained by taking the minimum flux across the line profile, shifted to the WR frame at each pixel (see Fig. 2.13).

The excess emission occurs from the shock-heated material viewed at different angles as the O-star orbits the WR-star. Fig. 2.14 demonstrates this phase-dependent behaviour of the extra emission. Luehrs (1997) first attempted to model these periodic modulations based upon the geometry of the wind-wind collision zone. This was further

Table 2.VII: Best-fitting values for the Lamontagne et al. (1996) atmospheric eclipse model

Parameter	$i = 18°$	$i = 67°$
Δm_0 [mag]	0.477 ± 0.006	0.649 ± 0.006
$\mathscr{A}$	0.017 ± 0.002	0.0030 ± 0.0005

developed by Hill et al. (2002). Adopting the formalism from Hill et al. (2002), the radial velocity of this excess emission ($\mathrm{RV}_{\mathrm{ex}}$) and full width ($FW_{\mathrm{ex}}$) can be characterized by

$$\begin{aligned} \mathrm{RV}_{\mathrm{ex}} &= c_2 + v_{\mathrm{strm}} \cos\theta \sin i \cos 2\pi(\phi - \delta\phi), \\ \mathrm{FW}_{\mathrm{ex}} &= c_1 + 2v_{\mathrm{strm}} \sin\theta \sqrt{1 - \sin i^2 [\cos 2\pi(\phi - \delta\phi)]^2}, \end{aligned} \tag{2.13}$$

where c_1 and c_2 are constants, θ is the the half-opening angle of the cone, v_{strm} is the streaming velocity of the excess-emitting material in the shock cone and $\delta\phi$ is the aberration angle owing to the orbital motion relative to the wind speed. Combining the OMM and Keck data to improve the phase coverage, we measure $\mathrm{FW}_{\mathrm{ex}}$ at one third maximum and $\mathrm{RV}_{\mathrm{ex}}$ from the centroid of the line at this height. Equations 2.13 are fitted simultaneously to the observations while fixing the inclination angle at 18°. The results from the fitting procedures are presented in Table 2.VIII and shown in Fig. 2.15. We note that the aberration angle is effectively zero, which further supports the case B polarimetry scenario (see 2.3.4).

On one hand, using the Usov & Melrose (1995) formula we can deduce the wind momentum ratio, η, from only the value of the half opening angle, θ:

$$\theta(\mathrm{rad}) \simeq 2.1 \left(1 - \frac{\eta^{2/5}}{4}\right) \eta^{1/3}, \tag{2.14}$$

for $10^{-4} \leq \eta \leq 1$, with

$$\eta \equiv \frac{\dot{M}_O v_O^\infty}{\dot{M}_{WR} v_{WR}^\infty}, \tag{2.15}$$

where v_O^∞ and v_{WR}^∞ are, respectively, the terminal velocities of the O- and WR-stars. With a half opening-angle of $\theta = 78.6 \pm 4.0°$, we find a rather large momentum ratio of $\eta = 0.51 \pm 0.13$. We take note of a smiliar short period WR+O system with a rather high momentum ratio as well: V444 Cygni. Indeed, V444 Cygni is a well studied WN5+O6 colliding-wind binary system ($P = 4.212$ d) where $\eta \sim 0.13$ is deduced from $\theta = 50° - 60°$ (Marchenko et al., 1994). This is comparatively high in contrast to the generally obtained values of $\eta < 0.05$ from other WR+O colliding wind binaries (e.g. Fahed & Moffat, 2012; Hill et al., 2000). On the other hand, defined by equation 2.15,

η can also be determined using the typical mass-loss rates and terminal velocity values associated with each star's spectral type.

The WR's mass loss rate can be estimated polarimetricaly using equation 6 from St.-Louis et al. (1988):

$$\dot{M}(M_{\odot}\,\mathrm{yr}^{-1}) = \frac{2.33\times 10^{-7} A_p a(R_{\odot}) v^{\infty}_{\mathrm{WR}}(\mathrm{km\ s}^{-1})}{(1+\cos^2 i) f_c I}, \tag{2.16}$$

where f_c is the fraction of the total light in the filter used coming from the companion O star, I is a dimensionless integral defined in St.-Louis et al. (1988) and A_p is the semi-major axis of the ellipse in the $Q-U$ plane, which can otherwise be written as

$$A_p = H(1+\cos^2 i). \tag{2.17}$$

Given the spectral types of each star, f_c is obtained from

$$f_c = \frac{I_O}{I_{WR}+I_O} = \left(1+10^{-0.4\Delta M_v}\right)^{-1}, \tag{2.18}$$

where $\Delta M_v = M_v(WR) - M_v(O)$ is the difference between the respective absolute visual magnitudes of the WR- and the O-star. Taking $M_v(WR) = -7.0$, the mean value between -6.8 (Crowther, 2007) and -7.2 (Hamann et al., 2006b), and $M_v(O) = -5.21$ (Martins et al., 2005a) yields $f_c = 0.16 \pm 0.04$ and likewise, $I_{WR}/I_O = 5.2 \pm 1.0$. Finally, taking $v^{\infty}_{\mathrm{WR}} = 2000\,\mathrm{km\,s}^{-1}$ (this paper from inspecting low resolution IUE spectra) and I=18.6 (computed numerically with $\beta = 1$, $R_{\star}/a = 0.5$ and $\varepsilon = 1$, as defined in St.-Louis et al. (1988)) we obtain a polarimetric mass-loss rate of $\log \dot{M}_{\mathrm{pol}}(\ M_{\odot}\, yr^{-1}\ )$ =-5.2 ±0.3.

Alternatively, an estimate of the WR's mass-loss rate can be derived photometrically via equations 2.10 and 2.11. Using $\alpha = 0.5$ (for a wind dominated by He^{++}), $I_{WR}/I_O = 5.2$, $v^{\infty}_{WR} = 2000\,\mathrm{km\,s}^{-1}$ and the best-fitted amplitude, $\mathscr{A}$, from Table 2.VII, we find a photometric mass-loss rate an order of magnitude larger with $\log \dot{M}_{\mathrm{phot}}(\ M_{\odot}\, yr^{-1}\ )$ =-4.3 ±0.3 (see Table 2.IX).

Many factors can contribute to the discrepancy between the photometric and polarimetric mass-loss rates. First, we point out that the photometric mass-loss rates are far

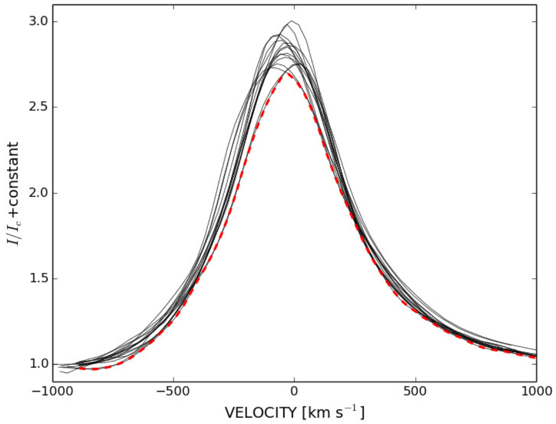

Figure 2.13: Line profiles of He II λ4686 shifted to the WR frame. The red dotted curve denotes the synthetic unperturbed base profile.

Table 2.VIII: Best-Fitting values for the colliding wind model (Hill et al., 2002)

Parameter	$i = 18^\circ$
c_1 [km s^{-1}]	-101 ± 22
c_2 [km s^{-1}]	-3827 ± 1400
$v_{\rm strm}$ [km s^{-1}]	2230 ± 700
θ [deg]	77.9 ± 4.8
$\delta\phi$ [deg]	0.0 ± 5.6

Table 2.IX: Mass loss rates obtained photometrically and polarimetrically

Parameter	$i = 18^\circ$
$\log \dot{M}_{\rm phot}$ [$M_\odot$ yr^{-1}]	-4.3 ± 0.3
$\log \dot{M}_{\rm pol}$ [$M_\odot$ yr^{-1}]	-5.2 ± 0.3

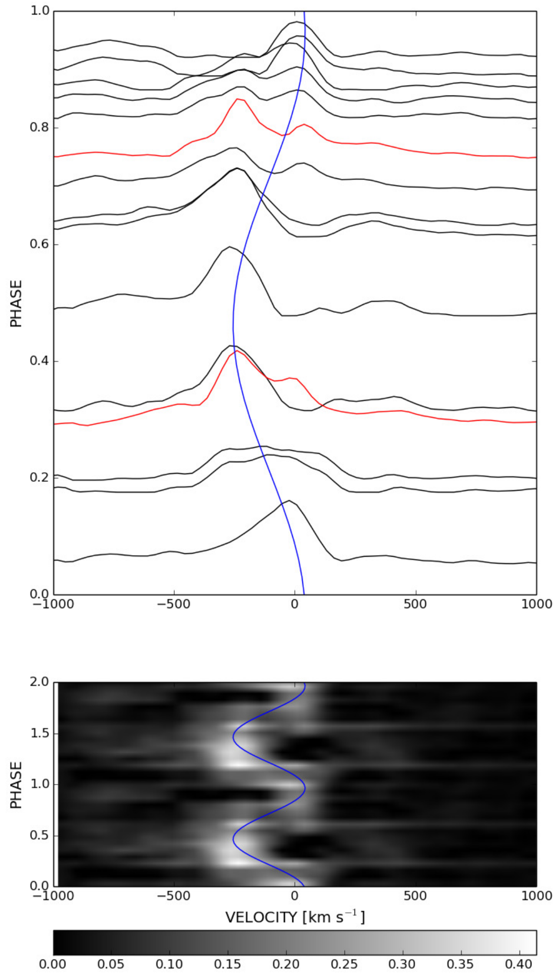

Figure 2.14: Excess emission in He II λ4686 varying with phase along the *x* axis. The red profiles are from the Keck data and the others from OMM. The blue curves represent the CW fit to the excess emission with parameters listed in Table 2.VIII.

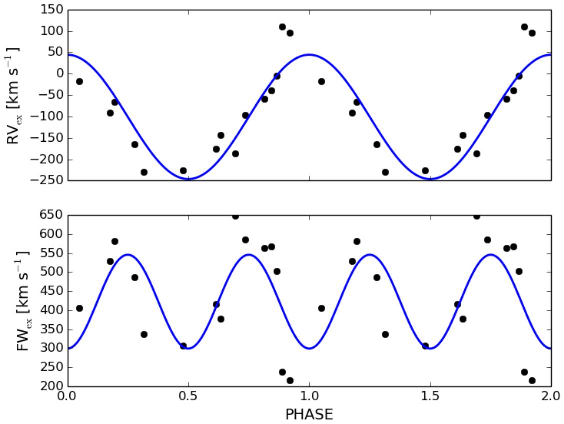

Figure 2.15: RV$_{\rm ex}$ and FWHM$_{\rm ex}$ plotted as a function of orbital phase. The blue solid curve represents the fit at 18°.

more sensitive to changes in the inclination angle than the polarimetric values. In fact, increasing the inclination slightly, from 18° to 20°, decreases $\log\dot{M}_{\rm phot}(M_{\odot} yr^{-1})to$-4.5 ±0.3, whereas $\dot{M}_{\rm pol}$ remains constant. Second, both the polarimetric and photometric mass-loss rates depend on the chosen β for the velocity law and the $R_{\star}/a$ ratio. Even though we have fixed them to their most likely values ($\beta = 1$ and $R_{\star}/a = 0.5$), varying them within their uncertainty boundaries can lead to a whole order of magnitude difference on $\dot{M}$. Finally, some fundamental assumptions in the models themselves, such as a negligible O-star wind contribution, may not be entirely justified in this case, especially when the wind momentum fraction is rather large. The errors on the mass-loss rates, being computed via propagation of errors, are therefore most likely underestimated.

Due to the uncertainty on the WR's mass loss rate, rather than attempt to re-derive the wind momentum fraction using equation 2.15, we use the best fitted value for η from the CW model to further constrain $\dot{M}_{WR}$. Considering typical values for the terminal velocity and mass-loss rate for an O5V star, $v_O^{\infty} = 2900\,{\rm km\,s^{-1}}$ (Conti et al., 2008) and $\log\dot{M}_O(M_{\odot} yr^{-1})$=-5.9$(Contietal.,2008)$, yields $\log\dot{M}_{WR} = -5.4 \pm 0.3$ which is most compatible with the polarimetric mass loss rate.

Up to this point, we have not yet considered the influence of radiative braking. As the WR wind approaches the O-star, the increased O-star radiation can inhibit the WR wind, thus potentially increasing the half-opening angle of the wind-wind interaction cone. This phenomenon has been thoroughly studied by Gayley et al. (1997) and we follow their prescription to determine whether radiative braking has an effect in WR 148 or not. To do so, we first need to evaluate the following parameters: $\hat{d} = d/d_{rb}$ and $\hat{P} = 1/(\eta P_{rb})$ where d_{rb} is the solution of

$$d_{rb} = 1 + \left(\frac{d_{rb}}{\gamma}\right)^{(1-\alpha)/(1+\alpha)}, \tag{2.19}$$

$$P_{rb} = \frac{4\beta^{\beta} d_{rb}^{2}}{(2+\beta)^{2+\beta}}, \tag{2.20}$$

and

$$\gamma = \frac{4}{3}\left(\frac{L_O}{L_{WR}}\right)^2 \frac{2GM_{WR}}{(v_{WR}^{\infty})^2 R_O}, \tag{2.21}$$

where L_O and L_{WR} are, respectively, the luminosities of the O- and the WR-star, R_O is the O-star's radius, $d = a/R_O$, $\alpha = 0.5$ is the CAK line-distribution exponent, $\beta = 1$ is the velocity law index and G is the Gravitational constant. Radiative braking becomes important if $\hat{d} > 1$ and $\hat{P} > \hat{d}^2$. Using $\log L_O(L_\odot) = 5.21$ and $R_O = 11\,R_\odot$, appropriate for an O5V star (Martins et al., 2005a) and $\log L_{WR}(L_\odot) = 6.2$ (Hamann et al., 2006b), we find $\hat{d} = 0.24$ and $\hat{P} = 0.04$. Radiative braking therefore appears to be insignificant in this case.

2.3.7 Runaway status

Runaways are stars with abnormally high peculiar space velocities, typically above $30\,\mathrm{km\,s^{-1}}$ for massive stars (Dray et al., 2005). As a result, they can be found high above the Galactic plane if the star is ejected in an appropriate direction. Two scenarios are generally accepted for producing massive-star runaways:

1. Binary ejection scenario (BES) : In a binary system, a supernova explosion (SN) may disrupt the system and eject the optical component. Surviving bound systems, though rare, also receive a recoil (Blaauw, 1961).

2. Dynamical ejection scenario (DES) : In dense forming open clusters, runaways arise from close gravitational encounters between stars (Poveda et al., 1967).

An alternative theory is expulsion of the binary component in a hierarchical triple system upon the SN explosion of the tertiary.

WR 148's runaways status was highly suspected since Moffat & Seggewiss (1979). However, little is known on its ejection mechanism. Since the companion for WR 148 is now confirmed to be non-compact, the BES hypothesis is no longer a viable option, leaving dynamical or tertiary ejection mechanisms as the only possible scenarios. We will explore all three scenarios mentioned above.

Taking the Hipparcos proper motions, the spectroscopic radial velocity and estimated distance[2] (see Table 2.X), we recreate WR 148's space velocity and retrace its trajectory back in time. This was done in an attempt to determine its origin. As done in Hoogerwerf et al. (2001), the orbits are integrated numerically with a fourth-order Runge-Kutta method in a Galactic potential described with a three component model: a logarithmic potential for the halo and a Miyamoto-Nagai potential for the disk and bulge of the Galaxy with parameters recently refined by Irrgang et al. (2013). Prior to the orbit integration, the star's heliocentric velocity, $v_\star$, must be corrected for the velocity of the Sun relative to the local standard of rest (LSR), $v_\odot$, and for the rotational velocity of the LSR relative to the Galactic center, $v_{\rm LSR}$. In the Galactic barycentric frame, $v_\star$ will thus be converted to

$$v_{\rm gal} = v_\star + v_\odot + v_{\rm LSR}, \tag{2.22}$$

where $v_\odot = (10.00, 5.23, 7.17)\,\mathrm{km\,s^{-1}}$ (Dehnen & Binney, 1998) and $v_{\rm LSR} = (0.0, 220.0, 0.0)\,\mathrm{km\,s^{-1}}$ (Binney & Tremaine, 1987). Because of the large errors on the proper motions and distance, we conducted 1000 Monte Carlo simulations to scope the parameter error space. We obtained an average travel time (from its current location back to the Galactic plane) of 4.7±0.8 Myr, an averaged peculiar velocity of 197±30 $\mathrm{km\,s^{-1}}$ at its

---

[2] Galactic WR stars have been newly calibrated based on revised near-infrared absolute magnitudes in Rosslowe & Crowther (2015). Since WR 148's distance is more sensitive to the WR-star's absolute visual magnitude uncertainty than on the contribution of the O-star companion, we adopt the distance estimate from Rosslowe & Crowther (2015).

curent location and an averaged peculiar velocity of 198±27 km s^{-1} at its past location leaving the plane. The errors given here are statistical 1σ errorbars. Though less likely, results in the $2-3\sigma$ range are conceivable.

The trajectory time is close to the upper limit of the lifetimes of massive WR-stars. However, it is certainly in the realm of possibility especially within the 2σ level. During this ballistic trajectory, we find that WR 148's peculiar velocity remains roughly constant. Moffat et al. (1998) also computed the peculiar tangential velocity (in direction of Galactic longitude and latitude) for several WR and O star runaways using the Hipparcos proper motions. Taking into account the peculiar radial velocity, we confirm that their obtained tangential peculiar velocity of 194 ± 110km s^{-1} for WR 148, is consistent with our result. Also, we note that this velocity is very similar to the high observed peculiar velocity of the WN8h runaway WR 124, close to 200 km s^{-1} (Moffat et al., 1982).

If WR 148 was ejected via a DES, we should be able to retrace its steps back to its parent OB association. However, this test was inconclusive because not only is the uncertainty on the system's spatial parameters high, but the localizations of the known OB associations (Mel'Nik & Dambis, 2009) are mostly limited to the solar neighborhood and are not so well known near the vicinity where the ejection starting point lies in the Galactic plane.

Though DES runaways favour single runaways, there is still a non negligible binary fraction. According to the N-body simulations (four-body encounters) performed by Leonard & Duncan (1990b), 10 % of the ejected runaways are predicted to be binaries. These binaries typically have high mass ratios above 0.5 and eccentricities between 0.4 and 0.7, although it is mentioned that for short period binaries, the eccentricity can decrease rapidly due to tidal circularisation. These properties are all found in WR 148. An extensive study of N-body simulations in massive clusters (three body scatterings) was followed up by Perets & Šubr (2012). They concluded that dynamically ejected binaries become increasingly rare at higher ejection velocities and essentially no binaries are expected to be ejected with velocities above 150 km s^{-1} . With a peculiar space velocity of $\sim 198 \pm 27$ km s^{-1} , WR 148 is definitely a unique case among the fastest massive runaway stars. Within the 2σ range, WR 148's peculiar space velocity is just achievable with the maximum predicted velocity for DES runaways.

Perhaps the system was expulsed by means of the proposed tertiary method. To evaluate the likelihood of this scenario we first need to determine the geometry of a hierarchical triple system. This configuration remains stable if the separation of the outer binary is significantly wider than the inner binary's separation (Michaely & Perets, 2014). This translates to,

$$\alpha = \frac{a_2}{a_1} \ll 1, \tag{2.23}$$

where a_1 and a_2 are respectively the semi-major axes of the outer and inner orbit, regardless of their eccentricities. Determining α analytically can only be done in special cases (see Naoz et al., 2013). Therefore, obtaining a stricter stability criterion is beyond the scope of this paper. In the following, we will assume that $\alpha = 0.1$ will suffice to ensure stability.

If the SN explosion of the tertiary decouples the outer orbit, the inner system will be ejected with its orbital velocity

$$K_{1,2} = \frac{m_3}{m_1 + m_2 + m_3} v_{\mathrm{orb}}, \tag{2.24}$$

with

$$v_{\mathrm{orb}} = \sqrt{\frac{G(m_1 + m_2 + m_3)}{a_1}}, \tag{2.25}$$

where v_{orb} is the outer systems orbital velocity, m_3 is the mass of the tertiary and $m_1 + m_2$ is the mass of the inner orbit. Solving equation 2.24 for m_3 yields

$$m_3 = \frac{\kappa + \sqrt{\kappa^2 - 4\kappa(m_1 + m_2)}}{2} \tag{2.26}$$

where $\kappa = \frac{K_{1,2}^2 a_1}{G}$. This allows us to estimate the tertiary's required mass to eject the inner binary with WR 148's observed peculiar velocity.

The parameters in equation 2.26 need to be known at the moment of WR 148's ejection. We know that the system's present orbital separation is $\sim 46\,R_\odot$. Considering a WR mass loss rate of $10^{-5.3}\,M_\odot\,\mathrm{yr}^{-1}$ and a WR phase lifetime of ~ 0.5 Myr [corresponding to $\sim 10\%$ of its descendent O-star lifetime (Meynet & Maeder, 2003) assumed to be equivalent to its travel time, i.e. ~ 5 Myr] we estimate that the WR-star lost approximately $2.5 M_{\odot}$. Whether this mass loss had been transferred to the companion or not shouldn't significantly alter the binary's configuration. In that case, a system with WR 148's present configuration to be ejected with an initial peculiar of 198 $\mathrm{km\,s^{-1}}$ would require a tertiary mass of $137 M_{\odot}$. Though high, it is feasible. This scenario would expect WR component to have had an initial mass of $\sim 35 M_{\odot}$. However, hydrogen righ WR-stars such as WR 148 are suspected to evolve from massive $65-110 M_{\odot}$ O-stars (Maeder & Meynet, 1994). To account for this discrepancy in initial mass, perhaps a formation of a common envelope (CE) caused the system to spiral in and eject its CE. This could expain WR 148's short orbital period. If this is the case, deriving an initial configuration for WR 148 is subject to too many uncertainties. Though, as ejection through hierarchical triple systems are rather inefficient at producing high-velocity runaway binaries (because the large separation needed for stability would require unrealistically large tertiary mass), we consider the tertiary mechanism to be an unlikely ejection mechanism for WR 148.

Another point to consider is the typical timescales of dynamical or tertiary ejections to occur. DES runaways are effectively ejected very near to the zero-age main sequence, whereas the latter ejections are delayed due to the longevity of the tertiary, which could take a few million years depending on its mass. Since the lifetime of the massive WR is already border-line compared to its travel time, it could not afford to wait another 1 or 2 Myr to be ejected. In short, it is unlikely that WR 148 was ejected from the tertiary mechanism and the DES method is prefered.

Looking further, WR 148 is a prime example of studying the occurence of a double ejection scenario: a DES to explain the current system followed by a future BES. As the WR component evolves and undergoes a SN explosion, the system may disrupt, possibly providing a supplementary kick. This may give rise to either two single runaways, if the system disrupts, or a binary runaway, if the system remains bound. Given the modeled Galactic potential, the escape velocity at WR 148's current location is estimated to be ~ 548 $\mathrm{km\,s^{-1}}$. With a space velocity of 281 $\mathrm{km\,s^{-1}}$ and an orbital velocity of

$v_1 = K_1/\sin i \sim 285 \pm 31$ km/s and $v_2 = K_2 \sin i \sim 256 \pm 28\,\mathrm{km\,s^{-1}}$, the gravitational decoupling of the system may eject one or both components to break free from the Galactic gravitational potential.

2.3.8 Rotation

It is instructive to constrain the projected rotation velocity $v \sin i$ of the companions, which can yield vital information regarding binary interaction in the system, e.g. synchronization and spin-up due to mass transfer. For this purpose, we calculate synthetic spectra for the WR- and O-companions using the Potsdam Wolf-Rayet (PoWR) model atmosphere code (see Gräfener et al. 2002 and Hamann & Gräfener 2004 for more details). The O-star model is calculated with parameters corresponding to an O5 dwarf based on Martins et al. (2005b). The WR model is calculated with parameters adopted from Hamann et al. (2006c), although some adjustments were made to provide a better fit to the specific features which are used here to constrain $v \sin i$.

To simulate the effect of rotation on the spectrum of the O component, we convolve the synthetic O-star spectrum with a rotation profile (virtually an ellipse, Gray 1975). However, additional broadening that is entangled with the rotation should also be included before $v \sin i$ can be derived. These include microturbulence, macroturbulence, and pressure broadening. Pressure broadening is intrinsically accounted for by the PoWR code. The photospheric microturbulence ξ_{ph} is set to the typical value of $20\,\mathrm{km\,s^{-1}}$ (e.g. Markova & Puls, 2008; Shenar et al., 2015) and is included in the calcu-

Table 2.X: WR 148 spatial parameters

Parameters	Values	Reference
l [deg]	90.0810	[1]
b [deg]	+06.4694	[1]
$\mu_\alpha \cos\delta$ [mas yr^{-1}]	-7.63 ± 1.39	[1]
μ_δ [mas yr^{-1}]	-1.78 ± 1.13	[1]
d [kpc]	7.05 ± 1.16	[2]
v_r [$\mathrm{km\,s^{-1}}$]	-120.1 ± 2.3	[3]

[1]van Leeuwen (2007), [2]Rosslowe & Crowther (2015), [3] this paper

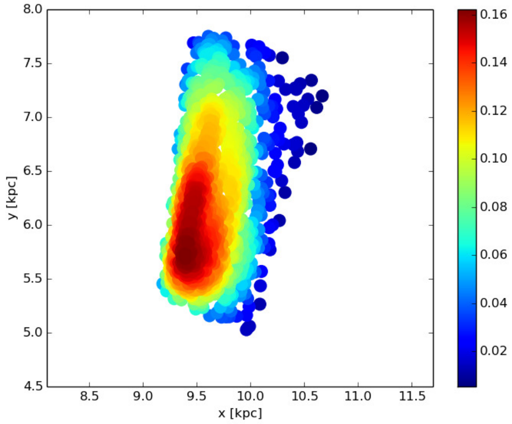

Figure 2.16: Probability distribution of the possible launching sites of WR 148 back in the Galactic plane. The x and y axis are both centered on the Galactic centre with the x axis passing through the Sun located at $R_0 \simeq 8.5$kpc perpendicular to the y axis.

lation of the synthetic spectrum. Finally, the macroturbulence $v_{\rm mac}$, which is typically found to be of the order of 20-90 km s^{-1} (e.g. Bouret et al., 2012), is treated as a free parameter, and is accounted for by convolving the synthetic spectrum with a corresponding radial-tangential profile (Gray, 1975).

We use the isolated O III $\lambda 5592$ line to determine $v \sin i$ and $v_{\rm mac}$ via a 2D χ^2 minimization algorithm, with $0 \leq v_{\rm mac} \leq 90\,{\rm km\,s^{-1}}$. We obtain $v \sin i = 60^{+20}_{-10}\,{\rm km\,s^{-1}}$ and $v_{\rm mac} = 80^{+10}_{-30}\,{\rm km\,s^{-1}}$ for the O component. In Fig. 2.17, we compare the composite WR + O synthetic spectrum to the 2014 Keck observations, accounting for the secondary's rotation and turbulence. The synthetic O spectrum was convolved with the determined $v \sin i$ and $v_{\rm mac}$ values. To confirm our results, we also perform an independent analysis of the O III feature using the IACOB-BROAD tool, which solves for $v \sin i$ in Fourier space (Simón-Díaz & Herrero, 2014), and find $v \sin i = 70\,{\rm km\,s^{-1}}$. Hence, both methods agree within the errors.

WR-stars are notoriously known for lacking pure photospheric features, making it difficult to measure their rotation directly. However, careful examination of the Keck spectra revealed a feature which clearly originates in the WR-star and is almost purely photospheric, namely, the N IV $\lambda\lambda 5200, 5204$ doublet. The observation, shown as a blue solid line in Fig. 2.18, shows relatively narrow absorption lines which follow the orbital motion of the WR component. The model calculated for the WR-star confirms that these lines are almost purely photospheric. This means that the observation provides us access to the poorly-understood photosphere at the base of the wind of a WR-star, which is indeed a rare occasion.

However, determining $v \sin i$ for the WR component is significantly more complex than for the O-star component. Firstly, the photospheric microturbulence of late-type WR-stars was poorly studied empirically, let alone their macroturbulence. Secondly, due to the extended WR photospheres, rotation cannot be treated via convolution, but rather a 3D integration algorithm of the intensities is necessary (Shenar et al., 2014a). Because the problem is significantly more complex, here we only give a rough estimate for the possible rotation of the WR component. A thorough and detailed study of the photospheres of this and other late-type WR-stars will be given elsewhere (Shenar et al. in prep.).

For simplicity, $v_{\mathrm{mac}} = 0\,\mathrm{km\,s^{-1}}$ is assumed. Then, assuming $\xi_{\mathrm{ph}} = 30\,\mathrm{km\,s^{-1}}$, we find $v \sin i \sim 150\,\mathrm{km\,s^{-1}}$, although the fit quality is rather poor. Assuming on the other extreme that $\xi_{\mathrm{ph}} = 100\,\mathrm{km\,s^{-1}}$, we can only give an upper limit of $v \sin i 150\,\mathrm{km\,s^{-1}}$. Fig. 2.18 illustrates this: The observations (blue solid line) of the N IV doublet are compared to the synthetic WR spectrum calculated with $\xi_{\mathrm{ph}} = 30$ (left panel) and $100\,\mathrm{km\,s^{-1}}$ (right panel) and with different rotation velocities, as given in the legend. Indeed, this simple analysis implies that large turbulence velocities are present already in the photospheres

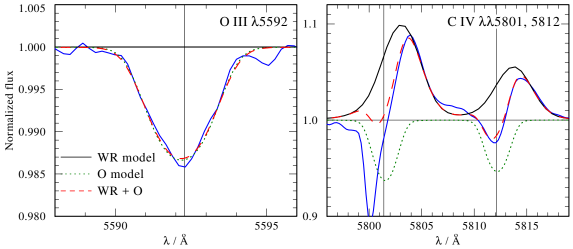

Figure 2.17: A comparison between the observed spectrum of WR 148 (blue solid line) and the modeled composite spectrum (red dashed line) of the O III $\lambda 5592$ line (left panel) and the C IV doublet (right panel). The individual synthetic components are shown in a black solid line for the WR-star and green dotted line for the O-star.

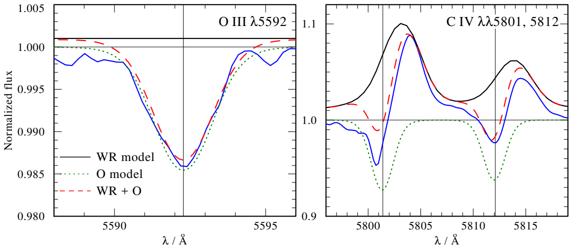

Figure 2.18: A comparison between the observed spectrum of WR 148 (blue solid line) and three synthetic WR spectrum, assuming $v \sin i = 0$ (black solid line), $v \sin i = 100$ (dashed red line) and $v \sin i = 200$ (dashed red line) of the N IV $\lambda\lambda 5200, 5204$ doublet for $\xi_{\rm ph} = 30\,{\rm km\,s^{-1}}$ (left panel) and $\xi_{\rm ph} = 100\,{\rm km\,s^{-1}}$ (right panel). The strong absorption feature at ~ 5800 Åis a residual DIB contamination after attempting to remove the DIB in section 2.3.1.

of WR-stars.

To summarize, we find $v \sin i = 60^{+20}_{-10}{\rm km\,s^{-1}}$ for the O component and $v \sin i 150\,{\rm km\,s^{-1}}$ for the WR component. Assuming that the rotation axes are aligned with the orbital axis and that $i = 18^\circ$, this yields $v_{\rm eq} = 194\,{\rm km\,s^{-1}}$ and $v_{\rm eq} 485\,{\rm km\,s^{-1}}$ for the equatorial velocities of the O and WR components, respectively.

The equatorial rotation velocity of the O-star is compatible with spin-up velocities attainable via mass in a Robe loche overflow process. In fact, the measured spin rates of the O-star component in WR+O binaries reveal that $v_{\rm eq}$ can range anywhere from 140 to 496${\rm km\,s^{-1}}$ (Shara et al., 2015). Or, the system may simply be synchronized. Adopting $R_{\rm O} = 11\,R_\odot$ for the O component as given by Martins et al. (2005b) for an O5V star, we find $P_{\rm rot,\,O} = 2.9^{+0.6}_{-0.8}\,{\rm d}$, which is smaller than the measured binary period of $P_{\rm orb} = 4.3173\,{\rm d}$. The WR rotation constraint does not help us further here. However, accounting for the uncertainties on the radius and inclination angle, we cannot forego the idea of synchronization. For instance, using $v \sin i = 50{\rm km\,s^{-1}}$, $R_{\rm O} = 12\,R_\odot$ and $i = 21^\circ$, we obtain $P = 4.35$ d. Thus, while the system has most definitely circularized, it may in fact be synchronized as well. Though, due to accumulated error propagation, we cannot confirm this with certainty.

2.4 Conclusions

We summarize our findings briefly as follows:

- WR 148 is found to be a normal, massive, close WR+O binary system: the primary is a H-burning WN7ha star and the secondary is an O5V star.
- This confirms the colliding wind binary scenario, rejecting once again the WR+cc scenario proposed in the past.
- Orbital solution is refined: P = 4.317336 d and time for phase zero (WR in front at inferior conjunction) of E = 2 444 825.04 HJD.
- We obtain a mass ratio of 1.1 ± 0.1. Assuming a mass of 37 $M_{\odot}$ for the O star, the WR component has a mass of 33 $M_{\odot}$ and the system has an orbital inclination of $18 \pm 4^{\circ}$.
- Regarding the previously determined inclination angle of 67°, we re-examine past polarimetric and photometric observations. Via a more appropriate error assessment, the polarimetric results are at best inconclusive requiring better data. The light curve is also now found to behave normally for an atmospheric eclipse of the O-star as it orbits in the WR wind favouring low inclinations.
- We deduce a O/WR wind momentum ratio of 0.51 ± 0.13 from analyzing the excess emission arising from CWs. Adopting typical mass loss rates and terminal velocities for an O5V star, we obtain for the WR component $\log \dot{M}(\ M_{\odot} yr^{-1}\ )$=-5.4±0.3. This is consistent with the mass loss rate derived from polarimetry.
- Most likely ejected via dynamical interactions, WR 148 is an extreme runaway with a current peculiar velocity of $\sim 197\,\mathrm{km\,s^{-1}}$.
- Runaway status is confirmed. WR 148 is currently $\sim 800\,\mathrm{pc}$ from the Galactic plane. It took $\sim 5\,\mathrm{Myr}$ to reach this position starting from the plane, which is marginally acceptable for massive-star lifetimes.

- The runaway's space velocity is not enough to allow for WR 148 to escape the Galactic potential; however, after the SN explosion of the current primary, two single massive runaways could result, with one or both able to escape the Galaxy.
- We find a projected rotational velocity of $v\sin i = 60^{+20}_{-10}\mathrm{km\,s^{-1}}$ for the O star and $v\sin i 150\,\mathrm{km\,s^{-1}}$ for the WR star. Adopting $\sin i$ from the orbit, leads to high rotation speeds for both stars. Though the system has definitely circularized, we cannot confirm whether it has synchronized.

Acknowledgements

AFJM and NSL are grateful for financial aid from NSERC (Canada) and FQRNT(Quebec). We acknowledge the help and support of colleagues at Université de Montréal, Universität Potsdam and W. M. Keck Observatory. NDR acknowledges postdoctoral support by the University of Toledo and by the Helen Luedtke Brooks Endowed Professorship. TR acknowledges support from the Canadian Space Agency grant FAST.

The authors wish to recognize and acknowledge the very significant cultural role and reverence that the summit of Mauna Kea has always had within the indigenous Hawaiian community. We are most fortunate to have the opportunity to conduct observations from this mountain.

Appendix A. Mean Keck spectra of WR 148 at two orbital quadratures

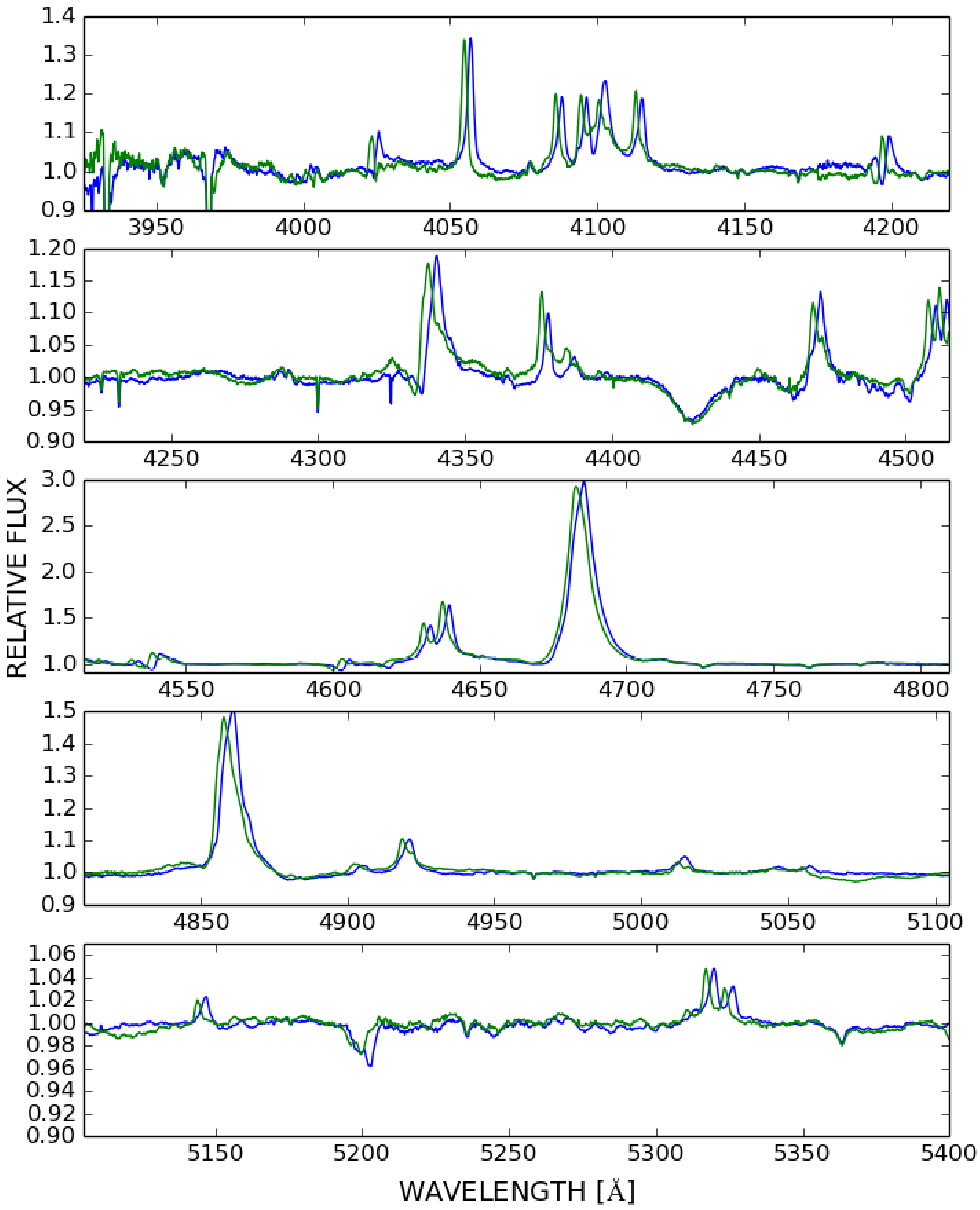

Figure 2.19: Mean spectra from the Keck observatory at both quadatures: phase $\simeq 0.279$ in blue and $\simeq 0.736$ in green.

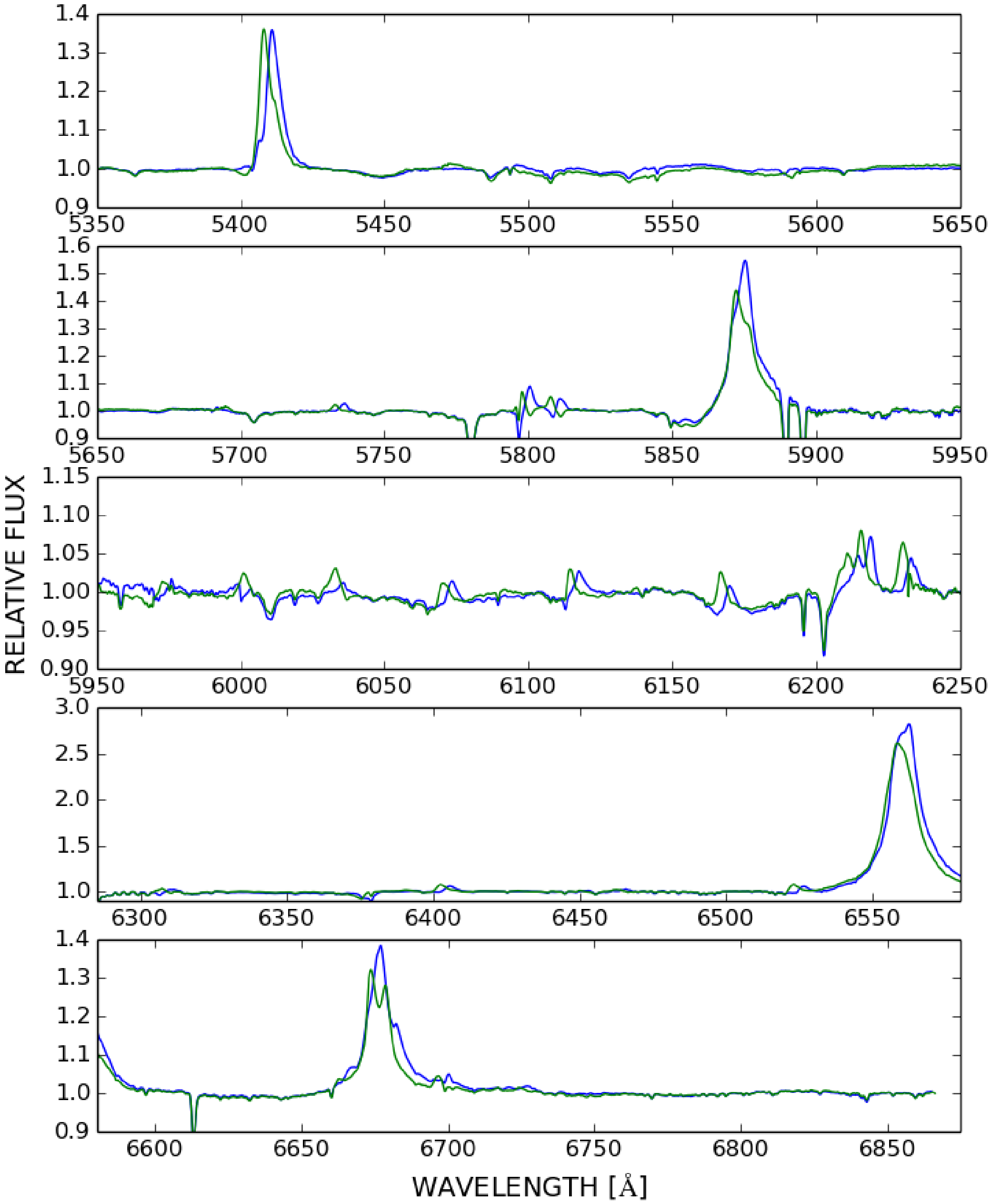

Figure 2.20: Continuation of Fig. 2.19

Fin de l’article.

CHAPTER 3

WR 71: L'ÉTOILE WOLF-RAYET SIMPLE EN CAVALE ETRÊME

L'article qui suit présente une étude photométrique et spectroscopique de WR 71. Il s'agit d'une étoile WR du type WN6o soupçonnée d'être comprise au sein d'un système binaire avec un compagnon compact. Les analyses photométriques et spectroscopiques de Isserstedt et al. (1983) révèlent une periode orbitale de 7.7 jours. Cependant, Balona et al. (1989) n'ont détecté qu'une période bruitée de 1.75 jours et aucune périodicité n'a été déterminée par Marchenko et al. (1998c). Ainsi, Hamann et al. (2006b) juge que les évidences de binarité ne sont pas suffisantes. Pour confirmer cette hypothèse, nous avons obtenu un mois de données photométriques continues à partir du télescope spatial MOST complémentées avec quelques données spectroscopiques à partir du sol.

Mes contributions correspondent à l'analyse des données photométriques et spectroscopiques, ainsi qu'à la reconstruction 3D des vitesses spatiales de WR 71. Les co-auteurs Bernard Heathcote, Terry Bohlsen et André-Nicholas Chéné ont obtenu et réduit les données spectroscopiques alors que Jason Rowe a réduit les données photométriques obtenues par l'équipe MOST. Guidé par Anthony Moffat, les co-auteurs Nicole St-Louis, Noel Richardon et Herbert Pablo ont tous fourni des commentaires constructifs et fondementaux à la rédaction de l'article. Enfin, l'article a été entièrement rédigé par moi-même.

L'article est en préparation et sa mise en forme a été adaptée pour être inclus dans le texte.

Muñoz, M., Moffat, A.F.J, Pablo, H., Rowe, J., Richardson, N.D., St-Louis, N., Chené, A.-N., Heathcote, B., Bohlsen, T., Matthews, J., Cameron, C., Guenther, D., Kuschnig, R., Weiss, Rucinski, S., Sasselov, D. (2016). The extreme-runaway single massive Wolf-Rayet star HD 143414 at 700 pc below the Galactic plane.
Monthly notices of the royal astronomical society
En préparation

The extreme-runaway single massive Wolf-Rayet star HD 143414 at 700 pc below the Galactic plane.

Melissa Muñoz,[1] Anthony F. J. Moffat,[1] Herbert Pablo,[1] Jason Rowe,[2] Noel D. Richardson,[3] Nicole St-Louis,[1] André-Nicolas Chené,[4] Bernard Heathcote,[5] Terry Bohlsen,[5] Jaymie Matthews,[6] Chris Cameron,[7] David Guenther,[8] Rainer Kuschnig,[9] Werner Weiss,[9] Slavek Rucinski,[10] Dimitar Sasselov[11]

[1]*Département de Physique, Université de Montréal, and Centre de Recherche en Astrophysique du Quebec, CP 6128, Succursale A, Montréal, QC H3C 3J7, Canada*

[2]*Institut de recherche sur les exoplanètes, iREx, Département de physique, Université de Montréal, Montréal, QC, H3C 3J7, Canada*

[3]*Ritter Observatory, Department of Physics and Astronomy, The University of Toledo, Toledo, OH 43606-3390, USA*

[4]*Gemini Observatory, Northern Operations Center, 670 North A'ohoku Place, Hilo, HI 96720, USA*

[5]*SASER Team, 269 Domain Road, South Yarra, Vic 3141, Australia*

[6]*Department of Physics and Astronomy, University of British Columbia, 6224 Agricultural Road, Vancouver, BC V6T 1Z1, Canada*

[7]*Department of Mathematics, Physics & Geology, Cape Breton University, 1250 Grand Lake Road, Sydney, Nova Scotia B1P 6L2, Canada*

[8]*Institute for Computational Astrophysics, Dept. of Astronomy and Physics, St Mary's*

University Halifax, NS B3H 3C3, Canada
[9]*University of Vienna, Institute for Astronomy, T ürkenschanzstrasse 17, A-1180 Vienna, Austria*
[10]*Dept. of Astronomy and Astrophysics, University of Toronto, 50 St George Street, Toronto, ON M5S 3H4, Canada*
[11]*Harvard-Smithsonian Center for Astrophysics, 60 Garden Street, Cambridge, MA 02138, USA*

Abstract

WR 71 (HD 143414) is an extreme runaway WN6o star, located $\sim$ 700pc below the Galactic plane and previously suspected to harbour a compact companion in a $\sim$ 7.7 d orbit. To look for any signatures of rapid rotation, possibly induced from Roche lobe overflow spin-up in a close binary, we have obtained a continous month of optical photometry from the MOST (Microvariability and Oscillations of STars) space micro satellite. In an attempt to confirm or disprove its binary status, we have also obtained ground-based optical spectroscopy (some in parallel with the MOST observations). We detect a $\sim$ 1.7 d and $\sim$ 3.4 d period from the first and second ($\sim$equal) portions of the MOST light curve, respectively and no obvious coherent radial velocity shift from the spectra. We therefore consider the evidence for binarity to be lacking. Instead, we believe the strongly variable photometric and spectroscopic data to be a consequence of corotating interaction regions (CIRs) as seen in other WR- and especially O-stars. Assuming the rotation period to be $\sim$ 3.4 d, WR 71 would have a surface rotation velocity of $\sim 104\,\mathrm{km\,s^{-1}}$. Thus, WR 71 does not appear to be rapidly spun up disfavouring the supernova ejection mechanism (recoil from the disruption of a binary system) as that responsible for its extreme runaway status. Using Hipparcos proper motions, observed radial velocity and an estimated distance, we retrace WR 71 back to the Galactic plane and determine a peculiar velocity upon ejection of $\sim 319\,\mathrm{km\,s^{-1}}$. WR 71's high peculiar velocity is virtually unachievable by the supernova ejection scenario, supporting the alternative dynamical ejection

scenario from a young dense open cluster.

Keywords: stars: individual: WR 71 – stars: mass-loss – stars: winds, outflows – stars: Wolf-Rayet – stars: kinematics and dynamics.

3.1 Introduction

As extreme population I, the vast majority of massive WR stars lie within ~ 100 pc of the Galactic plane (GP), with typical mean distance of $|z| = 35$ pc (Rosslowe & Crowther, 2015). A few lie much further and are denoted runaways. In particular, there are five pop I WR stars more than 500 pc (this distance is arbitrary; it was chosen to be able to concentrate on the most extreme runaways) from the GP: WR 64, 93a & 148 above and WR 71 & 123 below the plane (Rosslowe & Crowther, 2015), assuming of course that they are indeed pop I. [If they were [WR] CSPN (Crowther, 2008) or V Sge nova-likes (Steiner & Diaz, 1998) with spectra similar to those of pop I WR stars, this would no longer apply.]

Some runaways can be found by their large peculiar velocities and need not necessarily be far from the GP. For example, WR 124, a WN8h star (Moffat et al., 1982), has a peculiar radial velocity of ~ 200 km s^{-1} , a record for WR stars, based on spectral line shifts of both the star and its surrounding nebula, M1-67 (Grosdidier et al., 1998).

Another study previously dealt with WR 123 (Lefèvre et al., 2005), WN8o, a single star with a high level of photometric variability, like all WN8 stars (Antokhin et al., 1995; Marchenko et al., 1998b). But some of its variability gives a suspected period of 10h, the first in a WR star to be claimed to be seriously related to non-radial pulsations (NRP). However, there is no obvious link of this oscillation to its extreme runaway status.

Among the five extreme WR stars further than ~ 500 pc from the GP, only WR64 (WC7) & WR93a (WN2.5-3 or WN6) remain to be examined in detail and only 2 WR stars have binarity mentions: WR 148, a confirmed binary system (Bracher, 1979) and WR 71, a suspected binary system (Isserstedt et al., 1983).

We presented a detailed study on WR 148 in a first paper (Munoz et al., submitted.):

a massive binary WN7ha+O5V system at $\sim$ 800 pc above the GP, that must have been slung out of a forming young cluster in the GP (where virtually all such clusters are formed) rather than from a SN explosion in a close hierarchical tertiary (the competing hypothesis for this current runaway binary). Here we examine WR 71 = HD 143414, a WN6o star without significant hydrogen, lying $\sim$ 700 pc below the Galactic plane. WR 71 is suspected to harbour an unseen companion in a relatively short $\sim$ 7.7 d period system (Isserstedt et al., 1983).

First, we look for fast rotation from possible spin-up during the Roche lobe overflow (RLOF) process preceding a SN binary recoil scenario that led the runaway to high $|z|$. Then, we search for any binarity signatures and explore other ejection mechanism scenarios. We conclude in the final section.

3.2 Observational Data

3.2.1 Optical photometry

Continuous time-dependent optical photometry was obtained in 2014 from May 29th to June 24th using the MOST micro-satellite (Walker et al., 2003). Equipped with a 15 cm Rumak-Maksutov telescope, mounted onto a CCD photometer via a broadband optical filter (350-750 nm), MOST is designed to detect low-amplitude stellar oscillations with a precision of a millimagnitude or better. On its polar, sun-synchronous, low-Earth 101.4 min orbit, MOST can provide up to 8 weeks of uninterrupted observations. During one orbital revolution, roughly 15 data points are taken at intervals of 2.3 min.

3.2.2 Optical spectroscopy

Complementary to the optical photometry, we obtained ground-based spectroscopy from three independent sources. Table 3.I summarizes the details of the spectroscopic observations.

The first two data sets were collected in 2014 by TB and BH. TB collected two spectra from Armidale NSW Australia using a 0.28m telescope with low resolving power, compensated by a wider spectral range. Located in Melbourne Australia, BH provided the densest dataset with 9 spectra over the course of 2 months, 4 of which overlap in time with the MOST data. With a 1800 lines/mm grating and a 0.28m telescope, BH achieved a resolving power of ∼6300 and a signal-to-noise ratio of ∼50 per pixel in the continuum mainly to focus on He II λ4686.

Finally, the last contribution, consisting of 5 consecutive nights was generously provided from Chené & St-Louis (2011), hereafter AN. Although AN's dataset is well outside the MOST observations, it is invaluable to test for short orbital periods of the order days for WR 71. All data were received, reduced and normalized utilizing standard IRAF[1] techniques. A sample WR 71 spectrum is displayed in Fig. 3.1.

3.3 Analysis and results

3.3.1 Photometric Extraction and Instrumental Corrections

The MOST satellite observed the WR 71 field for 26.8 days. Two stars were observed in direct imaging mode with 20x20 pixel subrasters and integration times of 123.41s, one of which contained WR 71. To extract time-series photometry we used the MOST software[2] tool **allmost** (Rowe et al., 2006, 2008) to measure the positions, PSF shapes

---

[1] IRAF is distributed by the National Optical Astronomy Observatories, which are operated by the Association of Universities for Research in Astronomy, Inc., under cooperative agreement with the National Science Foundation

[2] The MOST direct imaging photometry codebase used in this paper is available at: https://github.com/jasonfrowe/MOST

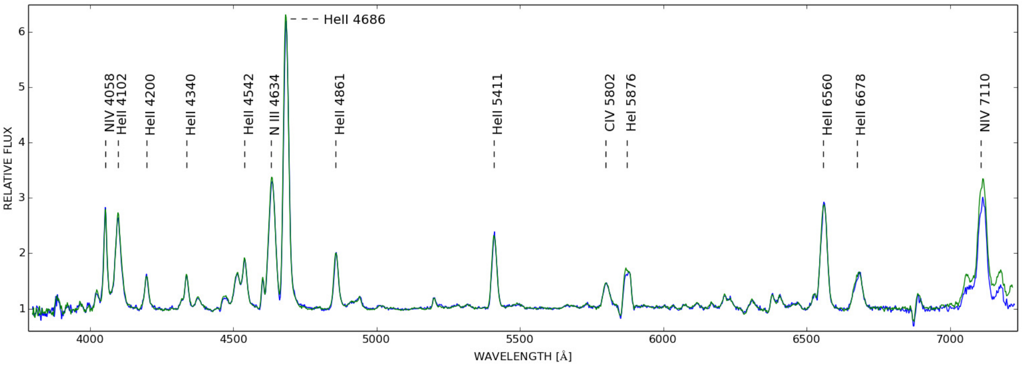

Figure 3.1: Sample spectrum from TB

Table 3.I: Summary of spectroscopic observations

Telescope	Dates		No. of spectra	Spectral range [Å]	Resolving power	S/N
TB (0.28m)	2014	July 30 - August 08	2	3800 - 7225	$\sim$1400	$\sim$50
BH (0.28 m)	2014	July 25 - August 23	9	4570 - 4790	$\sim$6300	$\sim$50
CTIO[†] (1.5 m)	2004	July 02 - July 06	5	5200 - 6000	$<$ 140000	$\sim$100

[†] Data provided from Chené & St-Louis (2011)

and fluxes of stars imaged in each subraster simultaneously. **allmost** uses a PSF model based on a 2D Gaussian to measure the position of the star and characterize the PSF shape. The star position is then used to place a photometric aperture with a radius of 4 pixels to estimate the flux from the target star. The median value of all pixels more than 8 pixels away from the star position was used as an estimate of the sky background. Valid photometry was extracted for 7520 frames.

Outliers in the raw photometry were identified using the MOST software tool **autocut**. This tool examined the distributions of the measured star locations and PSF directional widths of WR 71 to calculate median values for each parameter. Observations with a parameter value that was more than 3σ away from the median value were rejected. This step reduced the number of valid observations from 7520 to 5515. Observations that show significant motion in the star position of anomalous PSF shapes are typically associated with significant point jitter on timescales shorter than the integration time. In this case, it is very likely that flux from the target star was not contained within the photometric aperture. Inspection of the lightcurve before and after this cut showed a significant decrease in the number of deviant flux measurements. Since WR 71 was a shared target, larger jitter is expected.

MOST aperture photometry is known to be strongly correlated to the sky background. The timescale of stray light modulation is equal to the orbital frequency of the MOST satellite, 14.1 c/d. The correlation amplitude was observed to be smaller than true photometric variations from WR 71; thus special care was taken to decorrelate the stray light correction from time variability inherent to WR 71. The first step was to calculate the Fourier decomposition of the clipped MOST WR 71 lightcurve using the

MOST software tool, **mostper**. **mostper** was used to estimate the Fourier transform of the non-uniformly sampled lightcurve of WR 71 from 0 to 10 c/d with 8- times oversampling. The upper limit was chosen to exclude the MOST straylight signature of the analysis. The frequency with the largest amplitude was identified. Least-square fitting was then used to refine the frequency, amplitude and phase. The signal was then removed from the lightcurve and the Fourier transform was then calculated using the residuals. The next strongest peak was then identified and fit. These steps were repeated until the signal-to-noise of the identified signal was less than 4. At each iteration all identified frequencies are simultaneously refit. In total 16 frequencies were identified.

The identified frequencies are considered intrinsic to the star and were temporarily removed from the clipped lightcurve. The residuals were then used to fit for instrumental correlations. We used the MOST software tool **mostfit4** to simultaneously fit for the sky-flux and position-flux correlation. The latter is due to intrapixel variations common to CCD detectors. The sky-flux, column-flux and row-flux correlations were each modeled with a third-order polynomial. The model was then used to decontaminate the original clipped lightcurve, thus preserving the intrinsic large amplitude variability of WR 71. An additional 14 strong outliers were identified and removed. These measurements were likely the result of cosmic ray hits within the WR 71 subraster.

3.3.2 Photometry

Presented in Fig. 3.2a is the reduced MOST light curve with the MOST orbital means overplotted. WR 71 appears to be highly variable with short-term photometric fluctuations reaching up to $\sim$ 0.06 mag. The most prominent feature in the light curve is the abrupt change in overal slope at HJD=2451545+5274, after which, on a timescale of $\sim$14 d, roughly half the duration of the total observations, the light curve ramps up, quickly decreases, and recuperates with a similar slope. This corresponds to the dominating frequency seen in the time-frequency plot at $\sim$ 0.07 c/d (see bottom panel in Fig. 3.3a) along with the Fourier (Scargle, 1982) and phase dispersion minimization (PDM) (Stellingwerf, 1978) analyses (see top two panels in Fig. 3.3a) which were obtained from the binned light curve. If this behaviour is linked to the MOST orbit, then it should be manifested in other targets in the same field as WR 71. As can be seen in Fig. 3.12, the guide stars do not exhibit similar behaviour, thus indicating that this overlying long-term trend in WR 71 is likely to be real.

Regardless of the nature of this long-term trend (for which we have no viable explanation), we cannot provide a thorough analysis on it as it barely even spans two cycles in the data set. We therefore subtract a spline-fitted curve in an attempt to remove it. The resulting detrended light curve and corresponding time-frequency plots are shown in Figs. 3.2b and 3.3b. Detrending the data enhances the power of shorter periods and enables us to see a clear break in the time frequency plot at HJD 2451545+5274. In fact, below this pont in time, a ~ 1.7 d period dominates, whereas above it, the periodicity transitions to twice this value, i.e. ~ 3.4 d. We henceforth split the data accordingly in two parts: parts 1 and 2 for the segments of the light curve before and after HJD 2451545+5274, respectively. From an intensive photometry compaign, Balona et al. (1989) also reported a periodicity of 1.75 d in a long term increasing trend of 0.1 mmag, similar to our findings.

Scargle and PDM analyses are applied to both parts of the light curve individually to refine their corresponding periods. Their periodograms, illustrated in Fig.3.4a and Fig. 3.4b, reveal singly dominating periods of $P_1 = 1.7 \pm 0.1$ d and $P_2 = 3.4 \pm 0.4$ d respectively. No higher-order harmonics were detected, implying sinusoidal-like structures in the light curve. We note, however, that the first portion of the data is contaminated by a 1-day period alias residual, associated with the Earth's rotation rate, and that the second portion is still affected by residual high-frequency signals. Figs. 3.5a and 3.5b show the phase-folded light curves of parts 1 and 2 to their respective periods. Though somewhat noisy, binning the phased light curves reveals two quasi-sinusoidal signals; as expected in the absence of higher-order harmonic terms. The scatter may be a consequence of a fluctuation in amplitude. In fact, throughout each part of the light curve, we notice an amplification of the variations while the period remains approximately constant, possibly due to stochastic clumping in the wind, as seen in all hot-star winds (Lépine & Moffat, 2008).

In Fig. 3.2b, we indicate with time arrows the peaks of the light curve recurring at the corresponding periods. A phase shift of ~ 0.22 at P_1 is necessary at the transition from part 1 to part 2 of the light curve in order to make the time arrows coincide with the peaks of both segments simultaneously. This timely behaviour is reminiscent of the photometric modulation observed in WR 110, a MOST target conjectured to harbour corotating interaction regions, otherwise known as CIRs. Chené et al. (2011) interpret the detected dominating period of ~ 4.08 d as overdensity structures rotating in the wind. In the particular case of WR 71, the light curve shows an abrupt change in shape but with a constant rotation of $P_2 = 2P_1$. Interestingly enough, the detected periods are within a factor of two apart. We thus speculate that a common mechanism gives rise to both periodicities. CIRs are typically modelled with one or two spiral arms rotating in the wind (Cranmer & Owocki, 1996a). It is fairly straightforward to see how a ~ 3.4 d rotating WR star harbourig two CIRs could reproduce the detected ~ 1.7 d period in the first section of the light curve. For the second section, there could have been a transition from one set of bright spots [needed to trigger the CIRs (Cranmer & Owocki, 1996b)] during the CIRs, to another set, of which only the strongest pair is seen in the first part, and the strongest single one in the second part.

3.3.3 Spectroscopy

The purpose of the spectroscopic campaign was twofold: provide a complementary analysis to the photometric MOST light-curve and verify WR 71's possible binary nature reported in Isserstedt et al. (1983). However, with only four days of simultaneous coverage between the BH dataset and the light curve, we were not able to establish a reliable link between the photometric and spectroscopic variations.

We therefore proceed by measuring the radial velocities (RVs) of He II $\lambda 4686$ from the richer, higher-quality BH dataset (see Fig 3.6a). This is done by means of the bisector method (i.e. the radial velocity refers to the centroid of the line). Fig. 3.6b displays the RV measurements and their values are tabulated in Table 3.II. The WR 71 spectra do appear to be highly variable, with RV variations in the same order of magnitude as the proposed orbital amplitude from Isserstedt et al. (1983). Upon further inspection, we note, however, that the red- and blue- wing velocities move in anti-phase. This

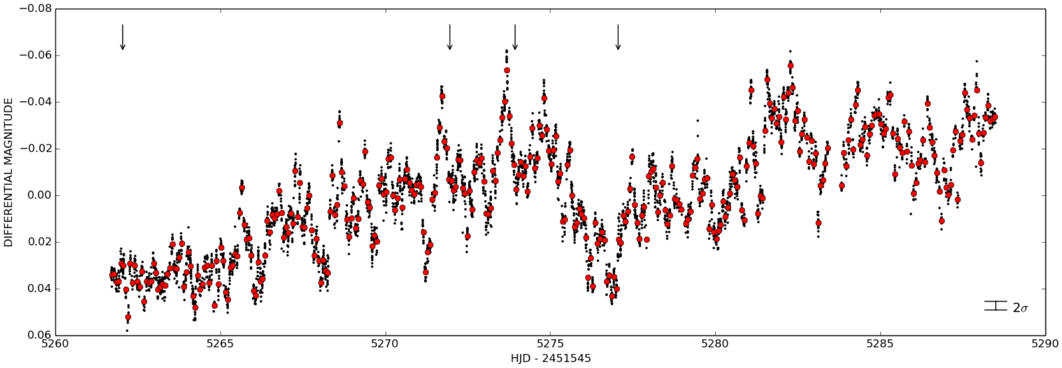

(a)

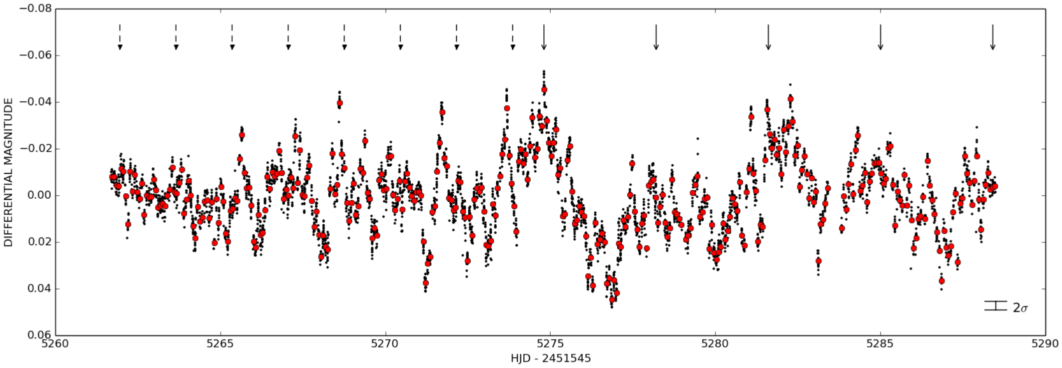

(b)

Figure 3.2: (a) MOST light curve of WR 71 with orbital bins overplotted. Time arrows indcate where ground based spetroscopy was obtained. (b) Detrended MOST light curve of WR 71 with orbital bins overplotted. Time arrows indicate intervals of 1.7 d before HJD 2451545 and intervals of 3.4 d afterwards. A 0.44 phase shift (of the first period) was introduced while transitioning from one evenly spaced interval to the other. 2σ errorbars for the unbinned light curves are indicated at the bottom right corner.

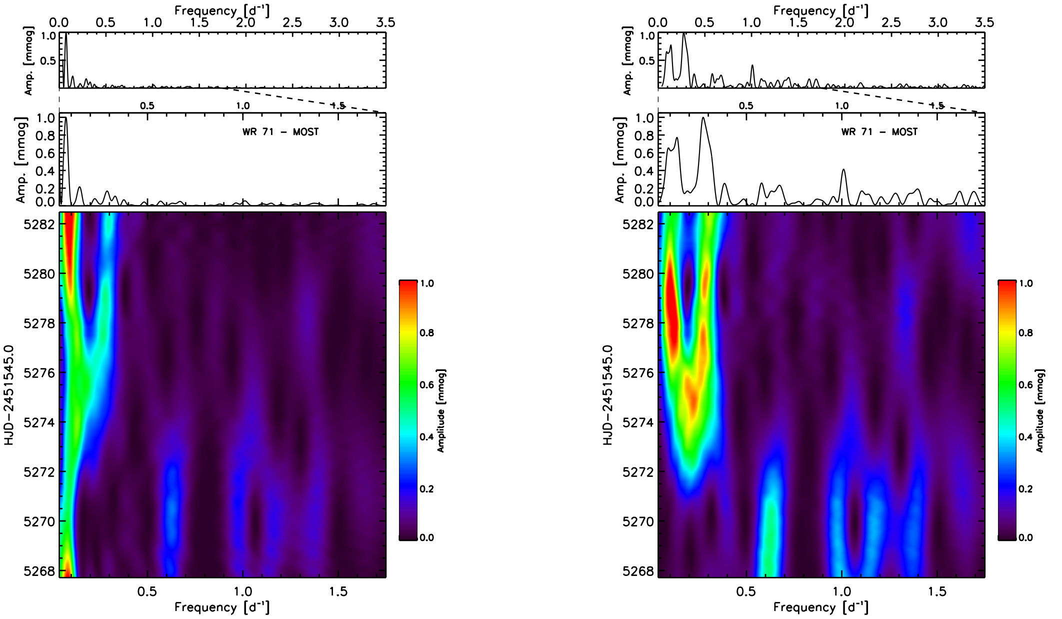

(a) (b)

Figure 3.3: Top panel: Lomb Scargle periodogram of the binned (a) original and (b) detrended MOST light curve in Fig. 3.2a and 3.2b, respectively. Middle panel: zoomed version of the top panel. Bottom panel: time-frequency analysis for WR 71 with 8-day running window in time.

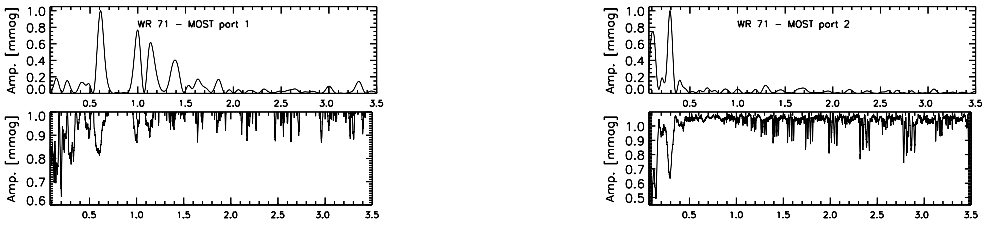

(a) (b)

Figure 3.4: Scargle and PDM analyses for (a) part 1 (before HJD 2451545+5274)and (b) part 2 (after HJD 2451545+5274) of the binned detrended MOST light curve in Fig. 3.2b.

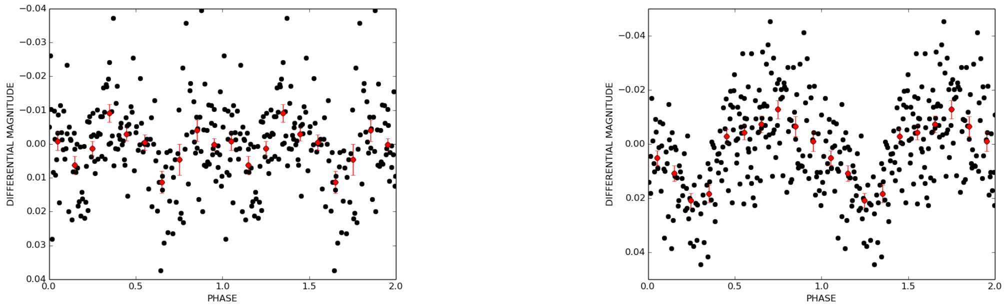

(a) (b)

Figure 3.5: Phased light curve for (a) part 1 (before HJD 2451545+5274) and (b) part 2 (after HJD 2451545+5274) of the binned detrended MOST light curve in Fig. 3.2b using a constant period of $P = 3.4$ and same zero point of HJD $2451545 + 5265.63$ (arbitriarily chosen to correspond to the first peak in the MOST detrended light curve). Overplotted are means in phase bins of 0.1 with 2σ errorbars corresponding to the standard error of the mean in each bin.

is uncharacteristic for spectroscopic binaries, where the red- and blue-wing velocities should move coherently. This so-called ”line-breathing” effect can be stronger on one side of the wing than the other (e.g. the right wing displaces at a higher amplitude than the blue wing or vice versa). Hence, once the red and blue wings are combined, this gives the false impression of a global RV shift.

The electron scattering wings in the broad WR emission line are proportional to the density of the wind and are thus sensitive to wind inhomogeneities. This is the very nature of clumping. However, these small-scale variations typically dissipate in a matter of hours (Lépine & Moffat, 1999c). Given the sparsity of the BH spectra, the propagation of wind-clump activity should pass undetected. Then, perhaps these line perturbations could also be linked to CIRs, rather than clumps, or to both. Overdensity structures rotating with the wind should in principle produce line-profile variations on a longer timescale (depending on the rotation period) than that of clumps. If this is the case, then periodic modulations in the calculations of moments (e.g. equivalent width, full width at half maximum, skewness and kurtosis) are expected. WR 71 needs to be further monitored by a more extensive spectroscopy campaign in order to confirm or disprove this hypothesis.

Table 3.II: He II λ4686 and He II λ5411 radial velocities.

Dataset	HJD - 2451545	RV [$\mathrm{km\,s^{-1}}$]
BH	5271.9586	-83 ± 13
	5273.9355	-94 ± 14
	5277.0580	-91 ± 7
	5289.9835	-126 ± 6
	5306.0104	-95 ± 12
	5309.9295	-82 ± 8
	5314.9997	-95 ± 12
	5324.0195	-25 ± 9
	5328.9673	-48 ± 14
AN	1644.7057	-99 ± 13
	1645.6689	-121 ± 10
	1646.6144	-92 ± 15
	1647.5956	-120 ± 14
	1648.5983	-101 ± 8

We now refer to the previous spectroscopic observations from Chené & St-Louis (2011). The evenly sampled data coverage from AN should be able to detect the ~ 7.7 d orbital period claimed in Isserstedt et al. (1983). As there is no overlap in spectral range between the AN and BH datasets, we measure the RVs based on He II λ5411, the strongest line in AN's spectral range (see Fig. 3.7a). Fig. 3.7b shows the RV measurements and their values are listed in Table 3.II. As can be seen in Fig. 3.7b, there is no obvious coherent RV variation as we would expect from a binary system with a 7.679 d period, suggesting that the spectroscopic variations are in fact intrinsic to the star and not related to any binary motion. We therefore exclude the possibility that WR 71 is a short period binary. It is difficult to ascertain the source of these variations with the limited number of spectra. Nevertheless, as stated by Chené & St-Louis (2011), WR 71 is a marginal candidate for CIRs based on the temporal variance spectrum. This further supports the idea that WR 71's spectroscopic variability may indeed be linked to CIRs.

To confirm WR 71's runaway status, we measure its systemic velocity based upon the N IV λ4058 line. Using TB's dataset, the only dataset covering this region, we obtain a rather large systemic velocity of -240 ± 10 $\mathrm{km\,s^{-1}}$. The N IV $\lambda 4058$ line is typically considered the most reliable to reflect the true motion of a late WN subtype because it is a relatively narrow and symmetric line formed quite deep in the WR wind. However, WR emission lines broaden and shift for hotter spectral types, thus hindering the RV measurements. Consequently, this technique may not be entirely suitable for a WN6o star such as WR 71. WR+O binaries are thus invaluable in verifying the true systemic velocity of a system because the O star's absorptions lines are less afflicted by Doppler broadening and do reflect the motion of the star. Measuring the O star's systemic velocity (γ_{O}) in comparison to that of the WR star (γ_{WR}) allows us to gauge the reliability of γ_{WR}. While in CQ Cep, a WN6o+O9II-Ib binary, γ_{WR} and γ_{O} are consistent (Marchenko et al., 1995), in V444 Cygni, a WN5o+O6III-V system, γ_{WR} is blueshifted by roughly 50 $\mathrm{km\,s^{-1}}$ (Underhill et al., 1988). We will thus conservatively consider a wider uncertainty range of -240^{+10}_{-50} $\mathrm{km\,s^{-1}}$ for WR71's systemic velocity.

3.3.4 Runaway status

Runaways are stars characterized by their unusually large peculiar space velocity. The minimum threshold, above which massive stars are considered to be runways, is typically set at 30 $\mathrm{km\,s^{-1}}$ (Dray et al., 2005). If ejected perpendicular to the GP, runaways can be found high above the GP. For such stars to achieve large spatial velocities, two competing ejection mechanisms are generally accepted:

1. Binary ejection scenario (BES) : Single runaways arise from the possible disruption of close binary systems subsequent to a supernova explosion (Blaauw, 1961). Binary runaway systems could arise from the recoil of surviving bound systems.

2. Dynamical ejection scenario (DES) : Runaways arise mainly from three- or four-body encounters in dense forming young open clusters (Poveda et al., 1967).

BES runaways typically possess high rotational velocities and an increased helium abundance as a result of close binary evolution (e.g. RLOF), whereas, DES runaways are not

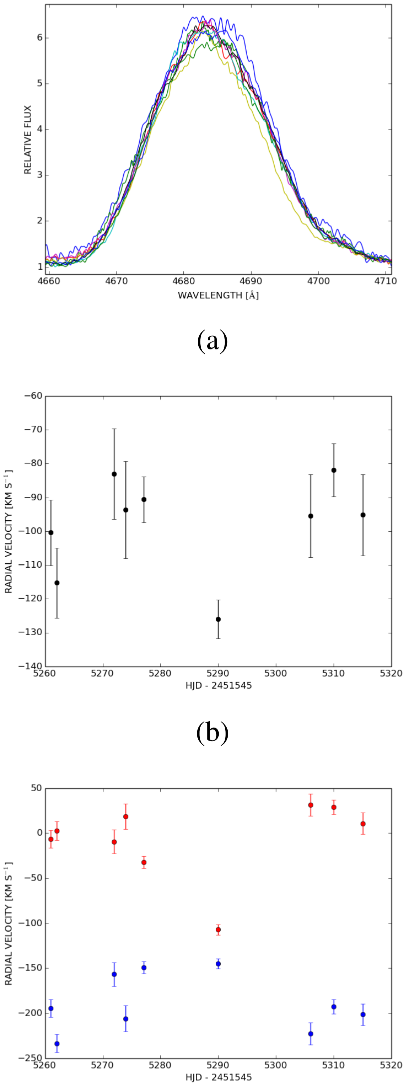

(a)

(b)

(c)

Figure 3.6: (a) Superimposed spectra from BH zoomed on He II λ4686. (b) Measured radial velocities. (c) Red and blue wings of the measured radial velocities.

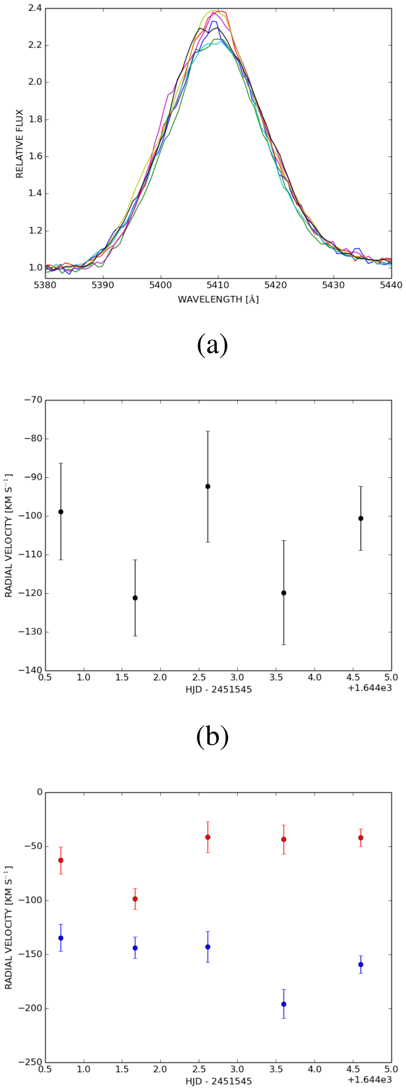

(a)

(b)

(c)

Figure 3.7: (a) Superimposed spectra from AN zoomed on He II λ5411. (b) Measured radial velocities. (c) Red and blue wings of the measured radial velocities.

expected to demonstrate theses signs (Hoogerwerf et al., 2001). Furthermore, the kinematic age of supernova-ejected runaways, defined as the travel time for the runaway to reach its current position upon ejection, is significantly shorter than the age of their parent group (the close binary system) as it may take several Myr for the original primary to undergo a SN explosion. Conversely, the kinematic age of a dynamically ejected runaway is nearly identical to the age of its parent group (the young open cluster), as DES runaways are effectively ejected at the zero-age-main sequence (Hoogerwerf et al., 2001). These are important factors to consider in order to determine the ejection mechanism responsible for WR 71.

To get a handle on WR 71's kinematic age, we attempt to retrace its trajectory back to the GP. Using the spectroscopic radial velocity, Hipparcos' proper motions, and an estimated distance (see Table 3.III), we recreate its spatial velocity and integrate its orbit back in time. As done in Hoogerwerf et al. (2001), the orbits are integrated numerically with a fourth-order Runge-Kutta method in a Galactic potential consisting of a three-component model: a logarithmic potential for the halo and a Miyamoto-Nagai potential for the disk and bulge of the Galaxy with parameters recently refined by Irrgang et al. (2013). Prior to the orbit integration, the star's heliocentric velocity, $v_{\star}$, must be corrected for the velocity of the Sun relative to the local standard of rest (LSR), $v_{\odot}$, and for the rotational velocity of the LSR relative to the Galactic center, $v_{\rm LSR}$. In the Galactic barycentric frame, $v_{\star}$ will thus be given by

$$v_{\rm gal} = v_{\star} + v_{\odot} + v_{\rm LSR}, \tag{3.1}$$

where $v_{\odot} = (10.00, 5.23, 7.17)$ km s^{-1} (Dehnen & Binney, 1998) and $v_{\rm LSR} = (0.0, 220.0, 0.0)$ km s^{-1} (Binney & Tremaine, 1987).

Finally, we performed 1000 Monte Carlo simulations to scope the error space in proper motions and distance. We obtained a mean kinematic age of 5.9±1.1 Myr, a mean peculiar velocity upon ejection of 319±27 km s^{-1} and a mean peculiar velocity of 269±30 km s^{-1} at its current location. This trajectory time is compatible with the lifetimes of stars with initial masses in the range of 25-40$M_{\odot}$ (Meynet & Maeder, 2003), which is consistent with the current mass and mass-loss rate modelled for WR 71 from Hamann et al. (2006b). Indeed, adopting, $M_{\rm WR} = 20 M_{\odot}$, $\log \dot{M} = -4.7 M_{\odot}$ yr^{-1} and assuming a WR-phase lifetime of 0.5 Myr, yields an initial mass $30 M_{\odot}$. Regarding WR 71's ejection velocity, it is quite high even in the runaway category. Portegies Zwart (2000) show that the maximum attainable velocity for massive BES runaways does not typically exceed 200 km s^{-1} . On the other hand, according to the extensive three body scatterings conducted from Gvaramadze & Gualandris (2011), although rare, massive DES runaways could achieve peculiar velocities above 350 km s^{-1} . The DES ejection scenario is therefore the most likely case for WR 71.

DES runaways should in theory be traceable back to their parent open cluster. Though, in practice, this is difficult to perform as the errors on proper motions and distance become increasingly large with extreme runaways. Such is the fate for WR 71. Fig. 3.8 illustrates the wide dispersion in WR 71's position, traced back to the GP. While the error ellipse spans at most 3kpc, the localization of the known OB associations in the GP (Mel'Nik & Dambis, 2009) is mostly confined to the solar neighborhood and is not known anywhere near where WR 71 crosses the GP. Determining WR 71's parent association is thus impossible with present data.

3.4 Discussion

3.4.1 Bow Shock

If a runaway's peculiar velocity is supersonic with respect to a sufficiently dense ISM, a bow shock can occur in the direction of motion of the star. First noted by Marston et al. (1994b), Stock & Barlow (2011) confirmed the presence of an ejecta nebula surrounding WR 71 in the Southern Hα Survey (SHS). The SHS image shown in Fig. 3.9 shows a noticeably denser side to the south. The vector of the peculiar motion of WR 71 is directed towards this region of enhanced emission as expected from the presence of bow shocks (Moffat et al., 1998). This confirms WR 71's runaway status and general peculiar motion in the plane of the sky.

Table 3.III: WR 71 spatial parameters

Parameters	Values	Reference
l [deg]	323.0812	[1]
b [deg]	-07.6127	[1]
$\mu_\alpha \cos\delta$ [mas yr^{-1}]	-6.89 ± 1.45	[1]
μ_δ [mas yr^{-1}]	-13.66 ± 1.60	[1]
d [kpc]	5.34 ± 1.05	[2]
v_r [km s^{-1}]	-240 ± 10	[3]

[1]van Leeuwen (2007),[2]Rosslowe & Crowther (2015),[3]this paper

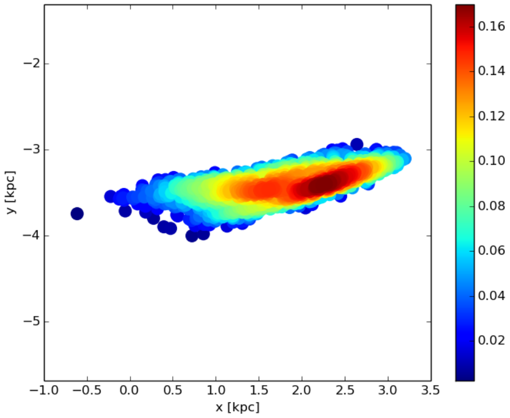

Figure 3.8: Probability distribution of the possible launching sites of WR 71 back in the Galactic plane. The sun is located along the y axis at $R_0 \simeq 8.5 R_\odot$.

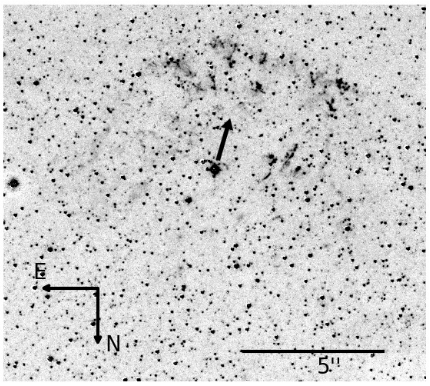

Figure 3.9: Peculiar proper motion vector superposed on an ISM emission map surrounding WR 71. The map is provided from Stock & Barlow (2011).

3.4.2 Rotation Period

Assuming that the rotation period is plausibly $\sim$3.4 d, we obtain a rotation velocity of $v_{\mathrm{rot}} = 2\pi R_*/P_{\mathrm{rot}} \sim 104$ km s^{-1} (which would project to even lower values for $\sin i < 1$), where R_* is the WR's core radius. This is significant yet quite far from the critical rotation speed of $v_{\mathrm{crit}} = \sqrt{GM/R_*} \sim 735$ km s^{-1} where G is the gravitational constant and M is the WR's mass. Here we have adopted $R_* = 7R_\odot$ and $M = 20M_\odot$, the optimized values for the stellar mass and radius for WR 71 were obtained via the Potsdam Wolf-Rayet Models (PoWR) from Hamann et al. (2006b).

According to Shara et al. (2015)'s study on spin rates of O stars in close massive WR+O binary systems, the O stars spin up by RLOF and, typically achieve rotational velocities ranging from 140 to 496 km s^{-1} . However, how the transition from O to WR star affects the rotation period is somewhat elusive. While the WR's continuous mass loss (and thus loss in angular momentum) leads to a decrease in rotation, its ever contracting core induces an increase in rotation (Shenar et al., 2014b). Meynet & Maeder (2003) computed evolutionary tracks of massive rotating stars (with initial rotational velocities of 300km s^{-1} and at solar metallicity) and monitored various stellar parameters, and in particular, the surface rotational velocities of WR stars. Despite the two opposing processes, they obtained a rather constant rotational velocity throughout the WR lifetime, which settled down to a relatively low 50-100 km s^{-1} . It is therefore not obvious if WR 71 was spun up during a RLOF event in a pre-SN binary, since its speculated rotational velocity is in the same order of Meynet & Maeder (2003)'s predictions for single evolving massive stars with an initial rotational velocity of 300 km s^{-1} . This does not exclude this scenario, but opens the door more to the other scenario of a slingshot effect from a young forming dense cluster.

3.4.3 CIR model

Up to now, we have only characterized WR 71's photometric variability qualitatively. For a more rigorous analysis, we attempt to apply Chené et al. (2011)'s CIR model to the MOST observations. Chené et al. (2011) devised a CIR model, analogous to a self eclipsing model, to describe the photometric variations in WR 110. It is an adapted form of the Lamontagne et al. (1996) atmospheric eclipse model widely used in the framework of WR+O binaries. However, instead of an O star (assumed to be a point source) rotating in a WR wind located at the system's orbital separation, it is the brightest part of a CIR rotating through the WR wind located at a certain radius from the photosphere, defined as $R_s = \gamma R_*$, where $\gamma > 1$ is a constant. In this context, Chené et al. (2011) defined the differential magnitude as

$$\Delta m = \Delta m_0 - 2.5 \log_{10} \left(I_{WR} + I_s e^{-\tau} \right), \tag{3.2}$$

where Δm_0 is a constant, I_{WR} is the intensity of the WR star, I_s is the intensity of the CIR and the opacity, τ is given by the integral

$$\tau = k \int_{z_0}^{\infty} \frac{d(z/R_s)}{(r/R_s)^2 (1 - R_*/r)^{\beta}}, \tag{3.3}$$

with $z_0 = -\sin i \cos 2\pi\phi$, $(r/R_s)^2 = \cos^2 i \cos 2\pi\phi + \sin^2 2\pi\phi + (z/R_s)^2$ and the dimensionless parameter

$$k = \frac{\alpha \sigma_t \dot{M}}{4\pi m_p v_\infty R_s}, \tag{3.4}$$

where σ_t is the free electron Thomson cross section, m_p is the proton mass, α is the number of free electron per baryon, β is the velocity law index, v_∞ is the terminal velocity, i is the inclination angle about the rotation axis (which is assumed to coincide with the CIR rotation axis) and ϕ is the rotational phase. The subscript s stands for spot, the driving mechanism for the CIR arising at the base of the wind. Where the CIR protrudes from the wind and is visible to the observer is assumed to be optically thin. We wil therefore only consider the optically thin case.

The solution to the integral in equation 3.3 is only analytic for integer values of β. As we adopt the physical parameters for WR 71 from Hamann et al. (2006b), where β is assumed to be unity, we fix $\beta = 1$ for consistency. Taking $\alpha = 0.5$, suitable for a wind dominated by He^{++}, and $v_\infty = 1200\ \mathrm{km\,s^{-1}}$ (Hamann et al., 2006b), yields $k = 0.34/\gamma$. Due to the degeneracy on the inclination angle in equations 3.2 and 3.3, the model does not converge if i is left as a free parameter. To remedy the situation, we proceed by fixing i to a selected few discrete angles. This reduces the total number of free parameters to the following: Δm_0, I_{WR}, I_s and γ for each value of i.

We first attempt to fit equation 3.2 to the phased binned light curve for the first portion of the data (before HJD 2451545+5274). Both peaks of the double wave in Fig. 3.5a are fitted simultaneously with a pair of spots both satisfying equation 3.2 with same Δm_0 and I_{WR} though with independant I_s and γ (totalling six free parameters for the pair). By design, the CIR model fits a peak at 0.5 phase. Two phase shifts are therefore manually imputed to fit the two waves at ~ 0.25 and 0.75 (see Fig. 3.10). Table 3.IV lists the best-fitted values and their reduced χ^2 (χ^2_{red}) while ranging the inclination from 5° to 90° with an increment of 5°. Beyond an inclination of $i > 30$, the model does not converge. These results are therefore omitted from the table. In all cases, χ^2_{red} is relatively constant so we cannot discriminate between the inclination angles from this criterion alone. Since cases where the spot is brighter than the star are not physical, we can exclude the angles where $I_{WR}/I_s \ll 1$. Furthermore, since the spot needs to be formed somewhere within WR's extended envelope, most likely in the vicinity of the WR's core radius, we can also exclude cases where $\gamma \gg 1$. Inclination angles between 10° to 30° seem to best satisfy these criteria. Though the likelihood of observing such small inclination angles is low, the model at $i = 10°$ is shown in Fig. 3.10.

We next attempt to reproduce the shape of the binned light curve for the second portion of the data (after HJD 2451545+5274) with a linear combination of the two modelled peaks obtained in Fig. 3.10. The pair of spots, giving rise to the double wave in the binned light curve from the first section, may have merged or blended through time, giving rise to a single wave in the binned light curve from the second section. Indeed, Fig. 3.11 shows a possible scenario where the two peaks are displaced towards each other by a quarter phase and amplified by a constant factor of 1.75. A configuration change of the set of spots may very well be the source for the apparent change in light curve at HJD 2451545+5274. Similar behaviour was also reported in Antokhin et al. (1994) in WR 6. A unique period was found, however the shape of the light curve does not remain coherent throughout extended periods of time. These large-scale variations in WR 6 are suggested to be caused by CIRs. Therefore, we suspect the photometric variations in WR 71 may also be indicative of CIRs.

3.5 Conclusions

- Despite the abrupt change in shape in the MOST light curve at HJD 2451545+5274, the 3.4 d period remains fairly robust.
- The lack of periodic radial velocity shifts suggests that WR 71 is a single runaway.
- The photometric and spectroscopic observations are both strongly variable and possibly indicative of CIRs.
- The suspected 3.4 d rotation period corresponds to a projected rotational velocity of $\sim$ 104 $\mathrm{km\,s^{-1}}$. Within the norm for other WR stars, WR 71 does not show obvious signs of rapid rotation expected from supernova ejected runaways.
- Ejected from the Galactic plane with a high peculiar velocity of $\sim$ 319 $\mathrm{km\,s^{-1}}$, WR 71 was most likely ejected via dynamical interactions in a dense forming cluster $\sim$ 5.9 Myr ago.
- Fitting the phase binned light curve of Fig. 3.5a to Chené et al. (2011)'s CIR model restrains the inclination angle about the rotation axis (which is assumed to coincide with the CIR rotation axis) between 10° and 30°.
- The double wave of the binned light curve for the first section of the light curve can be reproduced by two CIRs originating from a pair of spots. A linear combination of the first two CIRs can reproduce the single wave of the binned light curve for the second section.
- We suspect a configuration change of the pair spots is responsible for the abrupt change in light curve at HJD 2451545+5274.

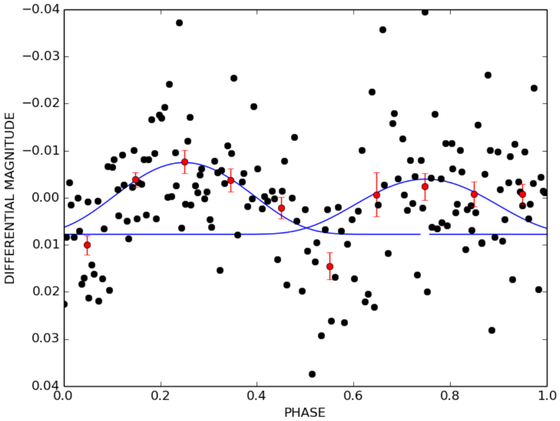

Figure 3.10: Chené & St-Louis (2011) CIR model fitted to the phased binned light curve for the first portion of the data (before HJD 2451545+5274) with a fixed inclination angle of 10°. Overplotted are means in phase bins of 0.1 with 2σ errorbars corresponding to the standard error of the mean in each bin.

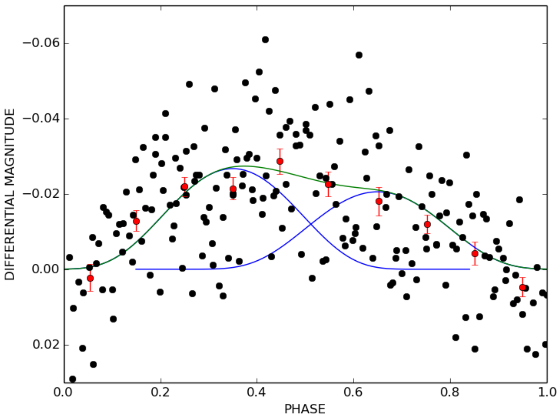

Figure 3.11: Linear combinatin (green) of the first two CIR models (blue) in Fig. 3.10 plotted over the phased binned light curve for the second portion of the data (after HJD 2451545+5274). Overplotted are means in phase bins of 0.1 with 2σ errorbars corresponding to the standard error of the mean in each bin.

Table 3.IV: Best-fittel values for the CIR model

	i	I_{WR}/I_s	γ	χ^2_{red}
First peak	5°	0.07	1.01	2.7972
	10°	1.49	1.02	3.8429
	15°	4.68	1.04	3.7688
	20°	7.53	1.06	3.7666
	25°	9.71	1.10	3.8426
	30°	12.71	1.15	4.2094
Second peak	5°	0.10	1.01	1.9562
	10°	2.14	1.02	2.0049
	15°	11.72	1.07	2.1535
	20°	17.40	1.17	2.2103
	25°	19.27	1.27	2.2384
	30°	18.75	1.27	2.2644

Acknowledgements

AFJM and NSL are grateful for financial aid from NSERC (Canada) and FQRNT(Quebec). We acknowledge the help and support of colleagues at Université de Montréal. NDR acknowledges postdoctoral support by the University of Toledo and by the Helen Luedtke Brooks Endowed Professorship.

Appendix B. WR 71 MOST guide stars

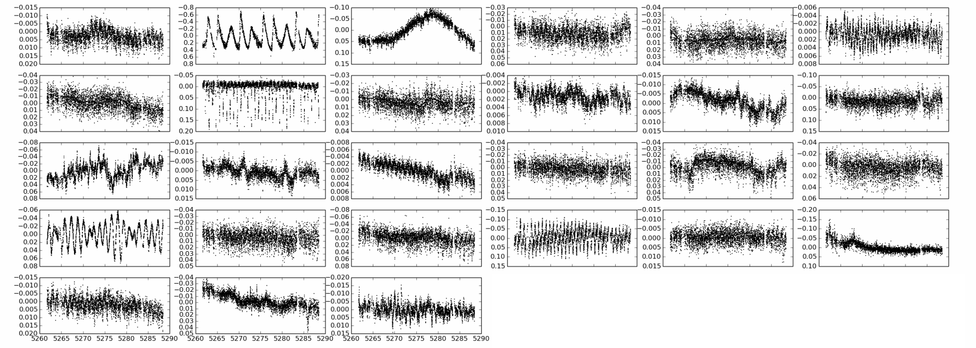

Figure 3.12: MOST light curves of other stars observed in paralled during the WR 71 observations.

Fin de l’article.

CHAPTER 4

LA DISPARITÉ DES ÉTOILES WOLF-RAYETS AU SEIN DES BINAIRES X.

L'acte de conférences qui suit traite de la question ouverte sur la rareté des systèmes binaires WR+cc. Étant donnée la durée de vie d'une étoile WR par rapport à celle d'une étoile O ($\sim 10\%$) et le nombre significatif des systèmes O+cc (~ 114), les descendants des systèmes WR+cc, nous nous attendons à observer $\sim 10\%$ de systèmes WR+cc. Or, uniquement un seul système WR+cc a été confirmé: Cygnus X-1. Pour comprendre la disparité des systèmes WR+cc par rapport aux WR+O, nous avons effectué une synthèse de population binaire. D'abord, nous avons generé une population synthétique de systèmes binaires massifs du type O+O ayant des propriétés orbitales qui reflètent l'échantillon Galactique. Ensuite, jumelé avec un code d'évolution binaire, nous avons évolué la population initiale de systèmes binaires dans le temps afin de comparer les prédictions théoriques des systèmes WR+cc aux systèmes WR+O et aux observations.

Mes contributions correspondent à l'application d'une synthèse de population à partir du code d'évolution binaire développé par Hurley et al. (2002). Guidé par Anthony Moffat, les co-auteurs Grant Hill, Noel Richardon et Herbert Pablo ont tous fourni des commentaires constructifs et fondamentaux à la rédaction de l'article. Enfin, l'article a été entièrement rédigé par moi-même. J'ai été choisie pour présenter le travail oralement.

L'article a été publié et se retrouve dans les actes de conférence du "International Workshop on Wolf-Rayet Stars" qui a eu lieu du 1er au 5 juin 2015 à Potsdam, Allemagne.

Munoz, M., Moffat, A. F. J., Hill, G. M., Richardson, N. D. and Pablo, H., (2015). The missing Wolf-Rayet X-ray binary systems. *Proceedings of an International Workshop held in Potsdam, Germany, 1.–5. June 2015: Pages 225-228.*
Version finale: `http://adsabs.harvard.edu/abs/2015wrs..conf..225M`.

The missing Wolf-Rayet X-ray binary systems.

Melissa Muñoz,[1] Anthony F. J. Moffat,[1] Hill M. Grant,[2] Noel D. Richardson,[1]
Herbert Pablo,[1]

[1]*Département de Physique, Université de Montréal, and Centre de Recherche en Astrophysique du Quebec, CP 6128, Succursale, Montréal, QC H3C 3J7, Canada*
[2]*W.M. Keck Observatory, 65-1120 Mamalohoa, Kamuela, HI 96743, USA*

Abstract

We investigate the rarity of the Wolf-Rayet X-ray binaries (WRXRBs) in contrast to their predecessors, the high mass X-ray binaries (HMXRBs). Recent studies suggest that common envelope (CE) mergers during the evolution of a HMXRBs may be responsible (Linden et al., 2012). We conduct a binary population synthesis to generate a population of HMXRBs mimicking the Galactic sample and vary the efficiency parameter during the CE phase to match the current WRXRB to HMXRB ratio. We find that ∼50% of systems must merge to match observational constraints.

4.1 Introduction

Current Wolf-Rayet (WR) evolution theories agree that WR stars originate from O-type main sequence stars. Thus, we expect a commonplace O+O binary system to evolve into an O+cc, a high mass x-ray binary, and eventually to a WR+cc system. Yet, while the number of known O + cc is significant, the number of detected WR+cc systems is much lower than predicted. In fact, while there are a total of 114 confirmed HMXRBs (Liu et al., 2006) in our Galaxy, there is only a single confirmed WR+cc binary: Cyg X-3 (Tutukov et al., 2013b).

To explain this discrepancy, the evolution of an HMXRB to a WRXRB is presumably halted by a CE merger. The goal is to produce a sufficient number of massive OB binaries to obtain 114 HMXRBs and adjust the efficiency parameter such that the merger rate of the HMXRBs is compatible with the observed number of WRXRBs.

4.2 Computational method

4.2.1 Initial binary population

Assuming zero eccentricity, the synthetic binaries can be synthesized with the aid of three probability distribution functions (PDFs): 1) the Salpeter initial mass function to determine the mass of the primary, m_1 2) empirical mass ratio to determine the mass of the secondary, m_2 3) Öpiks law to determine the orbital period, P. Respectively, the PDFs are:

$$\begin{aligned} f(m_1) &\propto m_1^{-2.35} \\ f(q) &\propto 1 \\ f(P) &\propto 1/P \end{aligned} \tag{4.1}$$

where $q = m_2/m_1$. The masses will range from 8 $M_\odot$, the minimum threshold for massive stars to undergo a supernova explosion, to 100 $M_\odot$, the maximum capacity in the binary evolution code (see section 4.2.2), and the period from 2 to 3000 days. Any system with a period less than 2 days is expected to merge and binary interaction is insignificant above 3000 days.

4.2.2 Binary Evolution

The generated binaries are evolved with a binary evolution code from Hurley et al. (2002). The initial masses and periods obtained in (1) will serve as input parameters. It is necessary to determine the distribution of supernova kicks and the efficiency parameter of the CE phase as they play an important role in the evolution of a HMXRB.

4.2.2.1 Supernova kicks

Asymmetric supernova (SN) explosions may impart an additional kick to a binary system. This may encourage the binary to disrupt or even help stabilize the orbit. Modelling SN kicks is therefore essential in massive binary evolution.

The direction of the kicks is presumed to be random. As for its magnitude, neutron star (NS) natal kicks are modeled with a Maxwellian distribution peaked at 300 km/s. Black hole (BH) kicks are assumed to obey reduced NS kicks owing to conservation of momentum (Repetto et al., 2012). For example, a 10 $M_\odot$ BH will receive $\sim$60% the kick of a 1.4 $M_\odot$ NS.

4.2.2.2 Common envelope evolution

If mass transfer occurs on dynamical timescales, faster than the compact object can accrete, then the excess matter will lead to the formation of a common envelope (CE) around both stars. As the compact companion orbits around the donor's core, the envelope creates a drag force on the two stars that dissipates their angular momentum and causes them to spiral in. The outcome of this scenario is either a successful ejection of the CE or a merger.

As the stars spiral in, if enough gravitational energy is released and converted to kinetic energy into the envelope, the CE may be blown away. However, as there are non-conservative forces, some energy will be lost. The survivability of the system depends on its efficiency in transferring orbital energy into the envelope.

Treatment of the CE evolution in Hurley et al. (2002) introduces two free parameters: α_{CE}, the efficiency, and λ, a corrective term in the envelope's binding energy that depends the donor's mass-density structure. It is common practice to set λ at 0.5 (de Kool, 1990) and the efficiency typically varies from 0 to 1. Therefore, in this study, λ is left constant at this default value and only α_{CE} was varied.

4.3 Results

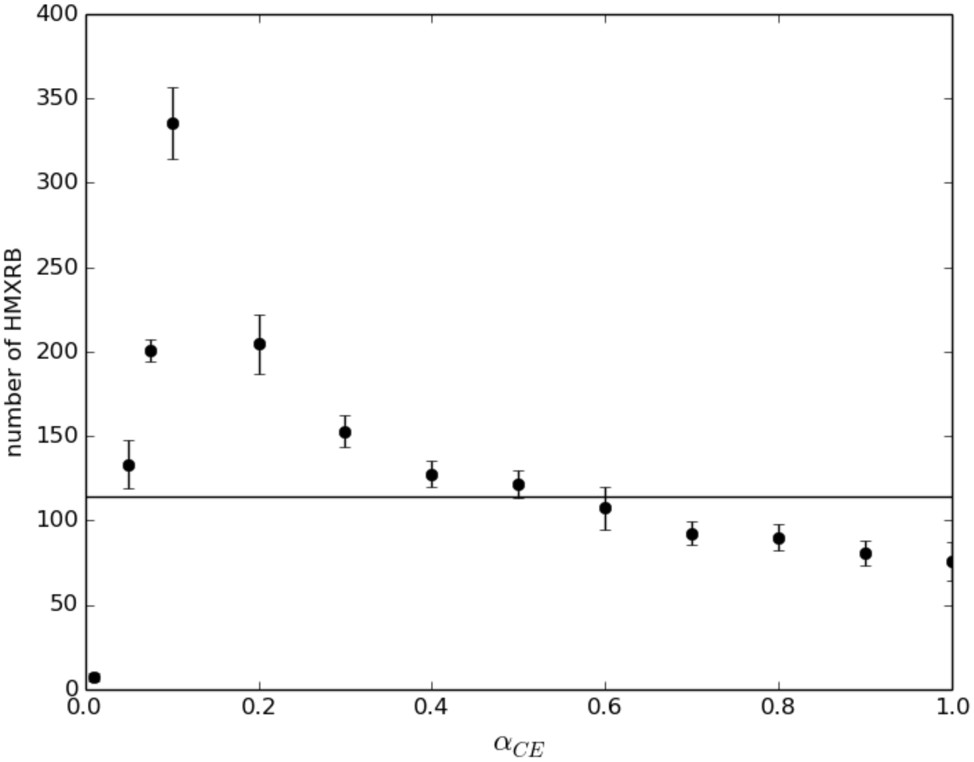

Figure 4.1: Number of HMXRBs as a function of the efficiency. The number of initial synthetic binaries is kept constant at 12000. The solid horizontal line indicates the cut off for 114 HMXRBs.

In Figure 4.1 we illustrate how the efficiency parameter effects the number of resulting HMXRBs with a constant initial population of 12000 binaries. The efficiency ranged from 0 to 1 with an increment of 0.1.

Similarly, depicted in Figure 4.2 is the number of WRXRB for a given efficiency.

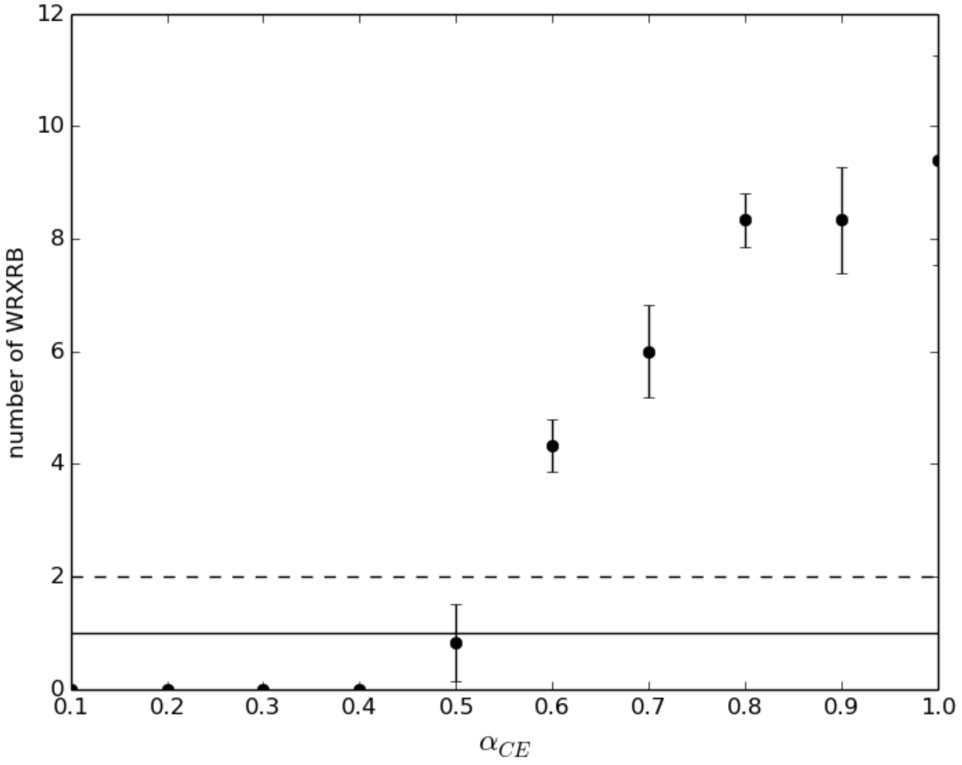

Figure 4.2: Number of WRXRBs as a function of the efficiency. The number of initial synthetic binaries is adjusted to produce roughly 114 HMXRBs. The solid and dashed horizontal lines respectively correspond to the thresholds for 1 WRXRB (Cyg X-3) and 2 WRXRBs (Cyg X-3 and possibly another unidentified WRXRB, such as WR 148).

For each value of α_{CE}, the initial population of generated OB binaries is calibrated (by trial and error) to ensure that there are $\sim$114 HMXRBs.

4.4 Discussion

Of interest is the value of α_{CE} to require all but a single HMXRB to merge from an initial sample of 114 HMXRBs. However, obtaining a constant population of 114 HMXRBs is difficult because it is sensitive to the efficiency. This indicates that there may be a CE phase prior to the SN of the original primary. If this were the case, then intuitively one would expect the number of HMXRBs to decrease as the efficiency drops.

And yet, as seen in Figure 1, the number of HMXRBs appear to rise for α_{CE} decreasing to 0.1.

A CE phase, while both stars are still on the main sequence, has an unprecedented effect on the disruption rate of a binary subsequent to a SN. As the efficiency drops, the pre-SN binaries that survive a CE phase (if a CE phase occurs) will have a much reduced orbital separation. As a result, these tighter binaries will have a better chance of surviving the first SN, thus creating more HMXRBs. This is valid for an efficiency between 0.1 and 1. However, below $\alpha_{\text{CE}} = 0.1$, the energy conversion isn't efficient enough for the binaries to survive the pre-SN CE phase and so the number of HMXRBs decline rapidly.

The surviving HMXRBs face another hurdle. Their evolution and fate is often subject to a CE phase once again. This is because unstable mass transfer is easily triggered if the binary components have a large mass ratio (e.i. $q1$). This is most likely the case for puffy OB stars orbiting around a compact object. Binaries that are successful at ejecting their CE can have their orbital separations drastically reduced by up to a factor of 100 (Tauris & van den Heuvel, 2006b). This can explain Cyg X-3's extremely short period of 4.8 hours.

Considering the typical lifetimes of a WR compared to its O-star progenitors, we would expect around 10% of the HMXRBs to evolve into WRXRBs. Thus naively, if there were no CE mergers, we would predict ~11 WRXRB in the Galaxy. This is what is shown in Figure 2 at 100 % efficiency (within error). As suspected, the number of WRXRBs decreases along with the efficiency. Below 40% efficiency, all HMXRBs have merged and there are no WRXRBs. Setting α_{CE} to 0.5 allows us to obtain the ideal merger rate.

These results are valid in the assumption that $\lambda = 0.5$. However, the true determination of this coefficient is still subject to much debate. Nevertheless, we are fortunate that the CE evolution depends on the product $\alpha_{\text{CE}}\lambda$ and not on the individual values themselves. Therefore, if λ is ever better constrained, the validity of this work is not changed as long as α_{CE} is adjusted so that the quantity $\alpha_{\text{CE}}\lambda$ remains equal to 0.25.

4.5 Conclusion and future work

We demonstrated how the transition from HMXRB to WRXRB can be impeded due to unstable mass transfer which leads to the formation of a common envelope. The apparent lack of WRXRB in comparison to the number of HMXRB can hence be explained by CE mergers. We obtain an efficieny of 0.5 during the CE phase to reproduce the current WRXRB to HMXRB ratio.

It is important to note that this study relies on the premise that Cyg X-3 is the only WRXRB in our galaxy. There are however other candidates worthy of investigation, namely WR 148 (HD 197406). WR 148 is a single lined spectroscopic binary classified as a WN8h + B3IV/BH (Hamann et al., 2006a). To determine the nature of the companion we have obtained high signal to noise spectra (above 1000 per pixel in the continuum once combined) from the Keck observatory with the ESI spectrograph, providing a range of 3900 Å to 10900 Å. A meticulous study of these spectra is currently underway.

Fin de l'article.

CHAPTER 5

CONCLUSION

Ce projet de mémoire était en premier lieu motivé par la recherche des rares systèmes WR+cc, débutant par l'étude de deux cas extrêmes des étoiles Wolf-Rayets en cavales: WR 148 et WR 71. Soupçonnés d'être éjectés par le recul d'une explosion supernova, des systèmes binaires en cavales du type SB1 comptant une étoile WR sont donc considérés des bons candidats des systèmes WR+cc.

WR 148 est un système binaire spectroscopique confirmé dont la nature du compagnon est inconnue. Par souci que les puissantes raies d'émission de l'étoile WR masquent les raies d'un compagnon non compact, nous avons obtenu deux nuits de spectres à haute résolution et rapport signal sur bruit élevé à l'Observatoire Keck. Ceci révèle des faibles raies d'absorption se déplaçant en antiphase avec les raies de la WR qu'on suspecte viennent du compagnon. À l'aide des données prises à l'Observatoire du Mont-Mégantic, nous avons séparé les deux spectres et classifié le compagnon comme un O5. Conformément à ce résultat, les variations photométriques et polarimétriques se comportent de manière typique pour un système WR+O serré. Nous nous attendons donc à observer des évidences de collisions de vents. En effet, WR 148 manifeste des rayons X thermiques ainsi qu'un excès d'émission périodique de l'étoile WR.

En revanche, WR 71 n'est qu'un système binaire soupçonné. Nous avons donc obtenu de multiples spectres pour vérifier son statut de binarité. Bien que les spectres soient fort variables, aucune variation de vitesses radiales cohérentes (attendues pour des systèmes binaires) n'a été détectée. Sous la supposition que WR 71 est en fait une étoile simple, nous avons analysé une courbe de lumière obtenue par le micro-satellite MOST. Des périodes dominantes de 1.7 et 3.4 jours ont été détectées dans la première et deuxième moitié de la courbe lumière, respectivement. On suggère que ce changement brusque dans la courbe de lumière peut être dû à un changement de configuration de taches brillantes qui sont à la source des CIRs. Il est donc possible que les variations spectroscopiques et photométriques intrinsèques à l'étoile soient liées aux CIRs.

Étant des étoiles en cavales, les cas présentés constituent des opportunités uniques pour explorer la cinématique et le mouvement des étoiles sujettes à un potentiel Galactique. Étudier les trajectoires balistiques de WR 148 et WR 71 nous renseigne sur leur vitesse d'éjection initiale et leur durée de vie minimale. Ces informations sont instructives pour discriminer entre les différents mécanismes d'éjections responsables de leur extrême emplacement géométrique. Il s'avère que les deux étoiles possèdent des vitesses particulières trop élevées pour être éjectées via des explosions supernovas. Cela favorise les interactions dynamiques dans un amas stellaire jeune comme méthode d'éjection.

Suite à la confirmation de la nature non compacte des étoiles WR 148 et WR 71, nous nous sommes interrogé au sujet de la rareté des systèmes WR+cc par rapport au nombre de systèmes O+cc connus. Nous avons développé une synthèse de population binaire adaptée aux étoiles massives dans l'intérêt de comparer le rapport WR+cc/O+cc prédit par les simulations aux observations. Pour réconcilier les statistiques observationnelles aux prédictions théoriques, on propose que la phase d'enveloppe commune interrompe l'évolution des systèmes O+cc vers les WR+cc. En effet, la résistance du gaz dans l'enveloppe commune favorise la coalescence des deux membres du système.

BIBLIOGRAPHY

I. Antokhin, J.-F. Bertrand, R. Lamontagne & A. F. J. Moffat. A unique period for the WN5 star EZ CMa. *Astron. J.*, 107:2179–2183, juin 1994.

I. Antokhin, J.-F. Bertrand, R. Lamontagne, A. F. J. Moffat & J. Matthews. The enigmatic WN8 stars: Intensive photometry of four southern stars on time scales from 30 min to 3 months. *Astron. J.*, 109:817–834, février 1995.

I. I. Antokhin. New Photoelectric Observations of Wolf-Rayet Star HD197406 with Probable Relativistic Companion = V1696-CYGNI. *Astronomicheskij Tsirkulyar*, 1350:1, novembre 1984.

I. I. Antokhin, A. A. Aslanov & A. M. Cherepashchuk. HD 191765 - A Wolf-Rayet binary with a low-mass companion. *Soviet Astronomy Letters*, 8:290–296, juin 1982.

L. A. Balona, J. Egan & F. Marang. Intensive photometry of southern Wolf-Rayet stars. *Mon. Not. Roy. Astron. Soc.*, 240:103–115, septembre 1989.

P. Bartzakos, A. F. J. Moffat & V. S. Niemela. Magellanic Cloud WC/WO Wolf-Rayet stars - II. Colliding winds in binaries. *Mon. Not. Roy. Astron. Soc.*, 324:33–50, juin 2001.

P. Bastien, L. Drissen, F. Menard, A. F. J. Moffat, C. Robert & N. St-Louis. The variability of polarized standard stars. *Astron. J.*, 95:900–910, mars 1988.

J. Binney & S. Tremaine. *Galactic dynamics*. 1987.

A. Blaauw. On the origin of the O- and B-type stars with high velocities (the ”run-away” stars), and some related problems. , 15:265, mai 1961.

J.-C. Bouret, D. J. Hillier, T. Lanz & A. W. Fullerton. Properties of Galactic early-type O-supergiants. A combined FUV-UV and optical analysis. *Astron. Astrophys.*, 544: A67, août 2012.

K. Bracher. The Wolf-Rayet spectroscopic binary HD 197406. *Publ. Astron. Soc. Pac.*, 91:827–829, décembre 1979.

J. C. Brown, I. S. McLean & A. G. Emslie. Polarisation by Thomson scattering in optically thin stellar envelopes. II - Binary and multiple star envelopes and the determination of binary inclinations. *Astron. Astrophys.*, 68:415–427, août 1978.

E. Budding. *Introduction to Astronomical Photometry*. septembre 1993.

J. I. Castor, D. C. Abbott & R. I. Klein. Radiation-driven winds in Of stars. *Astrophys. J.*, 195:157–174, janvier 1975.

A.-N. Chené, A. F. J. Moffat, C. Cameron, R. Fahed, R. C. Gamen, L. Lefèvre, J. F. Rowe, N. St-louis, V. Muntean, A. De La Chevrotière, D. B. Guenther, R. Kuschnig, J. M. Matthews, S. M. Rucinski, D. Sasselov & W. W. Weiss. WR 110: A Single Wolf-Rayet Star with Corotating Interaction Regions in its Wind? *Astrophys. J.*, 735: 34, juillet 2011.

A.-N. Chené & N. St-Louis. Large-scale Periodic Variability of the Wind of the Wolf-Rayet Star WR 1 (HD 4004). *Astrophys. J.*, 716:929–941, juin 2010.

A.-N. Chené & N. St-Louis. A Systematic Search for Corotating Interaction Regions in Apparently Single Galactic Wolf-Rayet Stars. II. A Global View of the Wind Variability. *Astrophys. J.*, 736:140, août 2011.

P. S. Conti, P. A. Crowther & C. Leitherer. *From Luminous Hot Stars to Starburst Galaxies*. Cambridge University Press, octobre 2008.

P. S. Conti & S. A. Frost. Spectroscopic studies of O-type stars. VI - The earliest types: O3-O5.5. *Astrophys. J.*, 212:728–742, mars 1977.

S. R. Cranmer & S. P. Owocki. Hydrodynamical Simulations of Corotating Interaction Regions and Discrete Absorption Components in Rotating O-Star Winds. *Astrophys. J.*, 462:469, mai 1996a.

S. R. Cranmer & S. P. Owocki. Hydrodynamical Simulations of Corotating Interaction Regions and Discrete Absorption Components in Rotating O-Star Winds. *Astrophys. J.*, 462:469, mai 1996b.

P. A. Crowther. Physical Properties of Wolf-Rayet Stars. , 45:177–219, septembre 2007.

P. A. Crowther. Physical and Wind Properties of [WC] Stars. Dans A. Werner & T. Rauch, éditeurs, *Hydrogen-Deficient Stars*, volume 391 de *Astronomical Society of the Pacific Conference Series*, page 83, juillet 2008.

M. de Kool. Common envelope evolution and double cores of planetary nebulae. *Astrophys. J.*, 358:189–195, juillet 1990.

W. Dehnen & J. J. Binney. Local stellar kinematics from HIPPARCOS data. *Mon. Not. Roy. Astron. Soc.*, 298:387–394, août 1998.

L. M. Dray, J. E. Dale, M. E. Beer, R. Napiwotzki & A. R. King. Wolf-Rayet and O star runaway populations from supernovae. *Mon. Not. Roy. Astron. Soc.*, 364:59–68, novembre 2005.

L. Drissen, R. Lamontagne, A. F. J. Moffat, P. Bastien & M. Seguin. Spectroscopic and polarimetric parameters of the runaway WN7 binary system HD 197406 - Is the secondary an X-ray-quiet black hole? *Astrophys. J.*, 304:188–200, mai 1986.

J. J. Eldridge, N. Langer & C. A. Tout. Runaway stars as progenitors of supernovae and gamma-ray bursts. *Mon. Not. Roy. Astron. Soc.*, 414:3501–3520, juillet 2011.

R. Fahed & A. F. J. Moffat. Colliding winds in five WR+O systems of the Southern hemisphere. *Mon. Not. Roy. Astron. Soc.*, 424:1601–1613, août 2012.

J. M. Fregeau, F. A. Rasio, P. Cheung & S. F. Portegies Zwart. Stellar Collisions During Binary Interactions and the Effect on Runaway Collisions. Dans N. St.-Louis & A. F. J. Moffat, éditeurs, *Massive Stars in Interactive Binaries*, volume 367 de *Astronomical Society of the Pacific Conference Series*, page 715, 2007.

D. B. Friend & D. C. Abbott. The theory of radiatively driven stellar winds. III - Wind models with finite disk correction and rotation. *Astrophys. J.*, 311:701–707, décembre 1986.

A. W. Fullerton, D. L. Massa & R. K. Prinja. The Discordance of Mass-Loss Estimates for Galactic O-Type Stars. *Astrophys. J.*, 637:1025–1039, février 2006.

K. G. Gayley & S. P. Owocki. Line-driven Instability Growth Rates in Wolf-Rayet Winds. *Astrophys. J.*, 446:801, juin 1995.

K. G. Gayley, S. P. Owocki & S. R. Cranmer. Sudden Radiative Braking in Colliding Hot-Star Winds. *Astrophys. J.*, 475:786–797, février 1997.

J. F. González & H. Levato. Separation of composite spectra: the spectroscopic detection of an eclipsing binary star. *Astron. Astrophys.*, 448:283–292, mars 2006.

G. Gräfener, L. Koesterke & W.-R. Hamann. Line-blanketed model atmospheres for WR stars. *Astron. Astrophys.*, 387:244–257, mai 2002.

D. F. Gray. Atmospheric turbulence measured in stars above the main sequence. *Astrophys. J.*, 202:148–164, novembre 1975.

Y. Grosdidier, A. F. J. Moffat, G. Joncas & A. Acker. HST WFPC2/Hα Imagery of the Nebula M1-67: A Clumpy LBV Wind Imprinting Itself on the Nebular Structure? *Astrophys. J. Lett.*, 506:L127–L131, octobre 1998.

V. V. Gvaramadze & A. Gualandris. Very massive runaway stars from three-body encounters. *Mon. Not. Roy. Astron. Soc.*, 410:304–312, janvier 2011.

W.-R. Hamann & G. Gräfener. Grids of model spectra for WN stars, ready for use. *Astron. Astrophys.*, 427:697–704, novembre 2004.

W.-R. Hamann, G. Gräfener & A. Liermann. The Galactic WN stars. Spectral analyses with line-blanketed model atmospheres versus stellar evolution models with and without rotation. *Astron. Astrophys.*, 457:1015–1031, octobre 2006a.

W.-R. Hamann, G. Gräfener & A. Liermann. The Galactic WN stars. Spectral analyses with line-blanketed model atmospheres versus stellar evolution models with and without rotation. *Astron. Astrophys.*, 457:1015–1031, octobre 2006b.

W.-R. Hamann, G. Gräfener & A. Liermann. The Galactic WN stars. Spectral analyses with line-blanketed model atmospheres versus stellar evolution models with and without rotation. *Astron. Astrophys.*, 457:1015–1031, octobre 2006c.

G. H. Herbig. The Diffuse Interstellar Bands. , 33:19–74, 1995.

G. M. Hill, A. F. J. Moffat & N. St-Louis. Modelling the colliding-winds spectra of the 19-d WR + OB binary in the massive triple system Muscae. *Mon. Not. Roy. Astron. Soc.*, 335:1069–1078, octobre 2002.

G. M. Hill, A. F. J. Moffat, N. St-Louis & P. Bartzakos. Modelling the spectra of colliding winds in the Wolf-Rayet WC7+O binaries WR 42 and WR 79. *Mon. Not. Roy. Astron. Soc.*, 318:402–410, octobre 2000.

D. J. Hillier. The effects of electron scattering and wind clumping for early emission line stars. *Astron. Astrophys.*, 247:455–468, juillet 1991.

D. Hoffleit. Stellar Spectra. (Scientific Books: An Atlas of Stellar Spectra with an Outline of Spectral Classification). *Science*, 97:536–537, juin 1943.

R. Hoogerwerf, J. H. J. de Bruijne & P. T. de Zeeuw. On the origin of the O and B-type stars with high velocities. II. Runaway stars and pulsars ejected from the nearby young stellar groups. *Astron. Astrophys.*, 365:49–77, janvier 2001.

I. D. Howarth & R. K. Prinja. The stellar winds of 203 Galactic O stars - A quantitative ultraviolet survey. , 69:527–592, mars 1989.

J. R. Hurley, C. A. Tout & O. R. Pols. Evolution of binary stars and the effect of tides on binary populations. *Mon. Not. Roy. Astron. Soc.*, 329:897–928, février 2002.

A. Irrgang, B. Wilcox, E. Tucker & L. Schiefelbein. Milky Way mass models for orbit calculations. *Astron. Astrophys.*, 549:A137, janvier 2013.

J. Isserstedt, A. F. J. Moffat & V. S. Niemela. The runaway Wolf-Rayet star HD 143414 - Evidence for a low-mass companion. *Astron. Astrophys.*, 126:183–191, septembre 1983.

K. Karami & R. Mohebi. Velocity curve analysis of the spectroscopic binary stars PV Pup, HD 141929, EE Cet and V921 Her by nonlinear regression. *Journal of Astrophysics and Astronomy*, 28:217–230, avril 2008.

H. J. G. L. M. Lamers & J. P. Cassinelli. *Introduction to Stellar Winds*. juin 1999.

H. J. G. L. M. Lamers & C. Leitherer. What are the mass-loss rates of O stars? *Astrophys. J.*, 412:771–791, août 1993.

R. Lamontagne, A. F. J. Moffat, L. Drissen, C. Robert & J. M. Matthews. Photometric Determination of Orbital Inclinations and Mass Loss Rates for Wolf-Rayet Stars in WR+O Binaries. *Astron. J.*, 112:2227, novembre 1996.

L. Lefèvre, S. V. Marchenko, A. F. J. Moffat, A. N. Chené, S. R. Smith, N. St-Louis, J. M. Matthews, R. Kuschnig, D. B. Guenther, C. A. Poteet, S. M. Rucinski, D. Sasselov, G. A. H. Walker & W. W. Weiss. Oscillations in the Massive Wolf-Rayet Star WR 123 with the MOST Satellite. *Astrophys. J. Lett.*, 634:L109–L112, novembre 2005.

P. J. T. Leonard. Mechanisms for Ejecting Stars from the Galactic Plane. Dans D. D. Sasselov, éditeur, *Luminous High-Latitude Stars*, volume 45 de *Astronomical Society of the Pacific Conference Series*, page 360, janvier 1993.

P. J. T. Leonard & R. J. Dewey. Montecarlo Simulations of the Supernova Ejection Mechanism for the Runaway Stars. Dans D. D. Sasselov, éditeur, *Luminous High-Latitude Stars*, volume 45 de *Astronomical Society of the Pacific Conference Series*, page 239, janvier 1993.

P. J. T. Leonard & M. J. Duncan. Runaway stars from young star clusters containing initial binaries. II - A mass spectrum and a binary energy spectrum. *Astron. J.*, 99: 608–616, février 1990a.

P. J. T. Leonard & M. J. Duncan. Runaway stars from young star clusters containing initial binaries. II - A mass spectrum and a binary energy spectrum. *Astron. J.*, 99: 608–616, février 1990b.

S. Lépine & A. F. J. Moffat. Wind Inhomogeneities in Wolf-Rayet Stars. II. Investigation of Emission-Line Profile Variations. *Astrophys. J.*, 514:909–931, avril 1999a.

S. Lépine & A. F. J. Moffat. Wind Inhomogeneities in Wolf-Rayet Stars. II. Investigation of Emission-Line Profile Variations. *Astrophys. J.*, 514:909–931, avril 1999b.

S. Lépine & A. F. J. Moffat. Wind Inhomogeneities in Wolf-Rayet Stars. II. Investigation of Emission-Line Profile Variations. *Astrophys. J.*, 514:909–931, avril 1999c.

S. Lépine & A. F. J. Moffat. Direct Spectroscopic Observations of Clumping in O-Star Winds. *Astron. J.*, 136:548–553, août 2008.

T. Linden, F. Valsecchi & V. Kalogera. On the Rarity of X-Ray Binaries with Naked Helium Donors. *Astrophys. J.*, 748:114, avril 2012.

Q. Z. Liu, J. van Paradijs & E. P. J. van den Heuvel. Catalogue of high-mass X-ray binaries in the Galaxy (4th edition). *Astron. Astrophys.*, 455:1165–1168, septembre 2006.

J. R. Lomax, Y. Nazé, J. L. Hoffman, C. M. P. Russell, M. De Becker, M. F. Corcoran, J. W. Davidson, H. R. Neilson, S. Owocki, J. M. Pittard & A. M. T. Pollock. V444 Cygni X-ray and polarimetric variability: Radiative and Coriolis forces shape the wind collision region. *Astron. Astrophys.*, 573:A43, janvier 2015.

S. Luehrs. A Colliding-Wind Model for the Wolf-Rayet System HD 152270. *Publ. Astron. Soc. Pac.*, 109:504–513, mai 1997.

A. Maeder & G. Meynet. New models of Wolf-Rayet stars and comparison with data in galaxies. *Astron. Astrophys.*, 287, juillet 1994.

S. V. Marchenko, A. F. J. Moffat & P. R. J. Eenens. The Wolf-Rayet Binary WR 141 (WN5O + O5 V-III) Revisited. *Publ. Astron. Soc. Pac.*, 110:1416–1422, décembre 1998a.

S. V. Marchenko, A. F. J. Moffat, P. R. J. Eenens, O. Cardona, J. Echevarria & Y. Hervieux. The Wolf-Rayet Binary V444 Cygni Under the Spectroscopic Microscope. II. Physical Parameters of the Wolf-Rayet Wind and the Zone of Wind Collision. *Astrophys. J.*, 485:826–838, août 1997.

S. V. Marchenko, A. F. J. Moffat, P. R. J. Eenens, G. M. Hill & A. Grandchamps. Wind-Wind Interaction in the Close Wolf-Rayet Binary CQ Cephei (WN6+O9 II–Ib). *Astrophys. J.*, 450:811, septembre 1995.

S. V. Marchenko, A. F. J. Moffat, T. Eversberg, T. Morel, G. M. Hill, G. H. Tovmassian & W. Seggewiss. A comprehensive variability study of the enigmatic WN8 stars - Final results. *Mon. Not. Roy. Astron. Soc.*, 294:642, mars 1998b.

S. V. Marchenko, A. F. J. Moffat & G. Koenigsberger. The Wolf-Rayet binary V444 Cygni under the spectroscopic microscope. 1: Improved characteristics of the components and their interaction seen in He I. *Astrophys. J.*, 422:810–822, février 1994.

S. V. Marchenko, A. F. J. Moffat, R. Lamontagne & G. H. Tovmassian. The Wolf-Rayet Star HD 197406, with Its Strongly Ionizing Close Companion. *Astrophys. J.*, 461: 386, avril 1996.

S. V. Marchenko, A. F. J. Moffat, K. A. van der Hucht, W. Seggewiss, H. Schrijver, B. Stenholm, I. Lundstrom, D. Y. A. Setia Gunawan, W. Sutantyo, E. P. J. van den Heuvel, J.-P. de Cuyper & A. E. Gomez. Wolf-Rayet stars and O-star runaways with HIPPARCOS. II. Photometry. *Astron. Astrophys.*, 331:1022–1036, mars 1998c.

N. Markova & J. Puls. Bright OB stars in the Galaxy. IV. Stellar and wind parameters of early to late B supergiants. *Astron. Astrophys.*, 478:823–842, février 2008.

F. Martins, D. Schaerer & D. J. Hillier. A new calibration of stellar parameters of Galactic O stars. *Astron. Astrophys.*, 436:1049–1065, juin 2005a.

F. Martins, D. Schaerer & D. J. Hillier. A new calibration of stellar parameters of Galactic O stars. *Astron. Astrophys.*, 436:1049–1065, juin 2005b.

G. Mathys. The upper main sequence of OB associations. I - Spectral types and lines of C and N of southern single-lined O stars. *Astron. Astrophys. Suppl.*, 76:427–444, décembre 1988.

A. M. Mel'Nik & A. K. Dambis. Kinematics of OB-associations and the new reduction of the Hipparcos data. *Mon. Not. Roy. Astron. Soc.*, 400:518–523, novembre 2009.

G. Meynet & A. Maeder. Stellar evolution with rotation. X. Wolf-Rayet star populations at solar metallicity. *Astron. Astrophys.*, 404:975–990, juin 2003.

E. Michaely & H. B. Perets. Secular Dynamics in Hierarchical Three-body Systems with Mass Loss and Mass Transfer. *Astrophys. J.*, 794:122, octobre 2014.

Y. J. L. Michaux, A. F. J. Moffat, A.-N. Chené & N. St-Louis. On the origin of variable structures in the winds of hot luminous stars. *Mon. Not. Roy. Astron. Soc.*, 440:2–9, mai 2014.

B. Miszalski, P. A. Crowther, O. De Marco, J. Köppen, A. F. J. Moffat, A. Acker & T. C. Hillwig. IC 4663: the first unambiguous [WN] Wolf-Rayet central star of a planetary nebula. *Mon. Not. Roy. Astron. Soc.*, 423:934–947, juin 2012.

A. F. J. Moffat, L. Drissen, R. Lamontagne & C. Robert. Spectroscopic evidence for rapid blob ejection in Wolf-Rayet stars. *Astrophys. J.*, 334:1038–1043, novembre 1988.

A. F. J. Moffat, R. Lamontagne & W. Seggewiss. The fastest runaway Wolf-Rayet star of Population I in the Galaxy, 209 BAC - Evidence for a low mass companion. *Astron. Astrophys.*, 114:135–146, octobre 1982.

A. F. J. Moffat, S. V. Marchenko, W. Seggewiss, K. A. van der Hucht, H. Schrijver, B. Stenholm, I. Lundstrom, D. Y. A. Setia Gunawan, W. Sutantyo, E. P. J. van den

Heuvel, J.-P. de Cuyper & A. E. Gomez. Wolf-Rayet stars and O-star runaways with HIPPARCOS. I. Kinematics. *Astron. Astrophys.*, 331:949–958, mars 1998.

A. F. J. Moffat & W. Seggewiss. The intrinsically bright Wolf-Rayet stars of type WN7. IV - The galactic WN7/WN8 stars as massive O-stars in advanced stages of evolution. *Astron. Astrophys.*, 77:128–140, août 1979.

A. F. J. Moffat & M. M. Shara. Photometric variability of a complete sample of northern Wolf-Rayet stars. *Astron. J.*, 92:952–975, octobre 1986.

C. L. Morbey & E. B. Brosterhus. A Search for Spectroscopic Binaries from Published Radial Velocity Data. *Publ. Astron. Soc. Pac.*, 86:455, août 1974.

T. Morel, S. V. Marchenko, P. R. J. Eenens, A. F. J. Moffat, G. Koenigsberger, I. I. Antokhin, T. Eversberg, G. H. Tovmassian, G. M. Hill, O. Cardona & N. St-Louis. A 2.3 Day Periodic Variability in the Apparently Single Wolf-Rayet Star WR 134: Collapsed Companion or Rotational Modulation? *Astrophys. J.*, 518:428–441, juin 1999.

T. Morel, N. St-Louis & S. V. Marchenko. Optical Spectroscopy of EZ Canis Majoris: Indication for Large-Scale Structures in a Wolf-Rayet Wind. *Astrophys. J.*, 482:470–489, juin 1997.

D. J. Mullan. Corotating interaction regions in stellar winds. *Astrophys. J.*, 283:303–312, août 1984.

S. Naoz, W. M. Farr, Y. Lithwick, F. A. Rasio & J. Teyssandier. Secular dynamics in hierarchical three-body systems. *Mon. Not. Roy. Astron. Soc.*, 431:2155–2171, mai 2013.

G. Nelemans. What Can We Learn About Black-Hole Formation from Black-Hole X-ray Binaries? Dans N. St.-Louis & A. F. J. Moffat, éditeurs, *Massive Stars in Interactive Binaries*, volume 367 de *Astronomical Society of the Pacific Conference Series*, page 533, 2007.

Matthew Newville, Till Stensitzki, Daniel B. Allen & Antonino Ingargiola. LMFIT: Non-Linear Least-Square Minimization and Curve-Fitting for Python¶, septembre 2014. URL `http://dx.doi.org/10.5281/zenodo.11813`.

A. Pauldrach, J. Puls & R. P. Kudritzki. Radiation-driven winds of hot luminous stars - Improvements of the theory and first results. *Astron. Astrophys.*, 164:86–100, août 1986.

H. B. Perets & L. Šubr. The Properties of Dynamically Ejected Runaway and Hyper-runaway Stars. *Astrophys. J.*, 751:133, juin 2012.

P. Petit, T. Louge, S. Théado, F. Paletou, N. Manset, J. Morin, S. C. Marsden & S. V. Jeffers. PolarBase: A Database of High-Resolution Spectropolarimetric Stellar Observations. *Publ. Astron. Soc. Pac.*, 126:469–475, mai 2014.

S. F. Portegies Zwart. The Characteristics of High-Velocity O and B Stars Which Are Ejected from Supernovae in Binary Systems. *Astrophys. J.*, 544:437–442, novembre 2000.

K. A. Postnov & L. R. Yungelson. The Evolution of Compact Binary Star Systems. *Living Reviews in Relativity*, 17, mai 2014a.

K. A. Postnov & L. R. Yungelson. The Evolution of Compact Binary Star Systems. *Living Reviews in Relativity*, 17, mai 2014b.

A. Poveda, J. Ruiz & C. Allen. Run-away Stars as the Result of the Gravitational Collapse of Proto-stellar Clusters. *Boletin de los Observatorios Tonantzintla y Tacubaya*, 4:86–90, avril 1967.

R. K. Prinja, M. J. Barlow & I. D. Howarth. Terminal velocities for a large sample of O stars, B supergiants, and Wolf-Rayet stars. *Astrophys. J.*, 361:607–620, octobre 1990.

J. Puls, R.-P. Kudritzki, A. Herrero, A. W. A. Pauldrach, S. M. Haser, D. J. Lennon, R. Gabler, S. A. Voels, J. M. Vilchez, S. Wachter & A. Feldmeier. O-star mass-loss and wind momentum rates in the Galaxy and the Magellanic Clouds Observations and theoretical predictions. *Astron. Astrophys.*, 305:171, janvier 1996.

J. Puls, J. S. Vink & F. Najarro. Mass loss from hot massive stars. *Astron. Astrophys. Rev.*, 16:209–325, décembre 2008.

S. Repetto, M. B. Davies & S. Sigurdsson. Investigating stellar-mass black hole kicks. *Mon. Not. Roy. Astron. Soc.*, 425:2799–2809, octobre 2012.

C. Robert, A. F. J. Moffat, P. Bastien, L. Drissen & N. St.-Louis. Polarization variability among Wolf-Rayet stars. V - Linear polarization of the bright Cygnus stars and an anticorrelation of variability with wind speed. *Astrophys. J.*, 347:1034–1054, décembre 1989.

C. K. Rosslowe & P. A. Crowther. Spatial distribution of Galactic Wolf-Rayet stars and implications for the global population. *Mon. Not. Roy. Astron. Soc.*, 447:2322–2347, mars 2015.

J. F. Rowe, J. M. Matthews, S. Seager, R. Kuschnig, D. B. Guenther, A. F. J. Moffat, S. M. Rucinski, D. Sasselov, G. A. H. Walker & W. W. Weiss. An Upper Limit on the Albedo of HD 209458b: Direct Imaging Photometry with the MOST Satellite. *Astrophys. J.*, 646:1241–1251, août 2006.

J. F. Rowe, J. M. Matthews, S. Seager, E. Miller-Ricci, D. Sasselov, R. Kuschnig, D. B. Guenther, A. F. J. Moffat, S. M. Rucinski, G. A. H. Walker & W. W. Weiss. The Very Low Albedo of an Extrasolar Planet: MOST Space-based Photometry of HD 209458. *Astrophys. J.*, 689:1345–1353, décembre 2008.

J. D. Scargle. Studies in astronomical time series analysis. II - Statistical aspects of spectral analysis of unevenly spaced data. *Astrophys. J.*, 263:835–853, décembre 1982.

M. M. Shara, S. M. Crawford, D. Vanbeveren, A. F. J. Moffat, D. Zurek & L. Crause. The spin rates of O stars in WR + O binaries. I. Motivation, methodology and first results from SALT. *ArXiv e-prints*, octobre 2015.

T. Shenar, W.-R. Hamann & H. Todt. The impact of rotation on the line profiles of Wolf-Rayet stars. *Astron. Astrophys.*, 562:A118, février 2014a.

T. Shenar, W.-R. Hamann & H. Todt. The impact of rotation on the line profiles of Wolf-Rayet stars. *Astron. Astrophys.*, 562:A118, février 2014b.

T. Shenar, L. Oskinova, W.-R. Hamann, M. F. Corcoran, A. F. J. Moffat, H. Pablo, N. D. Richardson, W. L. Waldron, D. P. Huenemoerder, J. Maíz Apellániz, J. S. Nichols, H. Todt, Y. Nazé, J. L. Hoffman, A. M. T. Pollock & I. Negueruela. A Coordinated X-Ray and Optical Campaign of the Nearest Massive Eclipsing Binary, δ Orionis Aa. IV. A Multiwavelength, Non-LTE Spectroscopic Analysis. *Astrophys. J.*, 809:135, août 2015.

S. Simón-Díaz & A. Herrero. The IACOB project. I. Rotational velocities in northern Galactic O- and early B-type stars revisited. The impact of other sources of line-broadening. *Astron. Astrophys.*, 562:A135, février 2014.

W. M. Smart & E. b. R. M. Green. *Textbook on Spherical Astronomy*. juillet 1977.

L. F. Smith, M. M. Shara & A. F. J. Moffat. A three-dimensional classification for WN stars. *Mon. Not. Roy. Astron. Soc.*, 281:163–191, juillet 1996.

L. J. Smith, C. Lloyd & E. N. Walker. UV and optical observations of variability in the WR+ compact candidate HD 96548. *Astron. Astrophys.*, 146:307–316, mai 1985.

V. V. Sobolev. *Moving envelopes of stars*. 1960.

N. St.-Louis, A. F. J. Moffat, L. Drissen, P. Bastien & C. Robert. Polarization variability among Wolf-Rayet stars. III - A new way to derive mass-loss rates for Wolf-Rayet stars in binary systems. *Astrophys. J.*, 330:286–304, juillet 1988.

J. E. Steiner & M. P. Diaz. The V Sagittae Stars. *Publ. Astron. Soc. Pac.*, 110:276–282, mars 1998.

R. F. Stellingwerf. Period determination using phase dispersion minimization. *Astrophys. J.*, 224:953–960, septembre 1978.

D. J. Stock & M. J. Barlow. A search for Ejecta nebulae around Wolf-Rayet Stars in the SHS Hα survey. *Bulletin de la Societe Royale des Sciences de Liege*, 80:316–321, janvier 2011.

R. C. Stone. The space frequency and origin of the runaway O and B stars. *Astron. J.*, 102:333–349, juillet 1991.

T. M. Tauris & E. P. J. van den Heuvel. *Formation and evolution of compact stellar X-ray sources*, pages 623–665. avril 2006a.

T. M. Tauris & E. P. J. van den Heuvel. *Formation and evolution of compact stellar X-ray sources*, pages 623–665. avril 2006b.

H. Todt, A. Y. Kniazev, V. V. Gvaramadze, W.-R. Hamann, D. Buckley, L. Crause, S. M. Crawford, A. A. S. Gulbis, C. Hettlage, E. Hooper, T.-O. Husser, P. Kotze, N. Loaring, K. H. Nordsieck, D. O'Donoghue, T. Pickering, S. Potter, E. Romero-Colmenero, P. Vaisanen, T. Williams & M. Wolf. Abell 48 - a rare WN-type central star of a planetary nebula. *Mon. Not. Roy. Astron. Soc.*, 430:2302–2312, avril 2013.

H. Todt, M. Peña, W.-R. Hamann & G. Gräfener. The central star of the planetary nebula PB 8: a Wolf-Rayet-type wind of an unusual WN/WC chemical composition. *Astron. Astrophys.*, 515:A83, juin 2010.

A. V. Tutukov, A. V. Fedorova & A. M. Cherepashchuk. Wolf-Rayet stars with relativistic companions. *Astronomy Reports*, 57:657–668, septembre 2013a.

A. V. Tutukov, A. V. Fedorova & A. M. Cherepashchuk. Wolf-Rayet stars with relativistic companions. *Astronomy Reports*, 57:657–668, septembre 2013b.

A. B. Underhill, S. Yang & G. M. Hill. The orbit of the Wolf-Rayet spectroscopic binary HD 193576, V444 Cygni. *Publ. Astron. Soc. Pac.*, 100:741–748, juin 1988.

V. V. Usov & D. B. Melrose. Pulsars with Strong Magnetic Fields - Polar Gaps Bound Pair Creation and Nonthermal Luminosities. *Australian Journal of Physics*, 48:571, 1995.

E. P. J. van den Heuvel. Interacting binaries: topics in close binary evolution. Dans S. N. Shore, M. Livio, E. P. J. van den Heuvel, H. Nussbaumer & A. Orr, éditeurs, *Saas-Fee Advanced Course 22: Interacting Binaries*, pages 263–474, 1994.

K. A. van der Hucht. The VIIth catalogue of galactic Wolf-Rayet stars. , 45:135–232, février 2001.

F. van Leeuwen. Validation of the new Hipparcos reduction. *Astron. Astrophys.*, 474: 653–664, novembre 2007.

gen W. De Loore C. D. Vanbeveren, Van bergen. *The Brightest Binaries*. 1998.

G. Walker, J. Matthews, R. Kuschnig, R. Johnson, S. Rucinski, J. Pazder, G. Burley, A. Walker, K. Skaret, R. Zee, S. Grocott, K. Carroll, P. Sinclair, D. Sturgeon & J. Harron. The MOST Asteroseismology Mission: Ultraprecise Photometry from Space. *Publ. Astron. Soc. Pac.*, 115:1023–1035, septembre 2003.

K. G. Wolinski & J. F. Dolan. Confidence Intervals for Orbital Parameters Determined Polarimetrically. *Mon. Not. Roy. Astron. Soc.*, 267:5, mars 1994.

S. A. Zhekov. X-rays from colliding stellar winds: the case of close Wolf-Rayet+O binary systems. *Mon. Not. Roy. Astron. Soc.*, 422:1332–1342, mai 2012.